Total Heat Input and Operational Temperature of Different Cell and Module Technologies

Ebrar Özkalay

TU Delft supervisor: Prof. Dr. Arthur Weeber
Daily supervisor: Dr. Bas B. Van Aken
Dr. Machteld P.W.E. Lamers

TU Delft ECN Your energy. Our passion.

Total Heat Input and Operational Temperature of Different Cell and Module Technologies

Thesis report

By

Ebrar Özkalay

At Energy research Centre of Netherlands (ECN)

in partial fulfilment of the requirements for the degree of

Master of Science

in Sustainable Energy Technology

Supervisor:	Prof. Dr. Arthur Weeber	TU Delft/ECN
Thesis Committee:	Dr. R.A.C.M.M. van Swaaij	TU Delft
	Dr. E. van der Kolk	TU Delft
	Dr. R. Santbergen	TU Delft
	Dr. Bas B. Van Aken	ECN Solar Energy

Date: 29-11-2017

List of Contents

Abbreviations 5
Nomenclature 6
List of Figures 9
List of Tables 11
ABSTRACT 12
1. Introduction 13
1.1. Solar Energy 13
1.2. Motivation and Objectives 14
1.3. Outline 16
2. Theory 18
2.1. Crystalline Si solar cells 18
2.2. Light Management of a Solar Cell 19
2.2.1. Reflection and Refraction 19
2.2.2. Light Absorption in the Solar Cell 21
2.2.3. Free Carrier Absorption (FCA) 24
2.3. Heating of Solar Cell 26
2.4. Heating of Solar Module 28
2.4.1 Absorbing and Reflective Back Sheet 29
2.5. Different Cell and Module Technologies 31
2.5.1. Al-BSF Solar Cell 31
2.5.2. n-Pasha Solar Cell 32
2.5.3. PERPoly Solar Cell 33
2.5.4. Jasmine Solar Cell 33
2.5.5. Module Designs 35
3. Heat Model 36
3.1. Heat Transfer 36
3.1.1. Convective Heat Transfer 36
3.1.2. Conductive Heat Transfer 38
3.1.3. Radiative Heat Transfer 38
3.2. Fluid Dynamic Model 40
4. The Experimental Setup 42
4.1. Building of the Modules 42
4.2. IV Measurement 42

4.3. Reflection and Transmission Measurements 43
4.4. Spectral Response Measurement 44
4.5. Outdoor Measurement Setup 46
5. Results and Discussion 49
5.1. Analysis of the Cells 49
5.1.1. Expected Heat Inputs of the Cells 52
5.1.2. Absorption Model for the PERPoly Cells 55
5.2. Analysis of the Single Cell Modules 56
5.2.1. Module Material Absorption 61
5.2.2. Total and Parasitic Heat Inputs 64
5.3. Outdoor Measurement Analysis 69
5.3.1. Effect of Module Type on Modules with Monofacial and Bifacial Cells 71
5.3.2. Effect of Cell Technology on Temperature of Glass-Glass Modules 74
5.3.3. Effect of Cell Technology on White back sheet & Black back sheet Modules 75
5.3.4. Comparison between Al-BSF Module with White back sheet and PERPoly 100nm Glass-Glass Module 77
5.4. Temperature Model Validation 78
5.4.1. Glass-Glass Module 79
5.4.2. White back sheet and Black back sheet Modules 80
6. Conclusion 83
7. Recommendation 85
8. Acknowledgement 86
9. Bibliography 87

Abbreviations

ABS	Absorption
Al	Aluminum
AR	Anti-reflection
Ag	Silver
BS	Back sheet
BSF	Back Surface Field
CTM	Cell to Module
c-Si	Crystalline Silicon
EVA	Ethyl Vinyl Acetate
E_{Ph}	Energy of the Photon
E_g	Bandgap energy
EQE	External Quantum Efficiency
FF	Fill Factor
FCA	Free Carrier Absorption
IQE	Internal Quantum efficiency
IBC	Integrated Back Contact
IR	Infrared
LPCVD	Low Pressure Chemical Vapor Deposition
LCOE	Levelized cost of electricity
MPP	Maximum Power Point
PV	Photovoltaics
PERL	Passivated Emitter with Rear Locally diffused
PERPoly	Passivated Emitter and Rear Polysilicon
n-Pasha	Passivated on all sides with H-Pattern
polySi	Polysilicon
PERC	Passivated Emitter Rear Cell
RFL	Reflection
Si	Silicon
SiN_x	Silicon Nitride
STC	Standard Test Condition
TM	Transmission
UV	Ultraviolet

Nomenclature

V_{oc}	Open circuit voltage
I_{sc}	Short circuit current
J_{sc}	Short circuit current density
k	Boltzmann's constant
T	Temperature
ϕ_{crit}	Critical angle
ϕ	Angle of incidence
d_c	Thickness of the AR coating
n	Refractive index
n_c	Refractive index of the AR coating
A_λ	Absorption
R_λ	Reflection
T_λ	Transmission
$I(x)$	The amount of light that transmitted as a function of traveled light distance
I_0	The intensity of incident light
$I_{abs.}(x)$	The amount of absorbed light as a function of traveled light distance
α	Absorption coefficient per wavelength
x	Travelled distance by the light
α_{depth}	Absorption depth of the photon per wavelength
$\alpha_{FCA,n/p}$	Free carrier absorption coefficient per wavelength
λ	Wavelength
c	Speed of light
q	Fundamental charge
N	Concentration of doping
ε_0	Vacuum permittivity
m^*	Effective mass
μ	Carrier mobility
E_g	Band gap of silicon
G_{eff}	Effective irradiance
$I_{sc,meas}$	Measured short circuit current under outdoor condition
$I_{sc,STC}$	Short circuit current at STC
G_{STC}	STC irradiance
$n_{ide.}$	Ideality factor
T_{Module}	Module temperature
T_{STC}	STC temperature
ρ	Density
t	Thickness
A_s	Surface area
C_{th}	Thermal capacitance
R_{th}	Thermal resistance
Q_{conv}	Heat transfer by convection

h_{conv}	Convective heat transfer coefficient
T_A	Ambient temperature
h_{free}	Free convection heat transfer coefficient
Nu	Nusselt number
Pr	Prandtl number
Gr	Grashof number
D_h	Hydraulic diameter of a module
L	Length of a module
W	Width of a module
g	Acceleration due to gravity on Earth
β	Volumetric thermal expansion coefficient of air
v	Kinematic viscosity of the air
w	Wind speed at module height
$h_{forced}^{lam.}$	Forced heat transfer coefficient of the laminar flow
$h_{forced}^{turb.}$	Forced heat transfer coefficient of the turbulent flow
c_{air}	Heat capacity of the air
w_a	Observed wind speed
p	Elevation factor
l_m	Height of the module
l_a	Height of the anemometer
h_{total}	Total convective heat transfer coefficient
T_{sky}	Sky temperature
$T_{gr.}$	Ground temperature
ε	Emissivity
σ	Stefan-Boltzmann constant
$F_{sky/gr.}$	Sky/ground view factor
h_{rad}	Radiative heat transfer coefficient
Q_{rad}	Heat transfer by radiation
R_{rad}	Thermal radiative heat resistance
α_f	Thermal absorption of the front side
α_r	Thermal absorption of the rear side
G_f	Incident illumination on the front side of the module
G_r	Incident illumination on the rear side of the module
$\alpha_{th.}$	Thermal absorption
η	Efficiency of the module
$S(\lambda)$	AM1.5G global standard solar spectrum
$I_{RFL}(\lambda)$	Spectrum of the reflection
$I_{TM}(\lambda)$	Spectrum of the transmission
$I_{Elect.}(\lambda)$	Electrical output
$I_{Therma.}(\lambda)$	Thermalization
$I_{Para.}(\lambda)$	Parasitic heating
$E_{g,fermi}$	Energy difference between quasi fermi levels

$S_g(\lambda)$	Energy of the solar spectrum
c_h	Specific heat capacity
$I_{Rec.,Entr.,Resis.}(\lambda)$	Recombination, entropy and resistive losses
$\alpha_{FCA,polysilicon,n}$	Free carrier absorption coefficient of polysilicon per wavelength

List of Figures

Figure 1: The learning curve of PV [6]. 13
Figure 2: Configuration of the conventional crystalline silicon solar cell. 18
Figure 3: Reflected and refracted light by a smooth interface. 19
Figure 4: Reflected and refracted light when there are a coating on the layer. 20
Figure 5: Reflection and transmission of the light when there are multiple layers. 20
Figure 6: Reflection from the front metal grid of the solar cell. 21
Figure 7: The absorption coefficient of the intrinsic silicon as a function of wavelength [20]. 22
Figure 8: The absorption depth in the silicon. 22
Figure 9: Reflection from smooth surface versus textured surface. 24
Figure 10: Total internal reflections when the front and rear surfaces are textured. 24
Figure 11: The absorption coefficient of the intrinsic silicon as a function of wavelength [20], p-type 1×10^{16} cm^{-3} concentration doped bulk silicon and n-type 3×10^{20} cm^{-3} concentration doped emitter [25] [30]. 26
Figure 12: AM 1.5G solar spectrum with converted usable energy [31]. 27
Figure 13: The configuration of module with back sheet. 29
Figure 14: The reflection of white and black back sheets and transmission of the white back sheet.. 30
Figure 15: The light management of solar module with white and black back sheet. 30
Figure 16: The reflection of white and black back sheets and transmission of the white back sheet for their rear sides 31
Figure 17: Configuration of the conventional crystalline silicon solar cell. 32
Figure 18: Configuration of the n-Pasha bifacial solar cell. 32
Figure 19: Configuration of the PERPoly bifacial solar cell. 33
Figure 20: Configuration of the PERC solar cell. 34
Figure 21: Configuration of the Jasmine bifacial solar cell. 34
Figure 22: Configuration of (a) the glass-glass module and (b) module with back sheet. 35
Figure 23: Heat transfer of PV module with convection, conduction and radiation [42]. 36
Figure 24: Heat transfer mechanism of PV module. 40
Figure 25: (a) Placement of solar module for PASAN measurement. (b) Black sheet to prevent any incident light from the rear side. 43
Figure 26: Optical configuration of reflection and transmission measurements. 43
Figure 27: Placement of the solar cell samples with and without foil. 44
Figure 28: Measurement spots of the cell for homogeneous distribution. 44
Figure 29: Configuration of the spectral response(SR) measurement setup. 45
Figure 30: SR measurement of (a) a solar cell and (b) a solar module. 45
Figure 31: Outdoor measurement setup. 46
Figure 32: Position of the modules on the rack. 47
Figure 33: Abstract scheme of the passive outdoor measurement system [51]. 47
Figure 34: IQE of the different cell types. 50
Figure 35: IQE response of the different cell types between 950 nm and 1200nm. 50
Figure 36: Reflection and 1-transmission of the different cell types. The arrows show the absorption rate at 1180nm. 51
Figure 37: Spectrum of AM1.5g and electrical output, thermalization. Reflection and parasitic heating of the Al-BSF cell. 53
Figure 38: Spectrum of the parasitic heating of different cell types. 54

Figure 39: Modeled total absorption (band to band absorption of silicon and free carrier absorption) and measured absorption by using the measured spectral reflection and transmission for PERPoly 100nm cell. 55
Figure 40: Modeled total absorption (band to band absorption of silicon and free carrier absorption) and measured absorption by using the measured spectral reflection and transmission for PERPoly 200nm cell. 55
Figure 41: Distribution plot for band to band absorption, free carrier absorption, reflection and transmission of (a)PERPoly 100nm and (b)PERPoly 200nm at 330-1400nm wavelengths. 56
Figure 42: I_{sc} and P_{mpp} of different module types with different cell types (n-Pasha). 58
Figure 43: IQE of glass-glass modules with different cell types. 59
Figure 44: Reflection and 1-Transmission of the glass-glass modules with different cell types..... 60
Figure 45: Reflection and 1-Transmission of the different modules types with bifacial cell. 61
Figure 46: Various optical losses of a solar module (active area) (transmission for bifacial modules is not included). (1=reflection of air/glass interface, 2 = reflection of glass/EVA interface, 3 = reflection of EVA/Cell interface, 4 = absorption of glass, 5 = absorption of EVA.) 61
Figure 47: Absorption rate of the glass/EVA/glass stack..... 62
Figure 48:(a) CTM IQE of glass-glass module with bifacial cell and (b) CTM reflection and 1-transmission of glass-glass module with bifacial cell 63
Figure 49: Spectrum of the parasitic heating of bifacial cell and different module types with bifacial cell. 63
Figure 50: Parasitic heating spectrum of glass-glass modules with different cell technologies. 64
Figure 51: Parasitic heating spectrum of different module types with monofacial cell. 65
Figure 52: Parasitic heating spectrum of different module types with bifacial cell. 65
Figure 53: Parasitic heating spectrum of white back sheet module with different cell technologies. . 66
Figure 54: Parasitic heating spectrum of black back sheet module with different cell technologies... 66
Figure 55: Total parasitic heating of different module types with different cell technologies. 67
Figure 56: Total parasitic heating of different module types with different cell technologies with (0.3 sun at rear) and without (no sun at rear) rear contribution. 68
Figure 57: Total heating of different module types with different cell technologies with (0.3 sun at rear) and without (no sun at rear) rear contribution. 69
Figure 58: (a) Pareto chart and (b) main effect plot for front irradiance and wind speed. 70
Figure 59: Module temperature relative to ambient temperature as a function of front irradiance at low (1 m/s) and high (25 m/s) wind speeds. 70
Figure 60: Module temperature relative to ambient temperature as a function of front irradiance for different module types with Al-BSF cell. 71
Figure 61: Module temperatures relative to ambient temperature as a function of front irradiance for different module types with PERPoly 100nm cell. 72
Figure 62: Temperature of monofacial modules relative to temperature of bifacial module as a function of front irradiance. 73
Figure 63: Temperature of glass-glass modules relative to ambient temperature as a function of front irradiance for different cell technologies. 74
Figure 64: Temperature of glass-glass modules with different cell technologies relative to temperature of PERPoly 100nm module as a function of front irradiance. 75
Figure 65: Temperature of white back sheet modules relative to ambient temperature as a function of front irradiance for different cell technologies..... 75

Figure 66: Temperature of white back sheet modules with different cell technologies relative to temperature of PERPoly 100nm module as a function of front irradiance. 76
Figure 67: Temperature of black back sheet modules relative to ambient temperature as a function of front irradiance for different cell technologies. 77
Figure 68: Temperature of black back sheet modules with different cell technologies relative to temperature of PERPoly 100nm module as a function of front irradiance. 77
Figure 69: Temperature of Al-BSF white back sheet module relative to PERPoly 100nm glass-glass module. 78
Figure 70: Front irradiance of 24th (Low irradiance day) and 25th (High irradiance day) of October. 78
Figure 71: Predicted and observed module temperature of glass-glass module with ambient temperature and wind speed for 25th of October (High irradiance day). 79
Figure 72: Predicted and observed module temperature of glass-glass module with ambient temperature and wind speed for 24th of October (Low irradiance day). 80
Figure 73: Predicted and observed module temperature of white back sheet module with ambient temperature and wind speed for 25th of October (High irradiance day). 81
Figure 74: Predicted and observed module temperature of white back sheet module with ambient temperature and wind speed for 24th of October (Low irradiance day). 81
Figure 75: Predicted and observed module temperature of black back sheet module with ambient temperature and wind speed for 25th of October (High irradiance day). 82
Figure 76: Predicted and observed module temperature of black back sheet module with ambient temperature and wind speed for 24th of October (Low irradiance day). 82

List of Tables

Table 1: The module types for each cell type that are used in the project. 16
Table 2: Number of single cell laminates for each cell and module type. 35
Table 3: IV values of different cell types. 49
Table 4: IV values of rear side of different cell types. 49
Table 5: Average total heating, total parasitic heating and fraction of parasitic heating of the different cell types with a standard deviation. 54
Table 6: IV characteristics of glass-glass modules with different cell types 56
Table 7: Cell to Module change on I_{sc}, efficiency and bifaciality factor for the glass-glass module with different cell types 57

ABSTRACT

Monofacial modules capture light that falls on the front side of the module, and convert the solar energy to electricity. Bifacial modules can also capture the light that falls on the rear side of the module. For free standing bifacial modules, this results in a power output increase of 5 to 30% compared to monofacial modules. However, due to the heat generation by rear irradiance, this gain is partly lost. In this work, the effect of cell architecture (bifacial/monofacial) and module layout (bifacial/monofacial) on how much modules heat up under outdoor conditions is examined and the heat input mechanism from indoor measurements investigated. This is important because high temperature decreases the open circuit voltage (V_{oc}) of the cell/module which means less power output.

Main heat input mechanisms of a solar cell are thermalization, recombination, entropy, absorption of metal parts of the cells and free carrier absorption (FCA) which is absorption of IR light below the band gap. Since the cells that are used in this work have the same absorbing material (Crystalline silicon), comparable thermalization, recombination and entropy losses are expected. Hence, main difference between total heat input of the cells is due to the difference in parasitic heat inputs which includes FCA, absorption of metal parts and recombination. From heat input calculations by using indoor measurements, modules with Al-BSF cell have the highest heat input compared to modules with bifacial cell due to parasitic light absorption by the full aluminum (Al) back contact. This indoor calculation correlates with outdoor measurements where the modules are placed free-standing on rooftop of a building. Glass-glass module with Al-BSF cell is 3.4±1.7 K higher in temperature at 1000 W/m2 front irradiance (rear irradiance is around 11% of front irradiance) compared to glass-glass module with a PERPoly 100nm cell, which is one of the bifacial cells in this work. Additional to the parasitic absorption by the Al back contact from light from the front side, the rear illumination that is not reflected (80%) is fully absorbed and turned into heat by the rear configuration (Al/EVA(ethylene vinyl acetate)/Glass). For white back sheet modules (Glass/EVA/Solar Cell/EVA/white back sheet), Al-BSF module has 2.4±0.8 K higher temperature compared to PERPoly 100nm module at 1000 W/m2 front irradiance. Both these temperature differences for glass-glass and white back sheet modules correspond to 1.4±0.7% and 1.0±0.3% power gain for PERPoly 100nm modules compared to Al-BSF module. From the outdoor results, glass-glass PERPoly 100nm module is 3.6±1.5 K cooler than Al-BSF white back sheet module at 1000 W/m2 front irradiance (rear irradiance is around 11% of front irradiance). This temperature difference corresponds 1.5±0.6% power gain for PERPoly 100nm module compared to Al-BSF module. This result does not correlate with the indoor heat input calculations because higher heat input calculated for bifacial module compared to monofacial module at 11% rear irradiance fraction. The main reason for the absence of heating of bifacial module can be the 6% higher emissivity of glass compared to back sheet which results in higher radiative heat transfer for bifacial modules [1] [2]. Also, conductive heat transfer within the module level for bifacial modules might be better compared to monofacial modules. Even though indoor results show that a bifacial module heats more under 11% rear irradiance, outdoor results show that a bifacial module is cooler than monofacial module. At higher rear irradiance conditions the bifacial module might have the same temperature as monofacial module, while the power output is 5 to 30% higher, making the bifacial modules very attractive for large scale implementations.

1. Introduction

1.1. Solar Energy

In 2015, global energy production was around 24100 TWh which was provided from non-renewable (76.5%) and renewable energy sources (23.5%) [3]. Due to the depletion of non-renewable sources (e.g. coal, natural gas and oil) and negative environmental impact of the use of fossil fuels (e.g. climate change) [4] [5], transition from non-renewable energy sources to renewable energy sources (e.g. hydro, wind, solar, biofuel, geothermal) has started. Photovoltaics (PV) and thermal energy from solar energy are types of solar energy sources. PV had 1% contribution on the global energy generation in 2015 [3]. The energy generation by PV grows faster than most of the other electric generation technologies with a growing rate of around 45% in the last 15 years while the cost of the PV is reduced enormously [4]. Increasing cumulative production rate with decreasing cost can be expressed by the Swansson's law (learning curve) [5]. As can be seen in Figure 1, module prices learning rate is 22.5% over last 41 years, and even 39% over the last decade [6]. Due to the silicon shortage between 2004 and 2006, there is peak in the cost of the PV. Globally, the weighted average levelized cost of electricity (LCOE) for coal and natural gas was around 0.05-0.15 USD/kWh in 2015 and for large scale solar PV this was 0.13 USD/kWh, which is comparable with coal and natural gas prices [3]. The LCOE for large scale solar PV is expected to be below 0.03 USD/kWh in 2017. The reason behind the price reduction of the PV modules is the increasing efficiency of the solar cells, improvements in the manufacturing of solar modules and economies of scale [7] [8]. Looking at the historic trend of the learning curve, it is foreseen that the PV industry can keep the curve at high levels with improving cell and manufacturing technologies [4].

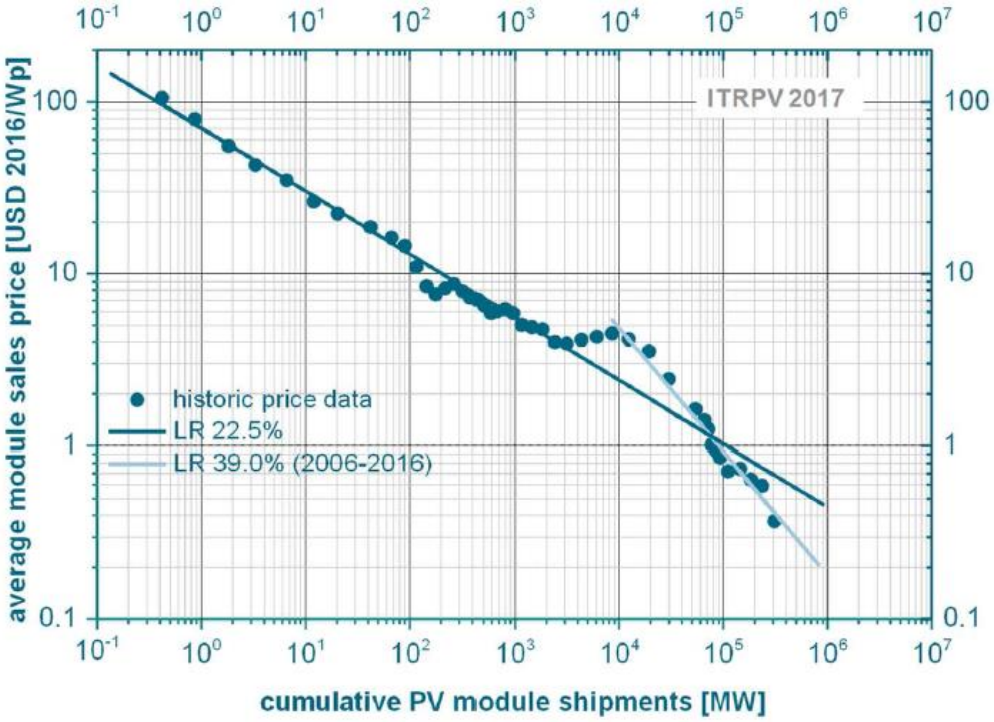

Figure 1: The learning curve of PV **[6]**.

Silicon solar cells are photovoltaic devices, converting the energy of the light directly to electricity, which use silicon as an absorber material with 1.12 eV band gap energy. Most common industrial made type of solar cell is the so-called monofacial Al-Back Surface Field (BSF) solar cell. However, this solar cell type is limited in maximal achievable efficiency, due to the higher rear recombination losses. There are different types of cell technology in the market and in the research phase. As high efficiency is needed in order to keep the learning curve at high levels, many research centers and universities are studying the high efficient solar cell technologies around the world. Rear passivated solar cell technologies like Passivated Emitter with Rear Locally diffused (PERL) cell [9] and Passivated Emitter and Rear Polysilicon (PERPoly) cell [10] can be given as an example of this. Another focus point in achieving high efficiencies is the reduction of the front metallization, which creates more active area available to refract light into the cell, by using for example Interdigitated Back Contact (IBC) [11] cell technology. Additionally, bifacial solar cells, which collect incident light both at the front and rear of the cell, is another promising technology to increase the amount of electricity production per area without increasing the production cost of the cell [12]. An additional advantage of bifacial solar cells over monofacial solar cells is the lower operational temperature due to the absence of full aluminum back contact which highly absorbs unabsorbed infrared (IR) light through the solar cell and acts as a heat generator [13] [14]. A lower operational temperature of the solar panel is desired as it is directly linked to higher power performance. The reasons for the increment in the temperature of PV modules during the operation are thermalization and parasitic heating which consist of recombination, free carrier absorption (FCA), absorption of light by inactive area of the solar cell and module materials. The solar module which is heated by irradiation of sun light cools down by convection (free and forced convection) and radiation. Especially, forced convection, which is function of the wind speed, is very dominant at places like Petten, Netherlands due to the high wind speeds during a year.

1.2. Motivation and Objectives

Two of the loss mechanisms when light is absorbed by the solar cell are: 1) absorbed photons with more energy than the band gap generates electron-hole pairs. This energy surplus is transferred to heat which is called thermalization; 2) refracted infrared (IR) light below the bandgap might be absorbed by free charge carriers (without creating electron-hole pairs) which is called free carrier absorption (FCA). FCA is dependent on doping level and causes parasitic heating [15]. In both cases, it leads to drop in the performance of cell and an increase in the temperature (and the associated loss in voltage) [16]. Another loss mechanism is the recombination. The aim of the project to understand the science/mechanism behind the heating/operating temperature of bifacial/monofacial modules with bifacial/monofacial solar cells.

During the project, four different bifacial cells (n-Pasha, jasmine, PERPoly 100nm, PERPoly 200nm) and monofacial (Al-BSF) solar cells were used. In Al-BSF solar cells, non-absorbed IR light cannot pass through the cell due to the full aluminum (Al) back contact. It is either reflected by or absorbed in the Al layer. In the bifacial solar cells, since light can pass through the cell, less parasitic absorption is expected. Due to the lower parasitic absorption in the bifacial cells, less parasitic heating is expected compared to the monofacial cells which is

associated with loss in performance. However, bifacial solar cells can get light from also the rear side which improves performance but also causes additional heating by FCA, thermalization and recombination of electron-hole pairs. Despite the extra heating from rear illumination of the bifacial cells, temperature of the bifacial cell is expected to be lower than temperature of the monofacial cell under operating conditions due to absence of full area Al back contact. Lower operating temperature which increases the performance is an additional advantage of the bifacial cells over the monofacial cells to illumination gain from back side of the cell.

Due to the different rear side technologies and the back surface field (BSF) layers, there are differences between the parasitic heating of different bifacial cell types (n-Pasha, PERPoly 100nm, PERPoly 200nm and jasmine) which affects the FCA. The BSF layer (100 and 200nm thick) of the PERPoly cells has higher doping level than the BSF layer of the n-Pasha cells which affects the FCA. Hence, higher FCA is expected in PERPoly cells compared to n-Pasha cells. Thermalization and recombination losses of the n-Pasha and PERPoly cells are expected to be around same level due to the similar cell technology compared to the Al-BSF technology. Therefore, only FCA makes the difference between their total heating and temperature. Due to higher parasitic heating, a slightly higher operational temperature is expected for PERPoly cells compared to n-Pasha cells. There are two types of PERPoly cells which have 100nm and 200nm thick BSF layer. Temperature of the PERPoly cell with thick BSF layer is expected to be higher than temperature of the PERPoly cell with thin BSF layer since thicker layer can absorb more than thinner layer.

The jasmine solar cells have local BSF regions at the Al rear contacts and 6nm Al_2O_3 layer at the open areas for passivation purposes, which is therefore not optically active for incoming light due to its thickness. Hence, the interface between the jasmine cell and ethyl vinyl acetate (EVA), which is encapsulant material, acts as Si-EVA interface which is highly reflective for unabsorbed IR light through the cell [17]. Therefore, low parasitic heating and FCA are expected in the jasmine cells. For this work, five types of cells were used and in the results the highest total heating and parasitic heating are expected for monofacial Al-BSF cell due to the Al-BSF back side.

The different module types that are evaluated in this work are glass-glass modules and modules with white and black back sheet. Each module type has a different light management for incident light on the front and rear and consequently, the influence on the heating is also different. Light can go through glass-glass modules and light that is not initially absorbed by the solar cell by the first pass will escape the module. For white back sheet modules, light incident on the front side passing through the solar cell will be highly reflected back to the solar cell by the white back sheet for a second pass. For a black back sheet module, this reflection is minimum and will be absorbed by the back sheet, adding full to the heating of the module. For white back sheet modules, when only illuminating the front, power output will be highest as the light reflected on the rear can pass through the cell again and be absorbed creating electron-hole pairs. For black back sheet module the power output will be lower and heating higher as no second pass of the light occurs. For glass-glass modules, the second pass of the light also does not happen and power output is subsequently lower, but the module does not increase in temperature as the light is not absorbed by the module material. The table

below shows the module types for each cell type which was used in indoor and outdoor measurements.

Table 1: The module types for each cell type that are used in the project.

	n-Pasha	PERPoly (200nm)	PERPoly (100nm)	Jasmine	Al-BSF
Glass-Glass	x	x	x	x	x
White back sheet	x	-	x	x	x
Black back sheet	x	-	x	x	x

The expected outcomes of this work are:

1. Understanding the science/mechanism behind the heating/operating temperature of bifacial/monofacial modules with bifacial/monofacial solar cells.
2. Effect of cell concept on parasitic heating (monofacial vs bifacial cells and different bifacial cell technologies).
3. Effect of back sheet on parasitic heating for different cell concepts.
4. Absorption of solar module materials (glass, EVA, white and black back sheet).
5. Absorption of encapsulated (different module types) and not encapsulated cell.
6. Understanding the effect of parasitic heating and FCA on the total heating of the solar cell and module.
7. Temperature prediction (Fluid dynamic model) of monofacial and bifacial modules depending on cell and module characteristics and components.
8. Effect of module type and cell technology on temperature of the module in outdoor 'real-life' conditions.

1.3. Outline

The second chapter provides background knowledge of the research. Firstly, crystalline silicon solar cells are introduced and then, light management of the cells are explained elaborately. Some part of the absorbed light by solar cell and module causes heat. This generated heat by solar cells and solar modules is described. In the end of the chapter, cell and module technologies that are used in this work are explained.

The fluid dynamic heat model, used in this research, is explained with all heat transfer mechanisms of the solar module in chapter three. The chapter four describes the indoor experimental setup and outdoor measurement setup in order to get results for this work.

In the fifth chapter the results are presented and discussed and it is divided into four main parts. The first part gives the indoor measurement results of the cell, expected heat input from indoor measurements and absorption model for PERPoly cells. In the next part, indoor measurement results of the modules and expected heat input of the modules are discussed. Also, module material absorption and cell to module losses are explained in this part. The third part describes effect of cell and module technology on operational temperature of modules from outdoor measurement setup. In the last part of this chapter, the temperature

model, which is explained in previous chapters, is validated by comparing predicted temperature from the model and observed temperature.

The last two chapters provide conclusions and recommendations for future work respectively.

2. Theory

2.1. Crystalline Si solar cells

Crystalline silicon (c-Si) solar cells are electronic devices which can convert sunlight directly into electricity (Figure 2). The active part of the solar cell is crystalline silicon which is a semiconductor. Thickness of the silicon absorber material is mostly around 160 μm. Most conventional c-Si solar cells have p-type bulk which is lightly doped with boron. In the top section of the solar cell, there is a thin n-type region which is called emitter layer and is typically 0.2-0.3 μm deep. The n-type emitter layer is created by diffusion of phosphorus. Due to the chemical potential that arises in the region between the p-type bulk and n-type emitter, a voltage called as ‘’build in potential’’ is created which can separate the charge carriers (electrons and holes) from each other under illumination. With AM1.5 illumination, most of the charge carriers are generated within the first 10 μm from the front surface. Charge carriers can also recombine again (whereby heat is generated and current is lost) and one of main recombination sites are the surfaces which is Shockley-Read-Hall (SRH) recombination. Reduction of the surface recombination is done by passivating the surface by using a coating on top of the emitter layer, like silicon nitride (SiN_x), which can also function as an anti-reflection (AR) layer. In order to collect the generated current from the wafer, H-grid pattern metallization is used at the front surface of the cell as a metal contact. The cross section of the metal contacts is designed carefully to optimize loss due to shading of the metal contact and series resistance due to the small cross-section area of the metal contact. Additionally, to minimize the losses at the interface between the metal contact and the emitter, the emitter directly below the contact is highly doped, and it is indicated with n++. At the rear side of the cell, a thin aluminum layer is used as a metal contact. A highly doped back region is created by alloying with of silicon with the thin aluminum layer and epitaxial re-growth during cooling down. This highly doped region is called back surface field (BSF). This layer passivates the rear surface and decreases the loss of the electron-hole pairs at the back of the solar cell.

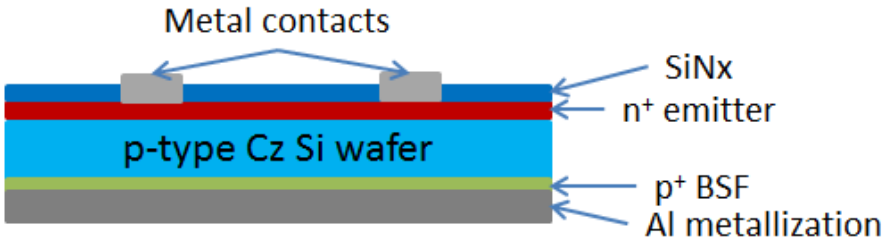

Figure 2: Configuration of the conventional crystalline silicon solar cell.

2.2. Light Management of a Solar Cell

2.2.1. Reflection and Refraction

Solar modules are optical multilayer systems. Since the refractive indices of those layers are different from each other, incident irradiance is reflected and refracted. The incremental increase in the refractive index per layer will maximize the refracted and minimize the reflected light. Texturing the surfaces relative to each other will further improve light transmission to the electrical active part of the module, the solar cell.

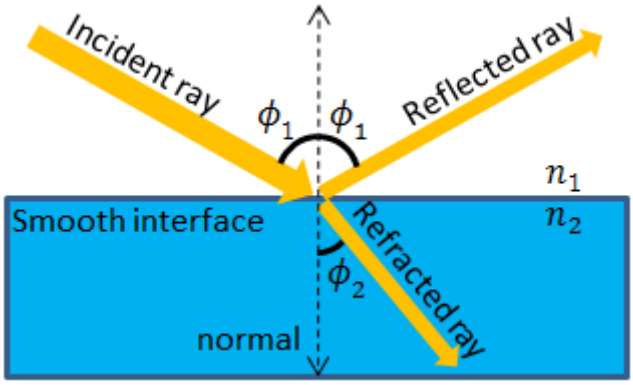

Figure 3: Reflected and refracted light by a smooth interface.

Figure 3 shows the reflection and refraction of the smooth surface which reflects the irradiance in a specular way. To describe the interaction between two mediums, besides the geometry of the interface, the refractive indices (n) of the mediums need to be known. The incident ray of light on the interface splits up to refracted and reflected rays. The Snell's law gives the relation between the angle of incidence (ϕ_1) angle of refraction (ϕ_2).

$$n_1 \sin \phi_1 = n_2 \sin \phi_2 \qquad \textbf{Eq. 1}$$

where n_1 and n_2 are refractive index of the medium 1 and 2 respectively. When light passes from high refractive index medium to low refractive index medium (i.e. $n_2 > n_1$), there is a critical angle (ϕ_{crit}) which is given by

$$\phi_{crit} = sin^{-1} \frac{n_1}{n_2}. \qquad \textbf{Eq. 2}$$

If the angle between incident ray and the interface normal is larger than a critical angle, there is no transmission, and the light reflects from the interface to the layer. This consequence of the Snell's law can increase the probability of trapping ray of light inside the layer since refractive indices of the solar module materials are gradually decrease from solar cell to module surrounding. The refractive index of the silicon is around 3.9 and the refractive index of encapsulation material is around 1.5, so critical angle for the silicon-glass interface is around 22.6˚. Also, the critical angle for the glass-air interface is around 41.8˚.

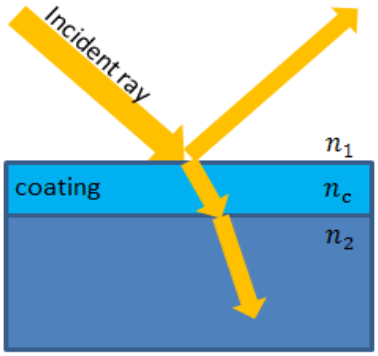

Figure 4: Reflected and refracted light when there are a coating on the layer.

Since the reflection is an optical loss mechanism, it is important to reduce the reflection as much as possible to increase the performance of the solar cell. As shown in Figure 4, a coating between two mediums can be used to decrease the reflection. The optimized refractive index of the coating (n_c) can be found by

$$n_c = \sqrt{n_1 n_2}. \quad \textbf{Eq. 3}$$

By using coating, we can get reflection minimum at a particular wavelength region. And by changing the thickness of the coating (d_c), the wavelength region of the reflection minimum can be arranged. By using more than one layer, reflection can be decreased more. This technique is called refractive index grading [18].

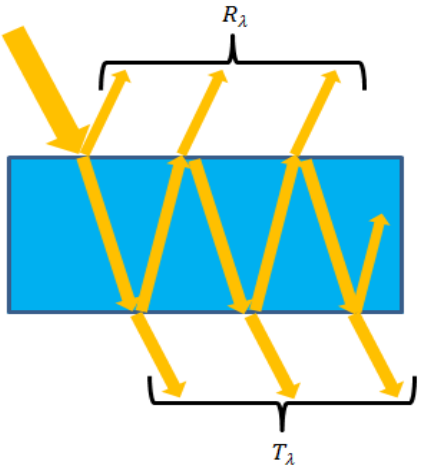

Figure 5: Reflection and transmission of the light when there are multiple layers.

Figure 5 shows a multilayer system with three layers and two smooth interfaces. Each layer has a different refractive index. As it can be seen from Figure 5, some part of the incident light may be trapped in the layer. All light rays need to be taken into account to determine reflection (R_λ) and transmission (T_λ) of the multilayer system. From the conservation of the energy, absorption (A_λ) of the multilayer system can be calculated by

$$A_\lambda = 1 - T_\lambda - R_\lambda. \quad \textbf{Eq. 4}$$

When light passes through an absorbing layer, the intensity of the light decreases exponentially. The amount of light that transmitted ($I(x)$) can be calculated by the Lambert-Beer law [19].

$$I(x) = I_0 e^{-\alpha x} \quad \textbf{Eq. 5}$$

where I_0 is the intensity of incident light, α is the absorption coefficient and x is the traveled distance by light. For high absorption, either absorption coefficient α or the traveling distance of the light x should be very large. Based on the conservation of the energy, the amount of absorbed light ($I_{abs.}(x)$) can be calculated by

$$I_{abs.}(x) = I_0(1 - e^{-\alpha x}). \quad \textbf{Eq. 6}$$

2.2.2. Light Absorption in the Solar Cell

Most solar cells have metal contacts on both sides to collect and transport carriers. On the front side an H-grid pattern is generally used. A small fraction of the incident light on the solar cell hits the metal contacts which prevent the light going into the solar cell and causes shading losses. This light is either reflected or absorbed by the contact which is a kind of parasitic absorption and causes heating of the solar cell (Figure 6). The optimal design of the metal contact is critical. It should cover a small area on the front surface to prevent high shading loss. On the other hand, it should be thick and wide enough to prevent high series resistance losses. Thereby, it is a trade-off between the large active area which is the area without metal contact and low series resistance of the metal contact.

Figure 6: Reflection from the front metal grid of the solar cell.

Incident light on the active area of the solar cell is either reflected, transmitted through the solar cell or absorbed in the solar cell. Absorbed light in the solar cell can generate electron-hole pairs. The possibility to create electron-hole pairs depends on the energy of the photon (E_{ph}) and band gap energy of the solar cell material (E_g). If $E_{ph} < E_g$, there will be very no absorption and the light will transmit through the cell. If $E_{ph} = E_g$, the photon has the enough energy to produce exactly one electron-hole pair. If $E_{ph} > E_g$, there will be generation of also exactly one electron-hole pair generation and the excess energy will thermalize the excited electron, which generates heat in the solar cell.

Each semiconductor material has a different absorption coefficient per wavelength. The difference between the absorption coefficients of different semiconductor materials can be used to increase the performance of the solar cells such as multi-junction solar cells which have two or more absorbing junctions. Higher absorption coefficient means that there will be a greater possibility to absorb a photon and create an electron-hole pair. The absorption coefficient of the silicon per wavelength can be seen in Figure 7. Semiconductor materials have a sharp edge that show their band gap energy. They cannot absorb a photon which has lower energy than the band gap energy of the solar cell. In this case, silicon cannot absorb light which has larger wavelength than 1.1 µm as shown in Figure 7.

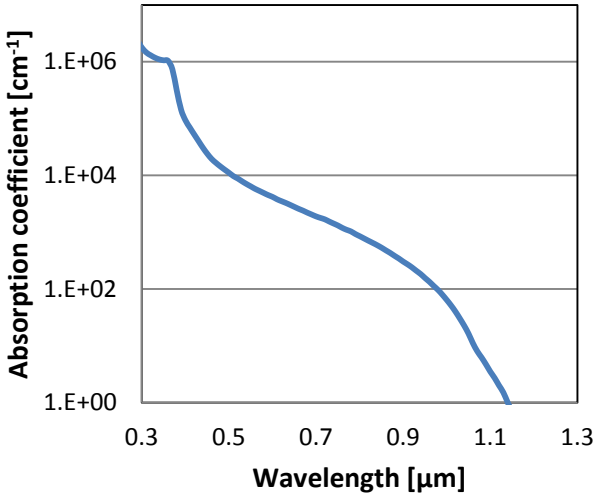

Figure 7: The absorption coefficient of the intrinsic silicon as a function of wavelength **[20]**.

The absorption coefficient is related to the absorption depth (α_{depth}) of the photon per wavelength, as given by the following equation.

$$\alpha_{depth} = \frac{1}{\alpha} \qquad \textbf{Eq. 7}$$

The inverse of the absorption coefficient shows the traveling distance of the ray light in the solar cell before it is absorbed. Short wavelengths have high energy and high absorption coefficient. Figure 8 shows the absorption depth of the light as a function of wavelength. Short wavelengths have very small absorption depth, so they are absorbed close to the surface of the cell. Long wavelengths have low absorption coefficient, so their absorption depth is large which means that they need to travel more in the cell to be absorbed (Figure 8). They are absorbed through the solar cell, but some of the long wavelength light pass through the cell without any absorption.

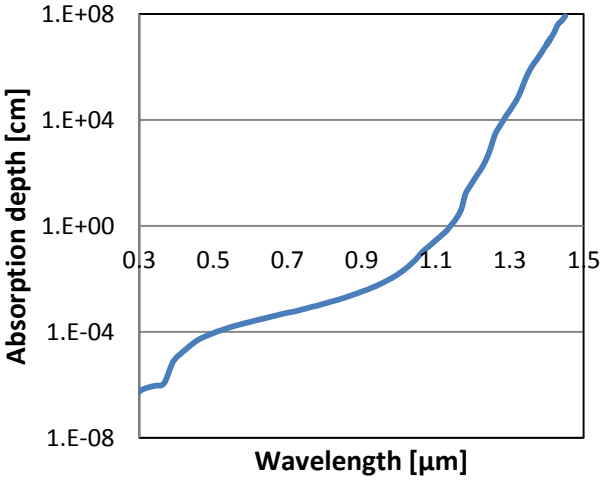

Figure 8: The absorption depth in the silicon.

The absorption depth of the material has an effect while deciding the thickness of the solar cell. Thicker solar cells absorb more long wavelengths light than thinner solar cells. Therefore, for more light absorption, a thicker solar cell is preferable. The diffusion length of the minority carriers in the solar cell is also an important parameter while determining the

thickness of the cell. Light generated carriers must reach the junction before recombination occurs, which decreases the open circuit voltage. It can be only possible when the light is absorbed within this diffusion length. To prevent recombination loss either thinner cells should be used or diffusion length of the carriers should be longer. If we assume the thickness of the cell is constant, doping level of the cell must be decreased to increase the diffusion length. On the other hand, minority charge carriers cause lower open circuit voltage due to recombination. This loss mechanism can be reduced by minimizing the minority charge carrier concentration. Increasing the doping concentration decreases the minority charge carrier and consequently lower recombination occurs due to minority charge carrier concentration. Hence, there is a trade-off between longer diffusion length and high open circuit voltage due to less recombination. Another parameter while deciding the thickness of the solar cell is cost of the wafer. Thinner wafer is cheaper and cost of the solar cell should be low enough to compete with other type of energy sources. Also, processing of the wafers to cells is an important parameter on the thickness of the solar cell. Probability and level of fault (breakage etc.) during the process affect the choice of thickness. All of these parameters that are mentioned above are considered to decide the thickness of the solar cell.

Some light trapping techniques are used to increase the absorption of the solar cell structure. As a result of light trapping, light can travel inside of the cell several times which is much longer than the thickness of the cell. With good light trapping, the traveling distance of the ray of light can be enhanced by factor up to $4n^2$ where n is the refractive index of the semiconductor material [21]. In this case, a light ray in silicon may pass 50 times on average before escaping out. Therefore, the probability of absorption of the long wave light increases without increasing the thickness of the cell.

For solar cells, there are several manners to increase the amount of the light which is refracted to the cell. One of them is using a coating for anti-reflection purposes as explained in chapter 2.2.1. The same coating is also used for passivation purposes. On the surface, since some valence electrons cannot find a partner to create a covalent bond with, dangling bonds which are a type of defect occurring at the surface. Those defects introduce trap state which can trap electron, and it recombines with a hole which is attracted by the trapped electron. This loss mechanism is called surface recombination, and it can be minimized by adding a thin layer onto the semiconductor surface. Because of the thin coating, the valence electrons on the surface can create a covalent bond with the elements in the thin layer and surface recombination decreases. This process called passivation and silicon nitride (SiN_x) layer is commonly used for anti-reflective and passivation purposes.

Besides anti-reflective coating, a textured front surface can be used to decrease the amount of the reflected light from the front surface. Figure 9 shows the incident light on the smooth and textured surfaces. Reflected light from the textured surface has higher probability to bounce back onto surface compared to reflected light from flat surface. This causes less reflection compared to flat surface. Because of the angled surface, the angle of the refracted light may be increased compared to the smooth surface. Therefore, optical path of the ray light may be longer in the solar cell which increases the probability of the light trapping and absorption of the light.

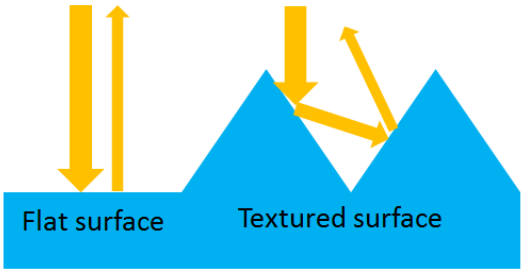

Figure 9: Reflection from smooth surface versus textured surface.

Another way to trap the light inside of the cell is reflecting at the rear. Instead of passing through the cell, by using reflecting back, ray light can be reflected from the rear which increases the optical path length of the ray light. This ray of light may hit the textured interface again, and if the incident angle of the ray of light is higher than the critical angle, the light can reflect back into the cell again. Also by using a textured rear reflector as can be seen in Figure 10, the number of total internal reflections can be increased more. Basically, due to the internal reflections, light may be trapped inside the cell and make several passes through the cell which increases the probability of the absorption of the light and enhance the performance of the cell without changing the thickness of the cell.

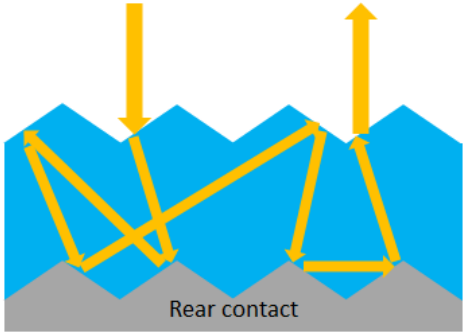

Figure 10: Total internal reflections when the front and rear surfaces are textured.

2.2.3. Free Carrier Absorption (FCA)

The refracted infrared (IR) light with photon energy below the bandgap might be absorbed in p or n type doped region by free charge carriers which are called free carrier absorption (FCA). Free carrier absorption is an optical absorption process which does not generate electron-hole pairs, but the energy of the photon is absorbed by the free carriers. These carriers are introduced by p or n type doping to a semiconductor to create the p-n junction. The free carriers, which absorbed the photon energy, move to a higher state in conduction band [22]. During the relaxation of the carrier to its original state, the carrier generates heat which is an undesirable effect for silicon solar cells.

The temperature, thus released heat, has very little effect on the short circuit current (I_{sc}) but it has significant effect on the open circuit voltage (V_{oc}) and decreases the V_{oc} of the cell which is discussed in detail in chapter 2.3. Hence, the performance of the solar cell decreases with heat during the operation [16] [23] [24]. The relation between temperature and the V_{oc} will be discussed in chapter 2.3. Free carrier absorption strongly depends on the wavelength of the incident irradiance and carrier concentration in the silicon. Therefore, the effect of the free carrier absorption can be seen in the shape of the solar cell's Internal

Quantum Efficiency (IQE), especially at longer wavelengths. If the effect of FCA is ignored, this results in an overestimation in the IQE of the solar cell. For usual screen printed solar cell, FCA causes 2-3.5% decrease on IQE at near band gap [22]. The decline is stronger in higher doped solar cells.

In the classical theory of the free carrier absorption which is derived from Drude's model, FCA is linearly dependent on the concentration of doping and square of the wavelength [15].

$$\alpha_{FCA,n/p} = \frac{q^3 \lambda^2 N}{4\pi^2 \varepsilon_0 c^3 n m^{*2} \mu} \quad \textbf{Eq. 8}$$

where $\alpha_{FCA,n/p}$ is the free carrier absoprtion coefficient, λ is wavelength, q is the fundamental charge, N is the concentration of doping, ε_0 is the vacuum permittivity, c is the speed of light, n is the refractive index, m^* is the effective mass and μ is the carrier mobility. Schroder *et al.* [15] substituted the assumed material parameters and experimentally determined the free carrier absorption coefficient for the wavelengths 4, 5 and 10 µm.

$$\alpha_{FCA,n} \cong 1 \times 10^{-18} N_n \lambda^2 \quad \textbf{Eq. 9}$$

$$\alpha_{FCA,p} \cong 2.7 \times 10^{-18} N_p \lambda^2 \quad \textbf{Eq. 10}$$

where $\alpha_{FCA,n}$ and $\alpha_{FCA,p}$ are given in cm^{-1}, λ is given in µm and N_n and N_p are given in cm^{-3}. This parametrization is valid at $N < 10^{19}$ cm^{-3} and $\lambda > 4$ µm. However, in silicon solar cells near band gap region is between 1 µm and 1.5 µm. Also, doping concentration generally exceeds 10^{19} cm^{-3} and sometimes almost reaches 10^{21} cm^{-3}. Indeed, the validity of the parametrization of Schroder *et al.* [15] is limited for typical solar cells. Later, various authors [23] [25] [26] [27] worked for adopting a better model for free carrier absorption coefficient by following Schroder *et al.*'s [15] work. They defined two constants γ and $C_{n/p}$. The γ is assumed 2 by Drude theory but it is expected to increase slightly at high doping [22] [23]. The $C_{n/p}$ is dependent on the free carrier effective mass and mobility [28]. The resulting FCA coefficient depends on N and λ as following.

$$\alpha_{FCA,n/p} = C_{n/p} N \lambda^{\gamma} \quad \textbf{Eq. 11}$$

where $C_{n/p}$ is in cm^{-3} and γ is dimensionless. The most widespread and simple expression of free carrier absorption coefficient for wavelength smaller than 2.5 µm was introduced by Green [25].

$$\alpha_{FCA,n} = 2.6 \times 10^{-18} N_n \lambda^3 \quad \textbf{Eq. 12}$$

$$\alpha_{FCA,p} = 2.7 \times 10^{-18} N_p \lambda^2 \quad \textbf{Eq. 13}$$

Different than the Drude theory, free carrier absorption of the n-type doping silicon is dependent on the λ^3 which is corroborated by the parametrizations of Baker-Finch *et al.* [23] and Rudiger *et al.* [26] which have an exponent of wavelength near to 3.

For the polysilicon layer, more accurate parametrization is found by Feldman *et al.* [29]. This parametrization fits well for 90nm and 145nm thick and 1.9×10^{20} cm^{-3} n-doped polysilicon layer.

$$\alpha_{FCA,polysilicon,n} = 1.33 \times 10^{-7} N_n \lambda^{2.58} \quad \textbf{Eq. 14}$$

where λ is given in cm and N_n is given in cm^{-3}.

For most conventional monofacial cell Al-BSF, which is explained in detail in chapter 2.1, p-type is found in the bulk of wafer and n-type is found in the emitter. And in the bulk of the wafer p-type doping concentration is typically around 1×10^{16} cm^{-3} and in the emitter, the maximum n-type active doping concentration is typically around 3×10^{20} cm^{-3} and 0.2-0.3 µm deep. For these doping concentrations, the absorption coefficient of intrinsic silicon, p-type bulk, and n-type emitter are illustrated in Figure 11. At near band gap (1.1 µm), where band to band absorption is weak, FCA starts to dominate the total absorption in the solar cell. The FCA can start to dominate shorter wavelengths if doping concentration increases. As shown in Figure 11, at near band gap region, the absorption coefficient of the emitter is higher than 10^3 cm^{-1} while the absorption coefficient of the bulk is around 10^{-1} cm^{-1}. The FCA in the emitter is more dominant than the FCA in the bulk of the wafer due to higher doping. The FCA in the bulk is weak but it occurs over the entire depth of the bulk.

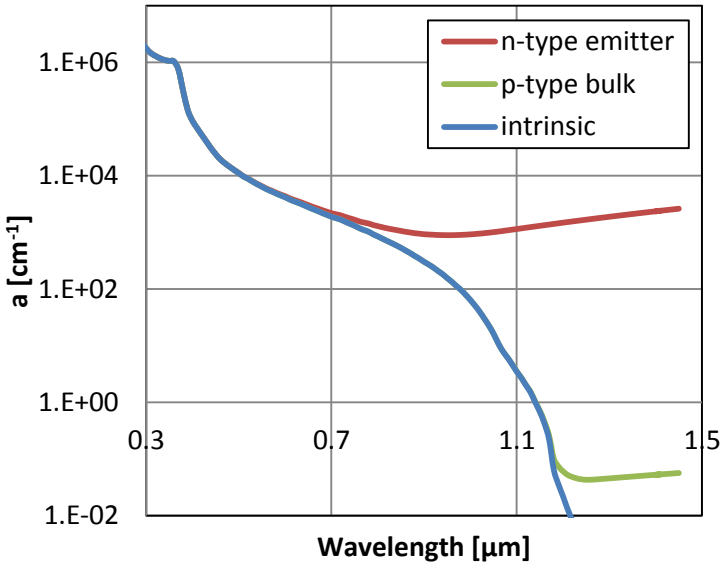

Figure 11: The absorption coefficient of the intrinsic silicon as a function of wavelength **[20]**, p-type 1×10^{16} cm^{-3} concentration doped bulk silicon and n-type 3×10^{20} cm^{-3} concentration doped emitter **[25] [30]**.

2.3. Heating of Solar Cell

There are several ways heat is generated in a solar cell. One of the primary heat source mechanism for solar cells is thermalization. Thermalization is the release of excess energy when an electron-hole pair is generated while the energy of the photon is higher than the band gap energy of the semiconductor. The released heat causes temperature increase in the cell. Short wavelength light has higher energy than the long wavelength light. Therefore, thermalization at shorter wavelengths is greater than thermalization at longer wavelengths and reduces to zero when the energy of the photon is same or lower than the band gap energy of the solar cell (Figure 12). For silicon, band gap energy is 1.1 eV which is 1100 nm.

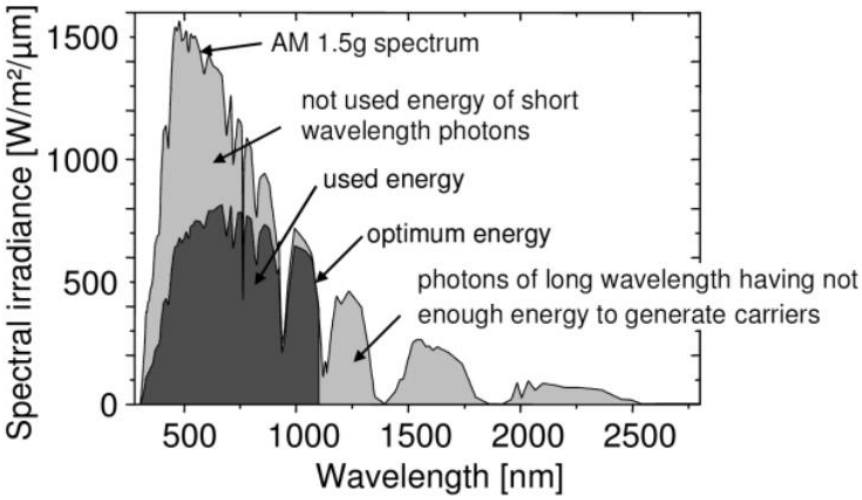

Figure 12: AM 1.5G solar spectrum with converted usable energy **[31]**.

Another heat source mechanism for solar cells is the parasitic absorption of the front and rear metallization. Since conventional solar cells have full area rear side metallization (large absorption area), the effect of the parasitic absorption by metallization is significant. The unabsorbed light through the solar cell hit the full aluminum back which is used as an electrical contact for the most conventional monofacial cell. The light is either reflected or absorbed. The average reflection of the Si/Al interface is around 77% [32]. The reflection from the aluminum rear increases the absorption probability of the light by the solar cell active area due to the increased path way of the light in a solar cell as mentioned before. Based on the conservation of the energy, the rest of the incident light on aluminum contact which is not reflected is absorbed by the aluminum contact. Around 10% of the sunlight (mostly above 1200 nm) is absorbed by the aluminum rear contact [33]. Since absorption of IR light through the solar cell is low, most of the IR light is absorbed by the aluminum back contact. According to Vogt [33], absorption by full aluminum rear contact increases the operational temperature of the solar cell by 3.2 ˚C compared to the solar cell which has SiN_x at the rear instead of the full aluminum contact. Another heating mechanism of the solar cell is absorption by the front metallization. Some of the incoming light hits the front metallization and it is either reflected or absorbed. The absorbed light by the metallization causes heat. However, the effect of the front metallization on the temperature of the cell is not as significant as the full area back contact because the area of the front metallization is only 5% of the total front surface which is very low compared to the solar cell active area.

The main effect of heat, resulting in a higher temperature, is on the open-circuit voltage (V_{oc}) of the solar cell. This effect can be calculated by using the following formula [34]

$$\frac{dV_{oc}}{dT} = -\frac{V_g - V_{oc} + \Upsilon(kT/q)}{T} \qquad \textbf{Eq. 15}$$

where V_{oc} is the open circuit voltage of the cell under STC, k is the Boltzmann's constant and equals to 1.380×10^{-23} J/K, T is temperature in Kelvin, q is elementary charge of an electron which is 1.602×10^{-19} C, Υ is constant(~3) [34] which depends on the temperature dependency

of other cell parameters and $V_g = E_g/q$ where E_g is the band gap of silicon (~1.12eV). Another parameter which affects V_{oc} of the solar cell is irradiance. By using the following

$$V_{oc}(T_{STC}, G_{eff}) = V_{oc}(T_{STC}, G_{STC}) + \frac{n_{ide.}kT_{STC}}{q} ln\left(\frac{G_{eff}}{G_{STC}}\right) \quad \textbf{Eq. 16}$$

where $n_{ide.}$ is the ideality factor of the solar cell and G_{eff} is the effective irradiance on the cell. Ideality factor is not a parameter that can be directly measured. It is from the IV characteristic data by using the one-diode model. Since total resistivity of the cell approaches to shunt resistivity at low voltages (low irradiances), ideality factor also approaches to 2 which makes the ideality factor not valid at low voltages [35]. Therefore, ideality factor assumed to be constant between 700 W/m^2 and 1200 W/m^2 which makes sense because effect of irradiance on the voltage at high irradiances is small.

The effective irradiance does not have to be equal to the observed irradiance by a reference cell in plane because some modules are bifacial and placed free standing. By using the direct relation between I_{sc} and the irradiance, the effective irradiance can be calculated as shown.

$$G_{eff} = \frac{I_{sc,meas}}{I_{sc,STC}} G_{STC} \quad \textbf{Eq. 17}$$

where $I_{sc,meas}$ is measured I_{sc} under any irradiance, $I_{sc,STC}$ is the I_{sc} under STC and G_{STC} is the STC irradiance which is 1000 W/m^2. Open circuit voltage at specific module temperature (T_{Module}) and irradiance can be calculated by using the next formula [18].

$$V_{oc}(T_{Module}, G_{eff}) = V_{oc}(T_{STC}, G_{eff}) + \frac{dV_{oc}}{dT}(T_{Module} - T_{STC}) \quad \textbf{Eq. 18}$$

With known irradiance, IV characteristics of the module and V_{oc} of the module under operating conditions, temperature of the module under operating conditions can be calculated by modifying the Eq.17.

$$T_{Module} = \frac{V_{oc}(T_{Module}, G_{eff}) - V_{oc}(T_{STC}, G_{eff})}{\frac{dV_{oc}}{dT}} + T_{STC} \quad \textbf{Eq. 19}$$

2.4. Heating of Solar Module

Absorptions which do not contribute to produce electron-hole pairs are called parasitic absorption which are module material absorption, free carrier absorption and absorption of the metal contacts. Heating in a solar module is also caused by the dissipation of power, due to resistance: $P_{diss.} = I^2R$. The heating due to parasitic absorption of the additional components to semiconductor is called parasitic heating. Also, module materials like glass, EVA and a back sheet, absorb light which generates heat. The heat is stored by the materials which increases the temperature of the module and cell, which affects the performance of the module. The thermal capacitance, which is the capability to store heat, of the module materials depends on the density (ρ) in kg/m^3, thickness (t) in m, surface area (A_s) in m^2 and specific heat capacity (c_h) of that material in J/K. The thermal capacitance (C_{th}) is defined in the following formula.

$$C_{th} = \rho c_h A_s t \quad \text{Eq. 20}$$

Since the solar cell is almost in the middle of the module and generates the most heat, heat transfers from the center of the module to the surrounding of the module. The module materials are resistive to the heat transfer. They should have low heat resistance to keep the temperature of the module as small as possible. The thermal resistivity of the materials depends on thermal conductivity of the material (k) in W/(m K) and various other parameters. The thermal resistance (R_{th}) of each layer to heat flow can be calculated by using the following formula.

$$R_{th} = \frac{t}{kA_s} \quad \text{Eq. 21}$$

2.4.1 Absorbing and Reflective Back Sheet

In the solar modules for different applications, absorbing and reflective back sheet can be used. White and black polymer back sheets are used as reflective and absorbing back sheet, respectively. The thickness of those back sheets is around 0.34 mm. The module configuration is glass/EVA/solar cell/EVA/back sheet as it can be seen in Figure 13.

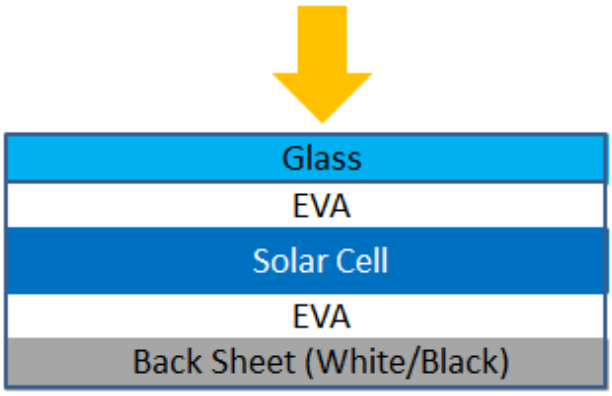

Figure 13: The configuration of module with back sheet.

Different to glass-glass modules, unabsorbed light through the solar cell cannot leave the solar module when it hits the black back sheet which has zero transmission rate for all wavelengths. It is either reflected or absorbed. Since white back sheet can partially transmit light after 500 nm, it is not opaque for all wavelengths. Hence, some amount of light can pass through the module with the white back sheet. Figure 14 shows the reflection (RFL) of white and black back sheet and the transmission (TM) of the white back sheet. For all wavelengths, the black sheet has around 95% absorption while the white back sheet has average 20% absorption.

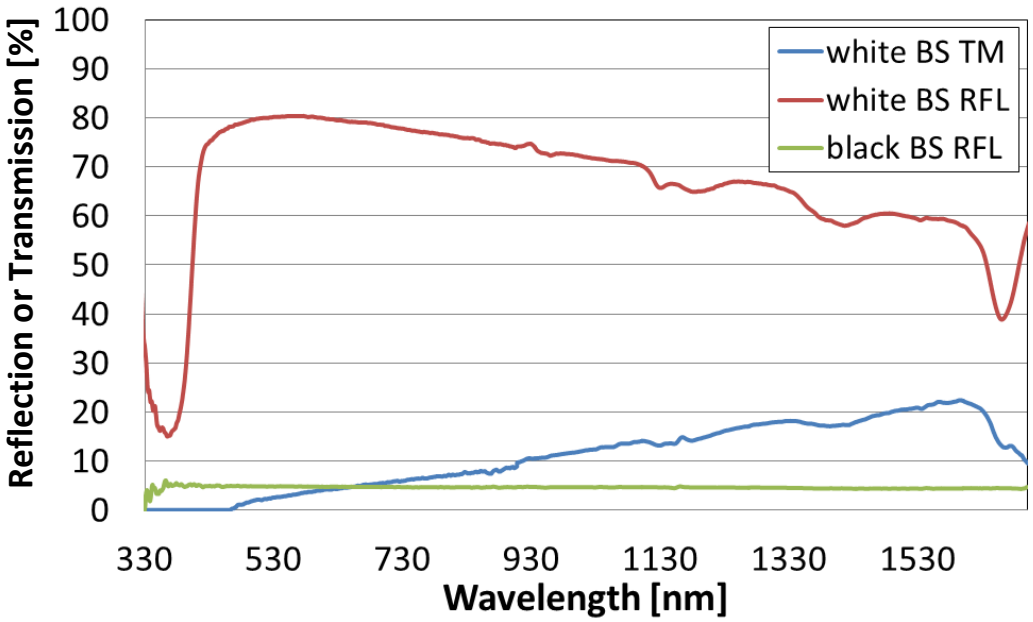

Figure 14: The reflection of white and black back sheets and transmission of the white back sheet.

The unabsorbed light through the solar cell and additional light which comes from the edge of the module may be reflected from the white back sheet and absorbed by the cell (Figure 15). Hence, the white back sheet causes illumination gain and increase the performance of the solar module with a bifacial solar cell. For modules with a black back sheet, this is not possible because the black back sheet is highly absorbing and reflects very less light which does not make a notable change in the performance of the module.

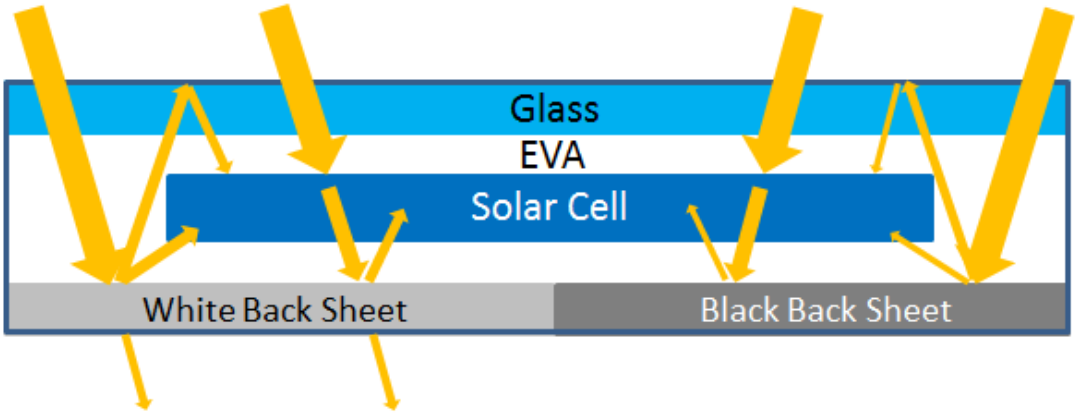

Figure 15: The light management of solar module with white and black back sheet.

The parasitic absorption of both back sheets causes parasitic heating and increase the temperature of the module. Since absorption of the black back sheet (95%) is higher than the absorption of the white back sheet (20%), higher parasitic heating is expected from a black back sheet. Moreover, for free standing applications, light also hit from the rear side of the modules. Incoming light from the back of the module affects the parasitic absorption and heating of the modules. Again, black back sheet is nontransparent while a white back sheet is partially transparent. Reflection of rear of the both back sheets and transmission of rear of the white back sheet can be seen in Figure 16. It should be noted that the rear side of the black back sheet (BS) is white. The front side of the black back sheet is black. For the white back sheet, both sides are white.

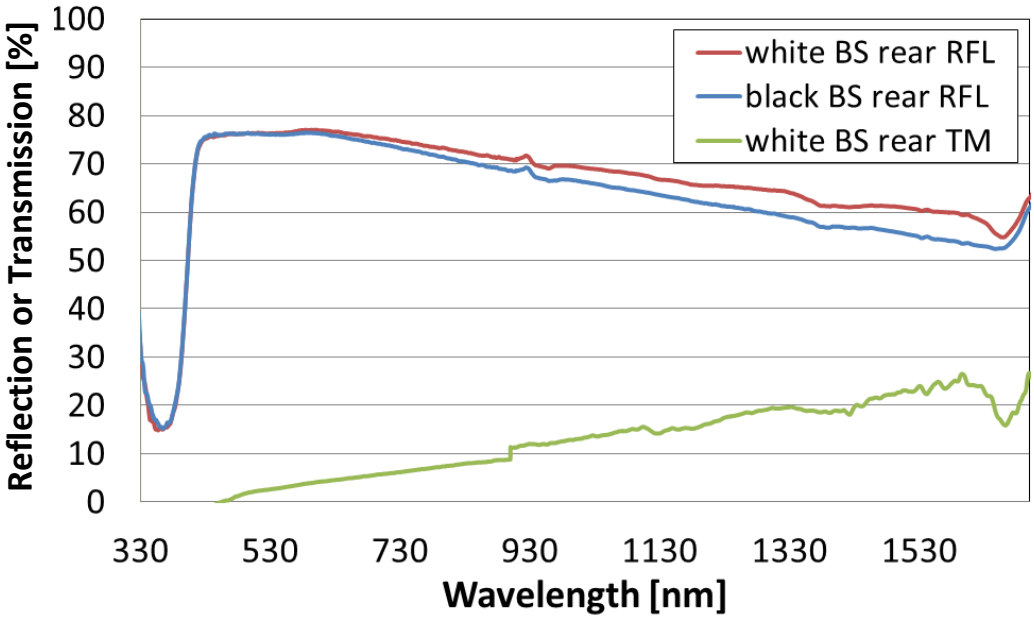

Figure 16: The reflection of white and black back sheets and transmission of the white back sheet for their rear sides.

Mostly, rear of white back sheet has higher reflection than rear of black back sheet. The difference between them is increasing while the wavelength is increasing. Also, transmission of the white back sheet increases with wavelength. Since white back sheet has higher reflection and transmission values, it has lower absorption. Therefore, the black back sheet has higher parasitic absorption when light only comes from the back. Additionally, a module with white back sheet has illumination gain from the rear side when it is free standing because the white back sheet is not nontransparent for all wavelengths.

2.5. Different Cell and Module Technologies

2.5.1. Al-BSF Solar Cell

As mentioned in chapter 2.1, the Al-BSF solar cell is most conventional solar cell type. The 243 cm^2 p-type Cz silicon wafer is used to produce Al-BSF solar cell (Figure 17). The n-doped 0.2-0.3 µm deep emitter layer is produced by diffusion of phosphorus. The highly doped BSF layer is formed by alloying the aluminum (Al) layer as a back contact. The SiN_x is used for passivation and anti-reflective purposes on the top of the cell which ensures that reflection minimum stays at around 600 nm wavelength. For the front contact, H-grid

metallization with three busbars is used by using aluminum as a material. Typical thickness of the cell is around 160 μm.

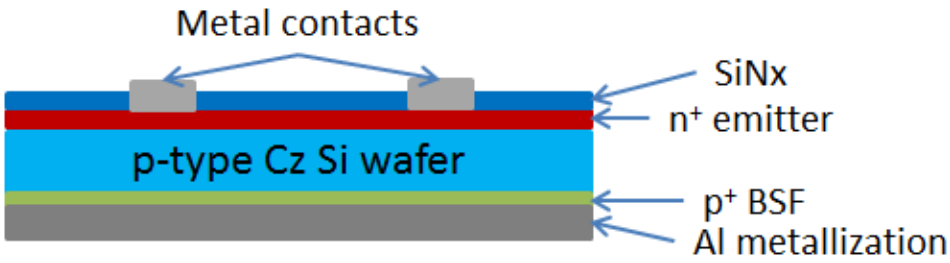

Figure 17: Configuration of the conventional crystalline silicon solar cell.

Due to the full back contact, unabsorbed light cannot pass through the cell. It is either reflected or absorbed in the Al layer. If the light is absorbed by full back contact which is parasitic absorption, back contact creates parasitic heating and increases the operational temperature of the cell. Because of this reason, highest parasitic heating and operational temperature are expected from Al-BSF solar cells.

2.5.2. n-Pasha Solar Cell

Some types of bifacial solar cells are developed by ECN to increase the efficiency with low cost. The n-Pasha cell is a n-type bifacial cell which can get light from both front and rear sides. The 6-inch semi-squared n-type Cz silicon wafers are used to produce 239 cm^2 n-Pasha bifacial cells [36]. The configuration of the n-Pasha cell can be seen in Figure 18.

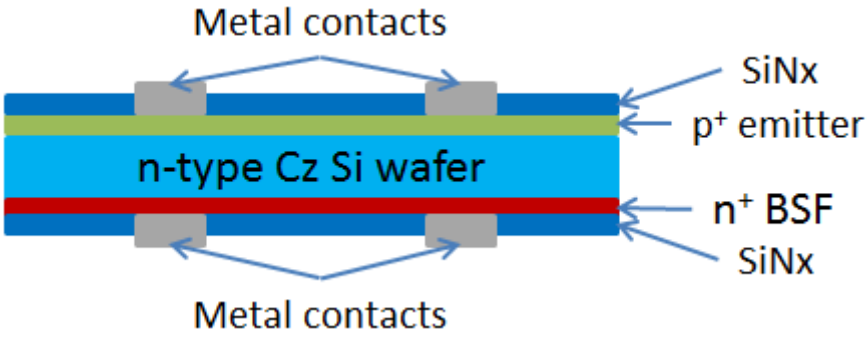

Figure 18: Configuration of the n-Pasha bifacial solar cell.

A 60 ohm/sq and 500 nm thick, p+ emitter layer produced by the diffusion of BBr_3 and the back surface field (BSF) is created by doping of the $POCl_3$ [36]. For the passivation and anti-reflective purposes, the SiN_x thin layer is used. Refractive index and the thickness of the SiN_x layer at the front are arranged for the minimum reflection at around 600 nm wavelength (thickness 70-80 nm). The metallization of the both sides are H-grid with four busbars and applied by screen printing [36]. The materials of the metallization for front and rear sides are Al/Ag and Ag, respectively. H-grid rear side makes possible bifacial application since light can also enter the cell from the rear side. Hence, there is gain from the back side on the efficiency of the cell [37].

Another advantage of the open rear metallization is the lower operating temperature of the cell compared to solar cells with full aluminum back contact [13] [14] [38]. The unabsorbed IR light can pass through the cell from the rear side which is not possible to pass

in the Al-BSF cell as mentioned before. Hence, lesser parasitic absorption, parasitic heating and operational temperature are expected in n-Pasha cell compared to Al-BSF cell. However, since bifacial cells can get light from the rear side, this additional light also needs to be considered while determining the temperature of the bifacial cell. The Al-BSF cell and n-Pasha cell have comparable front sides and the main difference between them is rear side metallization. Therefore, the main reason for the expected temperature difference is different rear metallization.

2.5.3. PERPoly Solar Cell

PERPoly (Passivated Emitter and Rear Polysilicon) cells are developed for high performance and low cost. It is very similar to the n-Pasha solar cell. The main difference compared to n-Pasha is the existence of a different BSF layer of the cell. Instead of n-doped conventionally diffused BSF layer, n+ polysilicon (polySi; LPCVD deposition of polySi and doped by diffusion afterwards) is used as BSF layer to decrease the rear passivation and improve the performance. 239 cm^2 n-type solar cells are produced on 6-inch wafers of 5 Ohm.cm [10]. A 70 ohm/sq and about 500 nm thick n+ emitter layer is produced by the diffusion of BBr3 [10]. H-pattern metal grid with four busbars is made by screen printing on both sides of the cell. The materials of the metallization for front and rear sides are Al/Ag and Ag, respectively. For anti-reflection and passivation purposes, SiN_x coating is used for both sides of the cell. Figure 19 shows the configuration of the PERPoly cell.

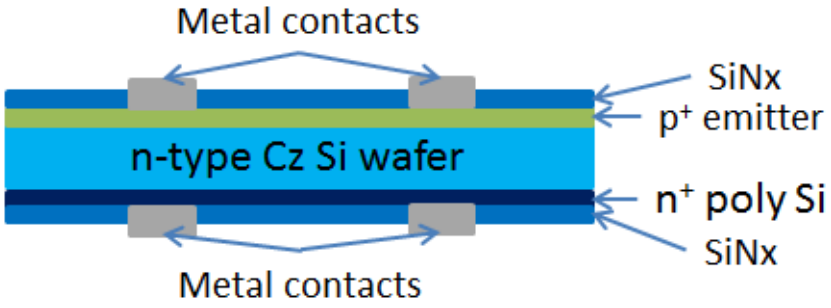

Figure 19: Configuration of the PERPoly bifacial solar cell.

The highly doped polySi layer causes higher absorption compared to the n-doped BSF layer of n-Pasha cell. Therefore, higher parasitic heating and operational temperature are expected in PERPoly cell compared to n-Pasha cell. In the project, two different types of PERPoly cells, which have 100 nm and 200 nm thick n-doped polySi layers with same doping levels at the back, are used. Higher parasitic absorption is expected from cells which have a thicker polySi layer. Hence, higher parasitic heating and operational temperature are expected from PERPoly cell with thicker polySi layer compared to PERPoly cell with a thinner polySi layer.

2.5.4. Jasmine Solar Cell

Jasmine solar cells are developed by ECN. These solar cells are 242 cm^2 p-type cell type which is an alternative for the PERC solar cells. The PERC solar cells are developed to enhance the performance of the conventional solar cells by changing the design of the back side of the typical Al-BSF cell (Figure 20). First of all, Al_2O_3 is used for passivation purposes to decrease recombination losses. In addition, there is no full area contact between aluminum

and silicon. As it can be seen from Figure 21, the electrical contact area is much smaller than the conventional Al-BSF cell. Before printing and firing Al paste, SiN_x is used as dielectric capping and passivating layer and laser cuts openings for Al contact [39]. With the passivation layer, unabsorbed light through the cell is reflected for a second chance to be absorbed. Also, it causes a reduction in recombination levels [40]. Therefore, PERC cells have better performance than standard cells. However, there are increased production costs to produce this high efficiency cell [41]. Hence, jasmine cells are developed which are planned to have same technology with cheaper production. In order to achieve this, SiN_x layer is removed, so the necessity for the laser cut of SiN_x is no longer needed (Figure 21) [17]. Both the absences of SiN_x and laser cut process lower the cost of the jasmine cells. In addition, lower consumption of Al paste and Al_2O_3 also decrease the cost of the production of the cell (Figure 21). In jasmine cells, H-grid metallization is used for both sides which are Ag and Al, respectively.

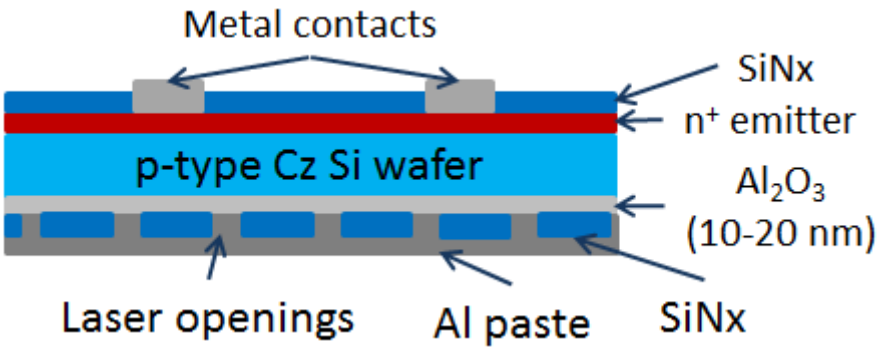

Figure 20: Configuration of the PERC solar cell.

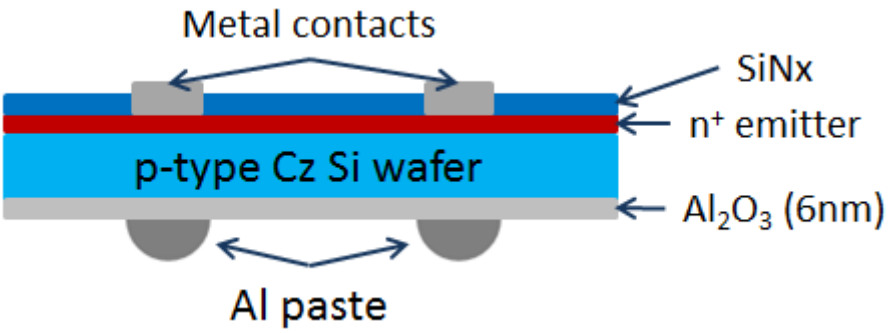

Figure 21: Configuration of the Jasmine bifacial solar cell.

Jasmine cells have textured front and smooth rear surface. The main difference compared to the previously mentioned cell types is at the back of the cell. The 6 nm Al_2O_3 is very thin and optically inactive for the infrared light. There is a big difference between the refractive index of silicon and EVA which are around 3.9 and 1.5, respectively [17]. Therefore, there is a high reflection for the jasmine solar cells. Since there is a great reflection, unabsorbed light through the solar cell may leave the cell after another pass. Hence unabsorbed light leaves the cell by reflecting from the rear instead of absorbed by the back contact. This causes a decrease in the parasitic absorption and parasitic heating of the cell. For these reasons, lowest parasitic heating is expected in the jasmine cells.

2.5.5. Module Designs

A bifacial and two monofacial module types were used for the project. The configuration of the bifacial module is Glass/EVA/Solar cell/EVA/Glass (Figure 22.a). The unabsorbed light through the solar cell can leave the solar module since rear side of the module is transparent. This configuration also allows illumination from the backside of the module. The advantage of the bifacial module configuration on the temperature is that unabsorbed light can leave the module with low absorption by module material. The configuration of the monofacial module is Glass/EVA/Solar cell/EVA/Back sheet (Figure 22.b). The unabsorbed light through the cell hits the back sheet which is either absorbing or reflective. White and black back sheets are used as reflective and absorbing back layers, respectively. Reflected light from the back sheet might be absorbed by the active part of the solar cell. Some part of the light is absorbed by the back sheet which causes parasitic heating. Therefore, higher parasitic heating and operational temperature are expected in the monofacial modules compared to the bifacial modules. Light management of the back sheets is mentioned in chapter 2.4.1.

Figure 22: Configuration of (a) the glass-glass module and (b) module with back sheet.

Glass-glass modules are built by using all five types of cells. However, for modules with a back sheet, only four types of cells were used which are the Al-BSF monofacial cell, n-Pasha cell, PERPoly (100nm) and jasmine. Table 2 shows the number of the single cell modules for each cell and module type.

Table 2: Number of single cell laminates for each cell and module type.

	n-Pasha	PERPoly 200nm	PERPoly 100nm	Jasmine	Al-BSF
Glass-Glass	1	2	3	2	4
White BS	2	-	2	2	3
Black BS	2	-	2	2	3

3. Heat Model

3.1. Heat Transfer

Incident light on the solar module is either reflected, transmitted or absorbed. It can be absorbed by any module material like glass, EVA or solar cell. Under the influence of the absorbed light, which does not generate electron-hole pairs, solar modules heat up. In reality, different than the standard test conditions (STC), the module temperature easily reaches around 45 ˚C in an ambient temperature of 20 ˚C. At higher temperature and higher incident conditions such as desert, the temperature of the module can reach up to 80-90 ˚C. The efficiency of the module decreases with temperature which is typically around 0.35 %/K [18]. Also, higher temperatures than STC temperature causes faster aging of the solar module.

As stated before, only 15-20 % of the incident light is converted into electricity and the rest is absorbed by module materials and cell but not generating electricity. The parasitically absorbed light generates heat and heats up the module. Similar to a sandwich, the solar cell is in the middle. Since solar cell is the main heat source in the module, it has the highest temperature and conveys its heat to the module components. The module is cooled down by the convective and radiative heat transfer mechanisms (Figure 23).

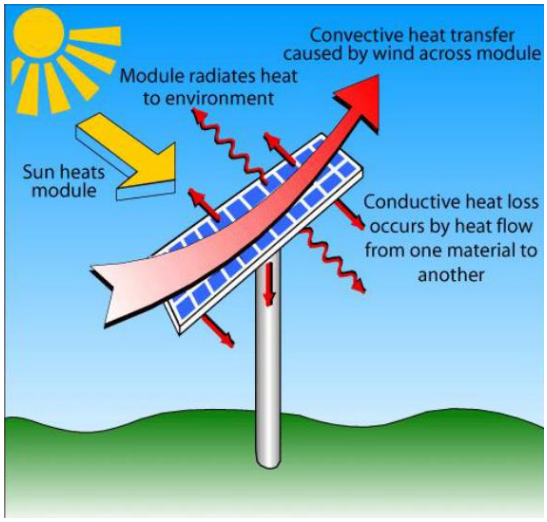

Figure 23: Heat transfer of PV module with convection, conduction and radiation **[42]**.

The first heat transfer mechanism is conductive heat transfer which occurs when a temperature gradient exists between mediums which allows heat to flow. The second heat transfer mechanism is convection and it occurs by the movement of the fluid; wind blowing along a module, lowering its temperature, is an example. The third heat transfer mechanism is radiative heat transfer. The module with a higher temperature than the surrounding temperature loses heat by radiating energy. In the next part, the mechanisms of heat transfer are explained in more detail.

3.1.1. Convective Heat Transfer

The convective heat transfer is caused by the movement of the fluid. In the modules, the transfer occurs between the glass (either front or rear) and air or between the back sheet

and air. The amount of the heat transfer by convection (Q_{conv}) can be expressed by the following equation.

$$Q_{conv} = h_{conv} A_s (T_M - T_A) \quad \text{Eq. 22}$$

where h_{conv} is the convective heat transfer coefficient in W/m^{2}K, A_s is the surface area in m^2, T_M and T_A are the module and ambient temperature in K, respectively. The convection can be either free or forced depending on the fluid motion. The free convection is independent on wind speed while the forced convection is dependent on wind speed. The relation between free convection heat transfer coefficient (h_{free}) and Nusselt (Nu) numbers is given by Fuentes *et al.* [43],

$$Nu = \frac{h_{free} D_h}{k} = 0.21(Gr \times Pr)^{0.32} \quad \text{Eq. 23}$$

where k is the heat conductivity of the air which is around 2.62×10^{-2} W/(m K) at 300 K [44], Pr is the Prandtl number which is the ratio of momentum diffusivity to thermal diffusivity and it is considered to be 0.71 [45] for air, and D_h is the hydraulic diameter of the module. The hydraulic diameter of a module can be calculated as below.

$$D_h = \frac{2LW}{L+W} \quad \text{Eq. 24}$$

where L is the length of the module and W is the width of the module. Gr is the Grashof number which can be calculated by using the following formula [46].

$$Gr = \frac{g\beta(T_{module} - T_{ambient}) D_h^3}{v^2} \quad \text{Eq. 25}$$

where g is the acceleration due to gravity on Earth which is 9.8 m/s, β is volumetric thermal expansion coefficient of air ($\beta \cong 1/T_{module}$) and v is the kinematic viscosity of the air which is considered to be 17×10^{-6} m^2/s [45]. By modifying the equations from above, free convection heat transfer coefficient (h_{free}) can be calculated by using following formula.

$$h_{free} = \frac{0.21k\left(\frac{g\beta(T_{module} - T_{ambient}) D_h^3 Pr}{v^2}\right)^{0.32}}{D_h} \quad \text{Eq. 26}$$

The forced heat transfer mechanism consists of laminar and turbulent heat flow. The forced heat transfer coefficient increases with increasing wind speed. There are two regions depending on the fluid motion which are laminar and turbulent region. For the laminar region Reynolds number should be lower than 3×10^5. If Reynolds number is higher than 3×10^5, flow is turbulent [46]. Finally, Re is the Reynolds number and it is expressed by [47]

$$Re = \frac{w D_h}{v}. \quad \text{Eq. 27}$$

where w is the wind speed at module height. The heat transfer coefficient of the laminar ($h_{forced}^{lam.}$) and the turbulent ($h_{forced}^{turb.}$) heat flow can be seen below [18] [43].

$$h_{forced}^{lam.} = \frac{0.86Re^{-0.5}}{Pr^{0.67}} \rho c_{air} w \quad \text{Eq. 28}$$

$$h_{forced}^{turb.} = \frac{0.028\mathrm{Re}^{-0.2}}{\mathrm{Pr}^{0.4}} \rho c_{air} w \quad \text{Eq. 29}$$

where ρ is the density of the air, c_{air} is the heat capacity of the air and w is the wind speed at the height of the module in m/s. The wind speed is measured by an anemometer where the height of it is different than the height of the module. The wind speed varies depending on the height. Therefore, by using the following formula, the measured wind speed can be scaled for the module height [43].

$$w = w_a \left(\frac{l_m}{l_a}\right)^p \quad \text{Eq. 30}$$

where w_a is the measured wind speed by the anemometer, p is the elevation factor, l_m and l_a are the height of the module and the anemometer, respectively. For the work shown in this thesis, all modules are free-standing in open country, for which an elevation factor of 1/5 can be used [43].

As described before, for the front side of the module, the total heat transfer coefficient represents the free and forced convection. The total convective heat transfer coefficient (h_{total}) can be calculated as follow [48]

$$h_{total} = \sqrt[3]{h_{forced}^3 + h_{free}^3}. \quad \text{Eq. 31}$$

3.1.2. Conductive Heat Transfer

In the module, there are two types of heat transfer by conduction. The first type of conduction is between the module and the surrounding. However, this heat transfer via conduction is assumed negligible due to the small contact area between the module and the mounting structure. The second heat transfer type by conduction happens within the module between the different layers which are glass, EVA, solar cell, and the back sheet. Each layer has its specific conductivity and absorbs some part of the incident light. They act as a heat source and thermal resistance between the solar cell and outer surface of the module. In the model which is developed in this work, the solar module is assumed as a single mass with uniform temperature, hence conductive heat transfer between the layers of the module is neglected.

3.1.3. Radiative Heat Transfer

The radiative heat loss also should be taken into consideration to determine the overall heat transfer from the module to the sky and the ground. The sky can be assumed as a blackbody and temperature of the sky (T_{sky}) is the function of the ambient temperature, humidity and cloud coverage. During the cloudy days, the sky temperature will be close to the ambient temperature. The sky temperature can be calculated as shown below [43] [49].

$$T_{sky} = 0.0552 \times T_a^{3/2} \quad \text{Eq. 32}$$

The ground temperature ($T_{gr.}$) is assumed to be equal to the ambient temperature (T_a) [1]. In nature blackbody does not exist so the PV module is considered as graybody. Therefore, the net radiation from the surface of the module occurs with emittance ε to the sky. The radiative heat transfer between the glass and the sky and between the glass and the ground can be expressed by Stefan-Boltzmann law [43].

$$Q_{rad} = \varepsilon\sigma A_s F_{sky/gr.}(T_{front/rear}^4 - T_{sky/ground}^4) \quad \textbf{Eq. 33}$$

where ε is the emissivity of the surface which is 0.91 for the glass [1] and 0.85 [2] for the back sheet, σ is the Stefan-Boltzmann constant which is around 5.670×10^{-8} W/(m^{2}K^4) and A_s is the surface area. $F_{sky/gr.}$ is the sky/ground view factor which can be calculated for the front and rear side of the module separately by the following equations [50].

$$F_{front,sky} = \frac{1}{2}(1 + cos(s)) \quad \textbf{Eq. 34}$$

$$F_{front,gr.} = \frac{1}{2}(1 - cos(s)) \quad \textbf{Eq. 35}$$

$$F_{rear,sky} = \frac{1}{2}(1 + cos(180 - s)) \quad \textbf{Eq. 36}$$

$$F_{rear,gr.} = \frac{1}{2}(1 - cos(180^\circ - s)) \quad \textbf{Eq. 37}$$

where s is the inclination of the module. The radiative heat transfer coefficient(h_{rad}) of front and rear surface of the module is expressed by

$$h_{rad,f,sky} = \varepsilon_f\sigma F_{front,sky}\left(T_{front}^2 + T_{sky}^2\right)\left(T_{front} + T_{sky}\right) \quad \textbf{Eq. 38}$$

$$h_{rad,f,gr.} = \varepsilon_f\sigma F_{front,gr.}(T_{front}^2 + T_{gr.}^2)(T_{front} + T_{gr.}) \quad \textbf{Eq. 39}$$

$$h_{rad,r,sky} = \varepsilon_r\sigma F_{rear,sky}\left(T_{rear}^2 + T_{sky}^2\right)\left(T_{rear} + T_{sky}\right) \quad \textbf{Eq. 40}$$

$$h_{rad,r,gr.} = \varepsilon_r\sigma F_{rear,gr.}(T_{rear}^2 + T_{gr.}^2)(T_{rear} + T_{gr.}) \quad \textbf{Eq. 41}$$

By using the radiative heat transfer coefficient, the thermal radiative heat resistance(R_{rad}) can be calculated by

$$R_{rad} = \frac{1}{h_{rad}A_s}. \quad \textbf{Eq. 42}$$

3.2. Fluid Dynamic Model

In this part, an accurate thermal model of the PV module, which is mainly dependent on the meteorological parameters, is introduced. We developed the fluid-dynamic model to estimate module temperature which is based on a detailed energy balance between the module and the surrounding environment. The model is dependent on the parameters of the module materials and surrounding parameters such as wind speed, irradiance and cloud cover. The model is mostly based on the model by Fuentes *et al.* [43].

Three types of heat transfer which were introduced are considered in the model. These heat transfers illustrated in Figure 24.

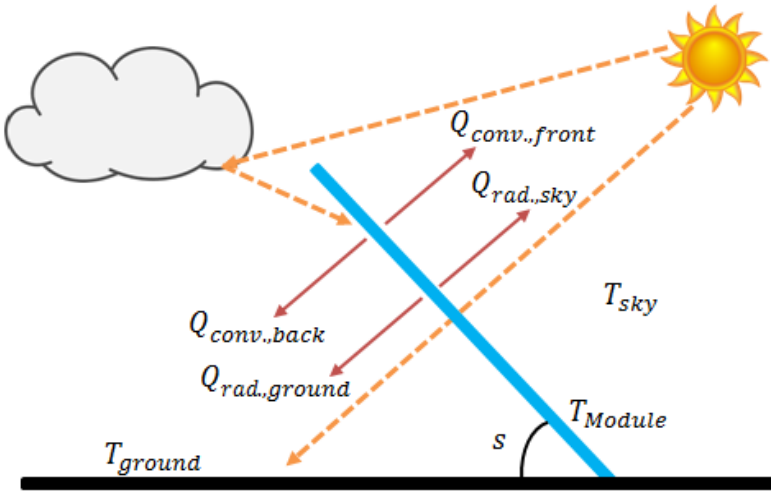

Figure 24: Heat transfer mechanism of PV module.

The model based on a one-dimension. In the model following hypotheses are used:

- The thermal exchanges by the module sides are negligible.
- The ambient temperature (T_A) assumed same all side of the module.
- The absorbed solar radiation by module, which is not converted to electrical energy, is assumed thermal energy.
- The solar module is considered as single mass with uniform temperature (T_M).
- The conductive heat transfer between the module and the surrounding is negligible due to a small contact area between the module and the mounting structure.
- The heat transfer by convection from the top of the module is dependent on the wind speed. Both free and forced convections are considered.
- The heat transfer by convection from the bottom of the module is also dependent on the wind speed because the modules are placed around 1 meters above the roof. Both free and forced convections are considered for back side of the modules.

By considering the contribution of the mentioned heat transfer mechanisms [43], the heat transfer balance can be written as below. Since some modules are bifacial, irradiance

gain from the rear side of the module is added to the heat balance which is different from the work by Fuentes *et al.* [43].

$$mc\frac{dT_M}{dt} = absorption_f + absorption_r - convection_f - convection_r - radiation_f - radiation_r \quad \textbf{Eq. 43}$$

$$mc\frac{dT_M}{dt} = \alpha_f G_f + \alpha_r G_r - h_{conv,f}(T_M - T_a) - h_{conv,r}(T_M - T_a) - h_{rad,f,sky}(T_M - T_{sky}) - h_{rad,f,gr.}(T_M - T_{gr.}) - h_{rad,r,sky}(T_M - T_{sky}) - h_{rad,r,gr.}(T_M - T_{gr.}) \quad \textbf{Eq. 44}$$

where m is the mass of the module per unit area, c is the specific heat of the module, α_f and α_r are the thermal absorption of the front and rear side, respectively, G_f and G_r are incident illumination on the front and rear side of the module, respectively.

In reality, the changes in the temperature due to varying irradiance do not occur immediately. The variations in the solar irradiance are faster than the changes in the temperature of the module. Therefore, the changes in temperature lag the solar irradiance variations. Each module has a time constant which shows the time for the module reach 63% of the total change in temperature due to a step change in solar irradiance [48]. The time constants of the modules are around seven minutes [18]. If the time step of the model exceeds the time constant of the module, the module can be considered in a steady-state condition. Our model evaluates the module temperature every 10 minutes so it can be regarded as steady-state. Therefore, the left side of the heat balance equals to zero like shown below.

$$0 = \alpha_f G_f + \alpha_r G_r - h_{conv,f}(T_M - T_a) - h_{conv,r}(T_M - T_a) - h_{rad,f,sky}(T_M - T_{sky}) - h_{rad,f,gr.}(T_M - T_{gr.}) - h_{rad,r,sky}(T_M - T_{sky}) - h_{rad,r,gr.}(T_M - T_{gr.}) \quad \textbf{Eq. 45}$$

By modifying this equation, the temperature of the module can be calculated as below.

$$T_M = \frac{\alpha_f G_f + \alpha_r G_r + T_a(h_{conv,f} + h_{conv,r}) + T_{sky}(h_{rad,f,sky} + h_{rad,r,sky}) + T_{gr}(h_{rad,f,gr} + h_{rad,r,gr})}{h_{conv,f} + h_{conv,r} + h_{rad,f,sky} + h_{rad,f,gr} + h_{rad,r,sky} + h_{rad,r,gr.}} \quad \textbf{Eq. 46}$$

The thermal absorption of the module defines the fraction of the converted thermal energy in the module. The absorptivity highly depends on the efficiency, reflectivity and transmission of the module. For the monofacial modules, since light cannot pass through the monofacial module, transmission of the module is zero. Below, calculation of the thermal absorption ($\alpha_{th.}$) of a module can be seen.

$$\alpha_{th.} = (1 - R - T - \eta) \quad \textbf{Eq. 47}$$

where R and T are the total reflection and transmission of the module, respectively and η is the efficiency of the module depending on the predicted module temperature.

4. The Experimental Setup

4.1. Building of the Modules

After the cell measurements, the solar cells that are mentioned in chapter 2.5 were used to build single cell modules. First of all, 1 mm and 5 mm wide tabs were soldered as busbar and cross connector to make the electrical contact of the module, respectively. Two probes were soldered with two polarities each (four probes per single cell module) to measure the current and the voltage separately which allows 4-probe measurement method for more accurate measurements. As mentioned in chapter 2.5, the configuration of the glass-glass module is Glass/EVA/Solar cell/EVA/Glass. The glasses have 3 mm thickness with dimensions 20 cm × 20 cm. 450 μm thick EVA (ethyl vinyl acetate) was used as an encapsulant material for moisture resistance and electrical isolation for both sides of the cell. For the modules with a back sheet, the configuration is Glass/EVA/Solar cell/EVA/Back sheet as mentioned before. As a back sheet, thin polymer was used which has 0.34 mm thickness. It is either white or black depending on the application. The back sheet prevents the module from moisture and acts as an electrical insulator. All sandwiches were heated up to 150 ˚C by the laminator. Hence, EVA is polymerized and keeps the module together. After indoor measurements of the modules, measurement cables for outdoor measurement were soldered to cross connectors which are used for the electrical contact. Also, all open connections are sealed to prevent any water leakage and corrosion during the outdoor measurement.

4.2. IV Measurement

IV characteristics of the cells are measured by using class AAA Wacom solar simulator under standard test conditions (STC) (1000 W/m^2 with AM1.5G spectrum, 25˚C). The irradiance level of the simulator is adjusted by using a calibrated reference cell. The size of the reference cell is comparable to the size of the sample cell. The light source homogeneously illuminates cells with the help of lenses. The temperature of the cell is controlled by a water cooling system and measured by the software.

IVs of the solar modules are also measured by the PASAN IIIb sun simulator under STC. It is a category “class A” flash tester according to IEC 60904-9 which is required for solar simulators. In order to adjust the temperature of the modules to 25˚C, the modules are left in the PASAN room which is always 25˚C with the help of the heating system. According to the doping type (n- or p-type), the setup is calibrated by using reference module. In order to avoid possible inhomogeneity of the light source in the calibration, the size of the reference module should be as close as possible to the size of the sample modules. Therefore, the four cell monocrystalline solar module was used as the reference module to calibrate the setup. Depending on the cell type of the modules, one, four or eight flashes are sufficient to get the required IV data. The modules are placed perpendicularly to the light beam (Figure 25.a). Each side of the modules is measured separately and for all measurements, the back side of the module is covered by a black sheet to prevent any light gain (Figure 25.b). A temperature sensor is placed with a piece of tape at the back of the module to measure the module temperature.

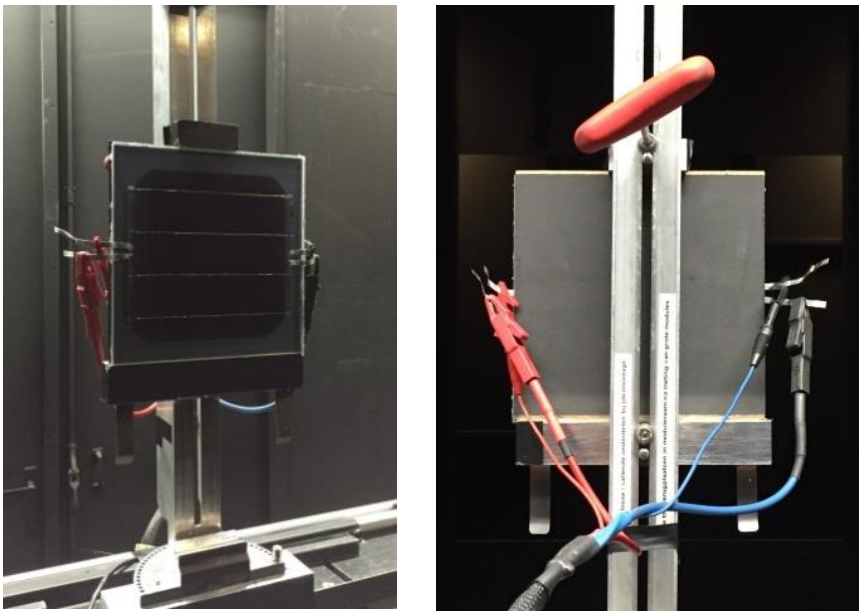

Figure 25: (a) Placement of solar module for PASAN measurement. **(b)** Black sheet to prevent any incident light from the rear side.

4.3. Reflection and Transmission Measurements

Spectral reflection and transmission of the cells, modules and module materials are measured by using the optical setup which is able to measure direct and diffuse light. The Labsphere RTC 060 SF is used as integrating sphere which is coated with high reflective and white Spectraflect. The light intensity in the sphere is measured by the Stellarnet twin detectors as a function of wavelength according to ASTM 424-71. The usual limits of the setup are between 330 nm and 1400 nm. The configuration of the setups for reflection and transmission measurements is shown in Figure 26.

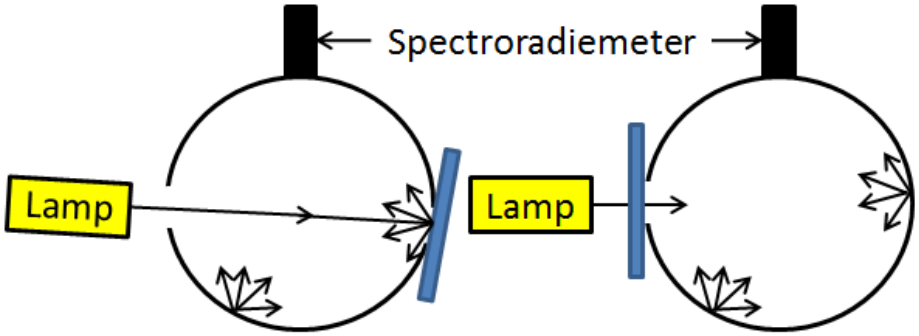

Figure 26: Optical configuration of reflection and transmission measurements.

There are a couple of ports which are used depending on the mode of the measurement. In the reflection mode, the light enters through the entrance port into the integrated sphere and illuminates the sample under an 8˚ angle (Figure 26). The lamp is focused on the sample port where the sample is located. The sphere collects the reflected light from the sample and the intensity of the light is measured by the Stellarnet twin detectors. In order to replicate the chuck of the spectral response or Wacom measurements, a foil with the same color of the chuck is placed to the back side of the sample during the reflection measurements (Figure 27).

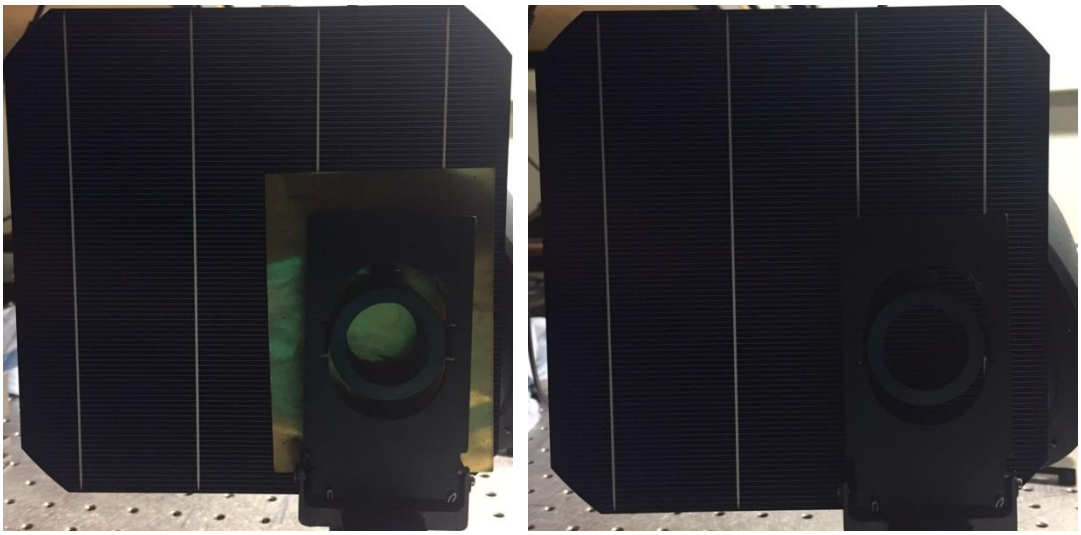

Figure 27: Placement of the solar cell samples with and without foil.

In the transmission mode, a sample is placed on the entrance port (Figure 26). The lamp is focused on the sample and illuminates it perpendicularly to minimize the reflection. Transmitted light through the sample is captured by the sphere and intensity of the transmitted light is measured by the detectors. Since the ports are too small to measure the entire surface of the sample, two different spots are measured for both measurement modes. Those spots are selected according to homogeneous distribution over the surface and placing them on busbars should be avoided (Figure 28). Hence, total spectral reflection and transmission can be estimated by averaging over two spots.

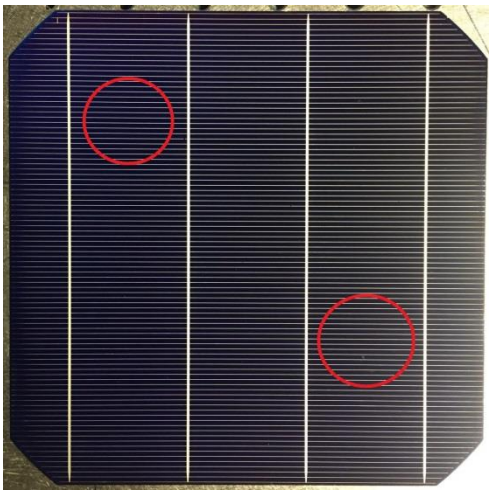

Figure 28: Measurement spots of the cell for homogeneous distribution.

4.4. Spectral Response Measurement

Spectral response measurement gives information on the performance of a solar cell and module as a function of the wavelength of the incident light. The measurement setup can be seen in Figure 29.

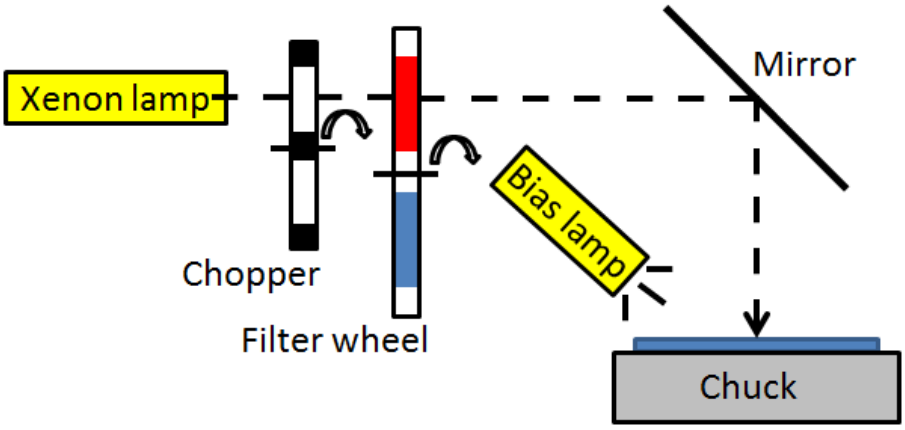

Figure 29: Configuration of the spectral response(SR) measurement setup.

The high power xenon light is used as a main lamp for the measurement. The other four small light bulbs are used for bias light, which keep the cell in the operational condition and adjust to produce a DC current that corresponds with about 0.5 sun. The chopper is used to maintain the light frequency at about 70 Hz which enables the lock-in amplifier to discriminate the signal caused by the filtered light and bias light. Hence, the measured signal does not consist of the bias light and electronic noise. The filter wheel contains 32 optical band pass filters which have different wavelengths from 330 nm to 1200 nm. The system measures the signal of each filter separately by the rotation of the filter wheel. The setup can be used to measure the spectral response of the cell and the module (Figure 30). The only difference between measuring a cell and a module is the way of being contacted with the samples. For the modules, crocodile clips are used instead of Kelvin probes which are used for the cells (Figure 30).

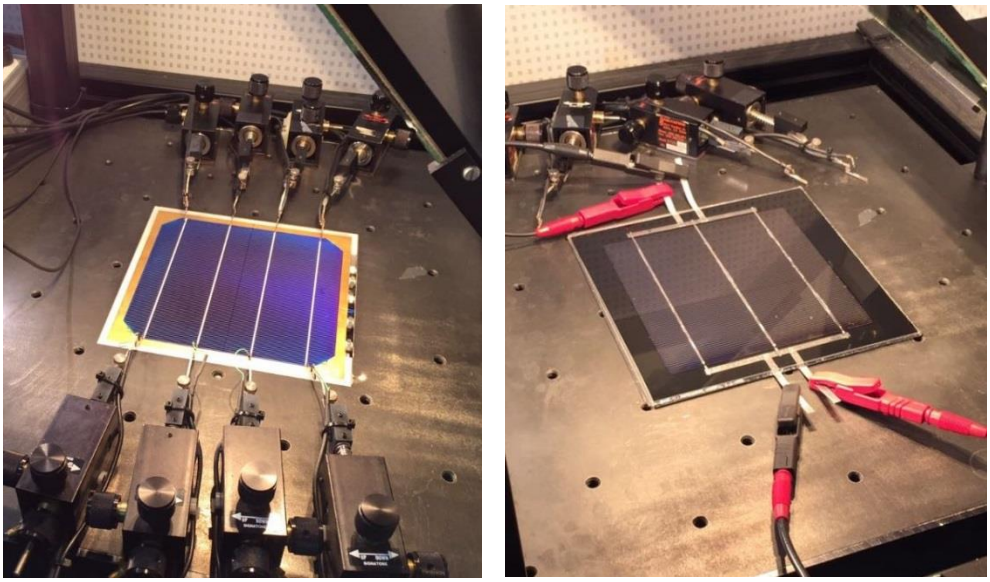

Figure 30: SR measurement of (a) a solar cell and (b) a solar module.

The measured signal gives information about the spectral response (SR) of the cell and the module on various loss mechanism. The response of short wavelengths, long wavelengths and overall response, provide the information about the front surface recombination, the rear surface passivation and diffusion length in bulk, respectively. The SR results show the current

density for 1 W/m^2 irradiance. The external quantum efficiency (EQE) and internal quantum efficiency (IQE) of the sample can be determined by the ECN program which needs SR, spectral reflection with foil, IV measurement by Wacom, total metallization coverage, metal fingers coverage and reflection curve of the metal grid. The EQE gives the number of collected electrons per incident photon, and it does not need reflection measurement of the sample cell. The IQE gives the number of collected electrons per absorbed photon in the cell. For the IQE, reflection measurement of the sample with foil at the back side of the sample is needed to mimic the chuck of the SR and Wacom setup.

4.5. Outdoor Measurement Setup

A 6×6 rack was prepared to measure 36 single cell laminates together as it can be seen in Figure 31.

Figure 31: Outdoor measurement setup.

The bottom row of the rack is 50 cm high from the ground with 0˚ azimuth angle (assuming South is 0˚) and 30˚ tilt angle in order to get highest yield during a year. The measurement boxes of the modules were placed next to the rack at each row to keep the measurement cables short for series resistance. Figure 32 shows the position of each module with the type of the cell and module on the rack. Modules, which have the same module type but different cell types, are placed close to each other in order to minimize the impact of their positioning on the measurement results (wind, shading for bifacial modules, etc.). Eight of the modules are measured by active outdoor IV measurement setup which is indicated in pink at Figure 32. In 10 minute intervals, active measurement system measures V_{mpp}, I_{mpp}, I_{sc}, V_{oc} and temperature of only the eight modules.

Left	1	2	3	1	2	3	Right
A	Perp (100nm) g-g	Jasmine g-g	Perp (200nm) g-g	Jasmine b-BS	F-Al b-BS	Perp (100nm) b-BS	
B	Perp (100nm) g-g	F-Al g-g	n-Pasha g-g	n-Pasha w-BS	F-Al w-BS	Perp (100nm) w-BS	
C	F-Al w-BS	F-Al g-g	Jasmine w-BS	n-Pasha w-BS	F-Al w-BS	Perp (100nm) w-BS	
D	F-Al b-BS	Perp (100nm) b-BS	Jasmine b-BS	n-Pasha b-BS	Jasmine w-BS	F-Al g-g	
E	**EMPTY**	F-Al b-BS	n-Pasha b-BS	Reference cell	b-BS IR reflecting module	**EMPTY**	
F	Perp (100nm) g-g	Perp (200nm) g-g	Jasmine g-g	F-Al g-g	w-BS module	b-BS module	

Figure 32: Position of the modules on the rack.

The rest of the modules, which are not measured by active measurement, are measured by passive outdoor IV measurement. Both active and passive measurements happen every 10 minutes. The passive outdoor measurement system is shown in Figure 33.

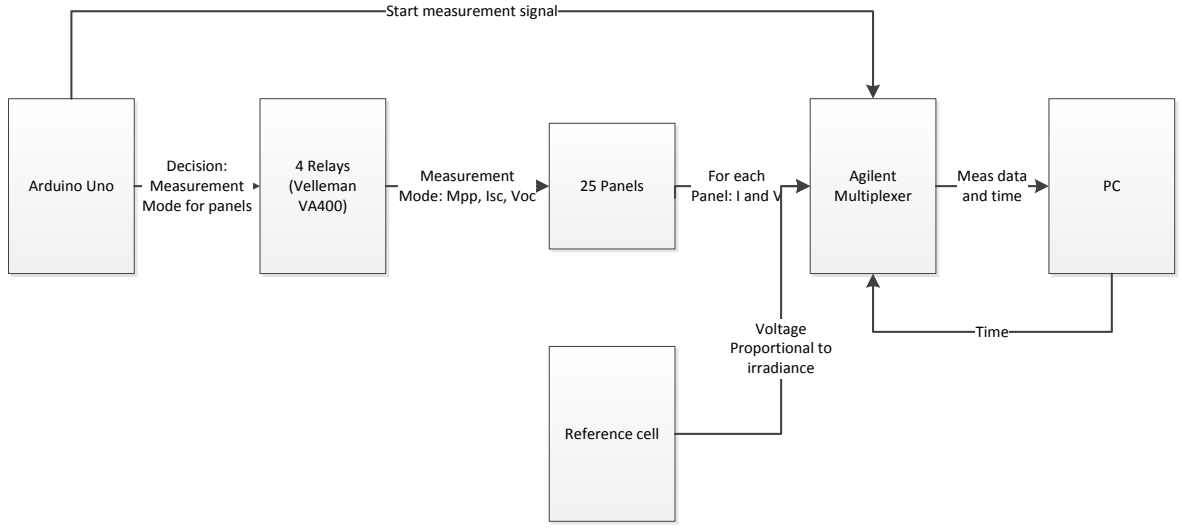

Figure 33: Abstract scheme of the passive outdoor measurement system **[51]**.

The working principle of the passive measurement system is different from the active measurement system. It measures each mode (Maximum Power Point (MPP), V_{oc} and I_{sc}) separately with time difference between them. The time and mode of the measurement are decided by the Arduino. First, the system measures I and V under MPP mode, after some time it measures I and V in I_{sc} mode [52]. Due to the cable resistances, real I_{sc} cannot be measured but can be approached. Finally, it measures I and V in V_{oc} mode. Both I and V are measured in I_{sc} and V_{oc} modes to confirm whether the measurements are real I_{sc} and V_{oc} measurements.

The reference cell is used to measure front irradiance which is placed on the same plane as the cells to be characterized. The front irradiance is measured six times to confirm if the weather is clear enough for a reliable measurement at each mode type. Hence, for a total measurement, the front irradiance is measured eighteen times. The researcher checks the differences between the eighteen irradiance measurements to decide if the measurement is reliable or not. The system is expected to be more reliable on sunny days with open sky.

The passive measurement setup is fully functional after 6th of September. However, the active measurement setup is fully functional from 18th of October. The data from the active measurement setup is only used for understanding the effects of environmental conditions (front irradiance, rear irradiance, ambient temperature and wind speed) on the module temperature and verifying the fluid dynamic model. For the outdoor analyses, modules which are measured by passive measurement setup were used because they are fully functional for a long time.

5. Results and Discussion

5.1. Analysis of the Cells

IV characteristics, spectral reflection, spectral transmission and spectral response of couple of cells were measured. Most comparable cells for each cell type were selected in order to be used in the project. Since the measurement results of the same type of cells are similar between each other, only measurement of one cell per each cell type are mentioned in this chapter. Table 3 and 4 show the IV characteristics measured at front and rear side of the different cell types, respectively.

Table 3: IV values of different cell types.

	J_{sc} [mA/cm^2]	V_{oc} [V]	FF [%]	Efficiency [%]	Bifaciality factor [%]
Al-BSF	37.2	0.631	79.5	18.6	-
n-Pasha	38.9	0.657	79.9	20.4	90.2
PERPoly 100nm	39.3	0.676	79.1	21.0	87.1
PERPoly 200nm	39.0	0.676	78.5	20.7	81.6
Jasmine	38.6	0.631	76.6	18.9	58.2

Table 4: IV values of rear side of different cell types.

	J_{sc} [mA/cm^2]	V_{oc} [V]	FF [%]	Efficiency [%]
n-Pasha	35.8	0.655	79.4	18.4
PERPoly 100nm	34.4	0.672	79.3	18.3
PERPoly 200nm	32.0	0.670	78.9	16.9
Jasmine	22.5	0.631	79.0	11.0

Al-BSF cell has one of the lowest V_{oc} due to the existence of full area aluminum-doped BSF and Al contact which cause lower quality surface passivation at the rear. The next lowest V_{oc} generated by the jasmine cell which is also caused by the lower quality of the local back surface fields (BSF). Both PERPoly cells have the highest V_{oc} due to the improved passivation by the n+ polysilicon which is used as BSF layer. Additionally, J_{sc} of the jasmine cell is higher than J_{sc} of Al-BSF cell due to improved internal reflections by reflective rear chuck during measurment. Since n+ polysilicon layer has higher doping level than the n+ BSF layer of n-Pasha cell, PERPoly cells have lower J_{sc} (PERPoly 100nm & 200nm: 34.4 mA/cm^2 & 32 mA/cm^2) than n-Pasha cell (35.8 mA/cm^2) when the cells are illuminated from rear side. Therefore, bifaciality factor of the n-Pasha cell is higher than bifaciality factors of the PERPoly cells (Table 3). Also, bifaciality factors of PERPoly cells decrease with thicker polysilicon layer due to higher absorption by polysilicon which decreases the rear J_{sc} value. Figure 34 shows the internal quantum efficiency (IQE) of the same cells.

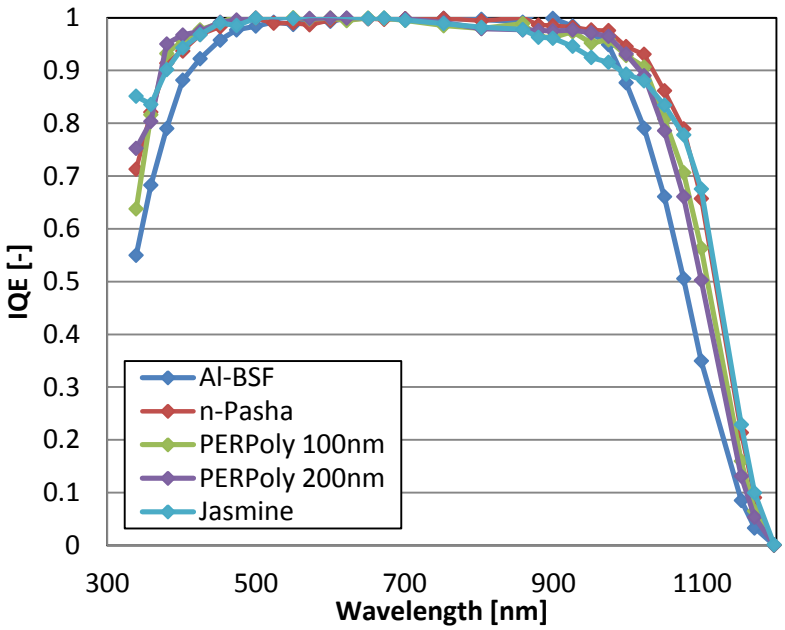

Figure 34: IQE of the different cell types.

As it can be seen in Figure 34, all bifacial cells have similar blue response but Al-BSF cell has lower blue response than other cell technologies which might be due to the poorer front surface passivation of Al-BSF cell compared to the other cells. The rest of the IQE rates of the cells are similar until the red response which shows the rear quality of the cells. Figure 35 shows more detailed red and near-infrared (near IR) IQE response of the cells.

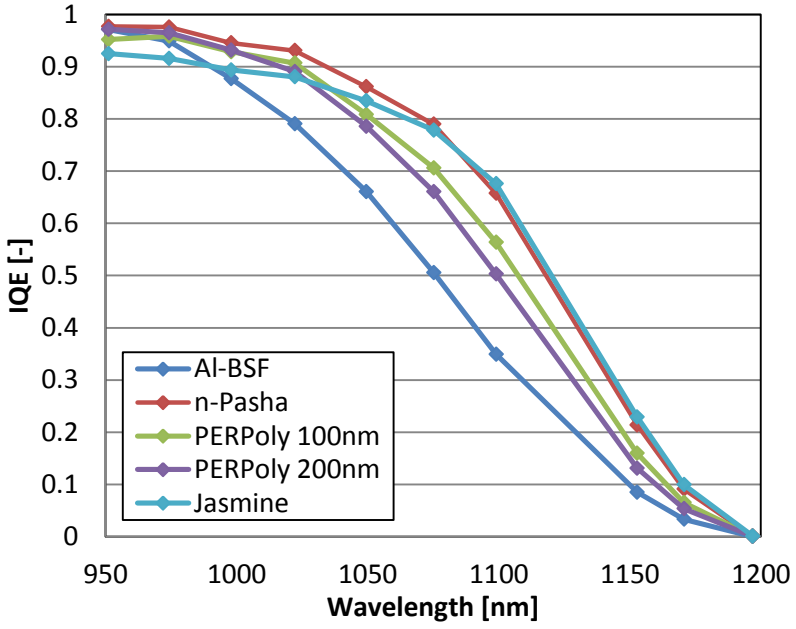

Figure 35: IQE response of the different cell types between 950 nm and 1200nm.

The Al-BSF (dark blue) cell has the lowest rear response due to the existence of full aluminum back contact which causes higher surface recombination and parasitically absorption of IR light. The effect of the full aluminum back contact is also seen on the V_{oc} of the Al-BSF cell as mentioned earlier. PERPoly cells (purple and green) have the second and

third poorest rear response due to highly n+ polysilicon layer which causes high free carrier absorption (FCA). The PERPoly 100nm has higher response than PERPoly 200nm because thicker layer parasitically absorbs more IR light than thinner layer. Since n+ BSF layer of n-Pasha is less doped than n+ polysilicon layer of PERPoly, lower FCA from n-Pasha cell is expected compared to PERPoly cells. Therefore, n-Pasha cell (red) has higher red response than PERPoly cells. As explained in chapter 2.5.4, the jasmine cell (light blue) has non-doped very thin passivation layer (6 nm) and high IR reflective back side which causes the lowest parasitic absorption at the back of the jasmine cell. Therefore, the jasmine cell has the one of the highest IQE red response. Figure 36 shows the spectral reflection (RFL(λ)) and 1-transmission (1-TM(λ)) of the cells. Due to the conservation of the energy the gap between RFL(λ) and 1-TM(λ) gives the spectral absorption (ABS(λ)) of the cells which are indicated by colored arrows for near IR region.

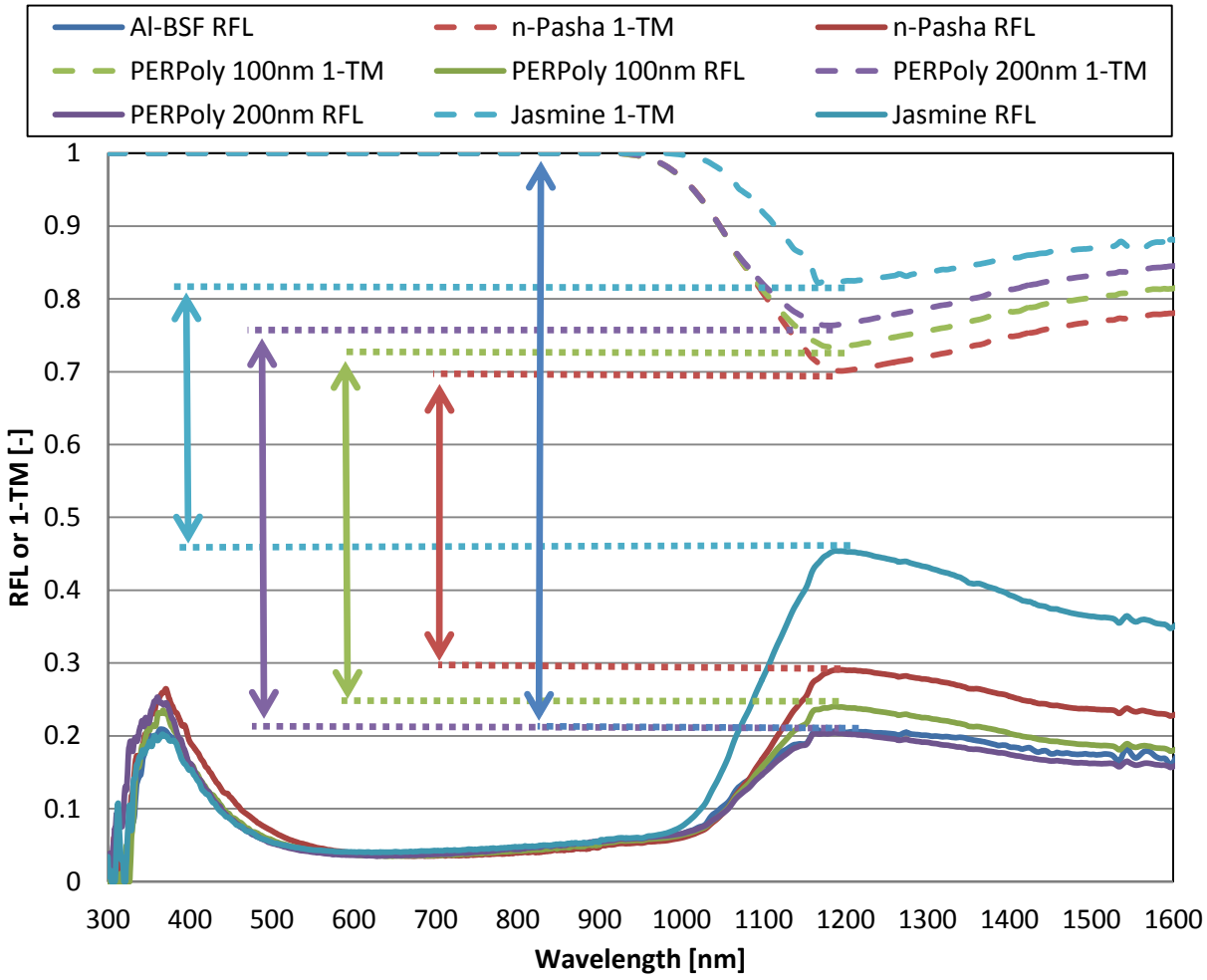

Figure 36: Reflection and 1-transmission of the different cell types. The arrows show the absorption rate at 1180nm.

The cells have comparable reflection rates until the near IR region which is mainly because of the different rear side designs (Figure 36). Since the jasmine has smooth and very thin passivation layer (6 nm), the passivation layer is optically inactive. The jasmine cell has the highest reflection (Si(~3.5)/air(~1) interface) at near IR region. Due to the high reflection, transmission of the jasmine cell at near IR region is low. The lowest absorption is expected from the jasmine cell at near IR (light blue arrow) which is ~36.9% at 1180 nm because of the

high reflection of the cell. The Al-BSF cell (dark blue arrow) has the highest absorption (~79.1% at 1180 nm) at near IR region due to the full area back contact which absorbs non-absorbed IR light through the cell. Also, it has the lowest reflection with the PERPoly 200nm cell. The PERPoly 200nm cell has the second largest absorption at near IR region which is due to the thicker and highly doped polysilicon layer. Due to the thicker doped polySi layer of the PERPoly 200nm cell as compared to the PERPoly 100nm cell, PERPoly 200nm cell has lower reflection and transmission than the PERPoly 100nm cell. Hence, PERPoly 100nm cell (~49.3% at 1180 nm) has less absorption than the PERPoly 200nm cell (~55.8% at 1180 nm) at near IR region (green and purple arrows). The n-Pasha cell has higher reflection and transmission than the PERPoly cells because of the absence of highly doped polysilicon layer. Hence, n-Pasha (red arrow) has the second lowest absorption (~41% at 1180 nm) at near IR region.

5.1.1. Expected Heat Inputs of the Cells

Expected spectral heating of the cells were calculated by using AM1.5G global (ASTMG173) standard solar spectrum ($S(\lambda)$), IQE response, spectral reflection ($RFL(\lambda)$) and transmission ($TM(\lambda)$) values of the cells. Spectrum of the reflection ($I_{RFL}(\lambda)$) and transmission ($I_{TM}(\lambda)$) in W/(m^{2}μm) calculated by using the following equations.

$$I_{RFL}(\lambda) = S(\lambda) \times RFL(\lambda) \quad \text{Eq. 48}$$

$$I_{TM}(\lambda) = S(\lambda) \times TM(\lambda) \quad \text{Eq. 49}$$

Due to the conversation of energy, absorption of the cells is calculated by

$$I_{ABS}(\lambda) = 1 - I_{RFL}(\lambda) - I_{TM}(\lambda). \quad \text{Eq. 50}$$

The absorbed value includes electrical output ($I_{Elect.}(\lambda)$), thermalization ($I_{Therma.}(\lambda)$), recombination, entropy and resistive losses ($I_{Rec.,Entr.,Resis.}(\lambda)$) and parasitic heating ($I_{Para.}(\lambda)$) which consists of recombination, FCA and absorption of metallization. These values can be calculated by the following equations.

$$I_{Therma.}(\lambda) = I_{ABS}(\lambda) \times IQE(\lambda) \times \frac{(S_g(\lambda) - E_g)}{S_g(\lambda)} \quad \text{Eq. 51}$$

$$I_{Elect.}(\lambda) = I_{ABS}(\lambda) \times IQE(\lambda) \times \frac{E_{g,MPP}}{S_g(\lambda)} \quad \text{Eq. 52}$$

$$I_{Rec.,Entr.,Resis.}(\lambda) = I_{ABS}(\lambda) \times IQE(\lambda) \times \frac{(E_g - E_{g,MPP})}{S_g(\lambda)} \quad \text{Eq. 53}$$

$$I_{Para.}(\lambda) = I_{ABS}(\lambda) - I_{Elect.}(\lambda) - I_{Therma.}(\lambda) - I_{Rec.,Enth.,Resis.}(\lambda) \quad \text{Eq. 54}$$

where E_g is the band gap energy of silicon which is 1.12 eV, $E_{g,fermi}$ is the energy difference between quasi fermi levels which is around 0.55 eV [53], $S_g(\lambda)$ is the energy of the solar spectrum in eV. Due to the recombination, entropy and resistive losses, the energy difference between quasi fermi levels ($E_{g,fermi}$) is lower than band gap of the silicon (E_g) [53]. Figure 37 shows the spectrum of AM1.5G, electrical output, thermalization, entropy, resistive losses, recombination, reflection, transmission and parasitic heating of the Al-BSF cell. In this

calculation, electrical outputs of the cells are derived in maximum power point (MPP) condition which is around 20% of the AM1.5G.

Figure 37 shows thermalization, entropy, recombination and resistive losses of the cell together (green). Thermalization loss is more dominant than recombination, entropy and resistive losses. Hence, thermalization significantly affects the shape of the green plot. Heating by thermalization is highly effective at short wavelengths due to the energy of the photon is higher than the bandgap energy of the silicon. Thermalization loss decreases above wavelength 450 nm because energy of the photon also decreases with increasing wavelength. Above 1100 nm main heating mechanism of the cell is parasitic heating (purple) which consists of recombination, FCA and parasitic absorption of metallization of the cell. Also, above 1100 nm reflection and transmission (only for bifacial cells) are other significant mechanisms that incoming light can turn into. Hence, high reflection and transmission (only for bifacial cells) are needed for wavelength above 1100 nm in order to keep the parasitic heating of the cell minimum. For wavelength above 1100 nm, 80% and 65.5% of the total sunlight leads to parasitic heating in monofacial and bifacial cells, respectively. The difference between the monofacial and bifacial cells is due to the transmission of the bifacial cell.

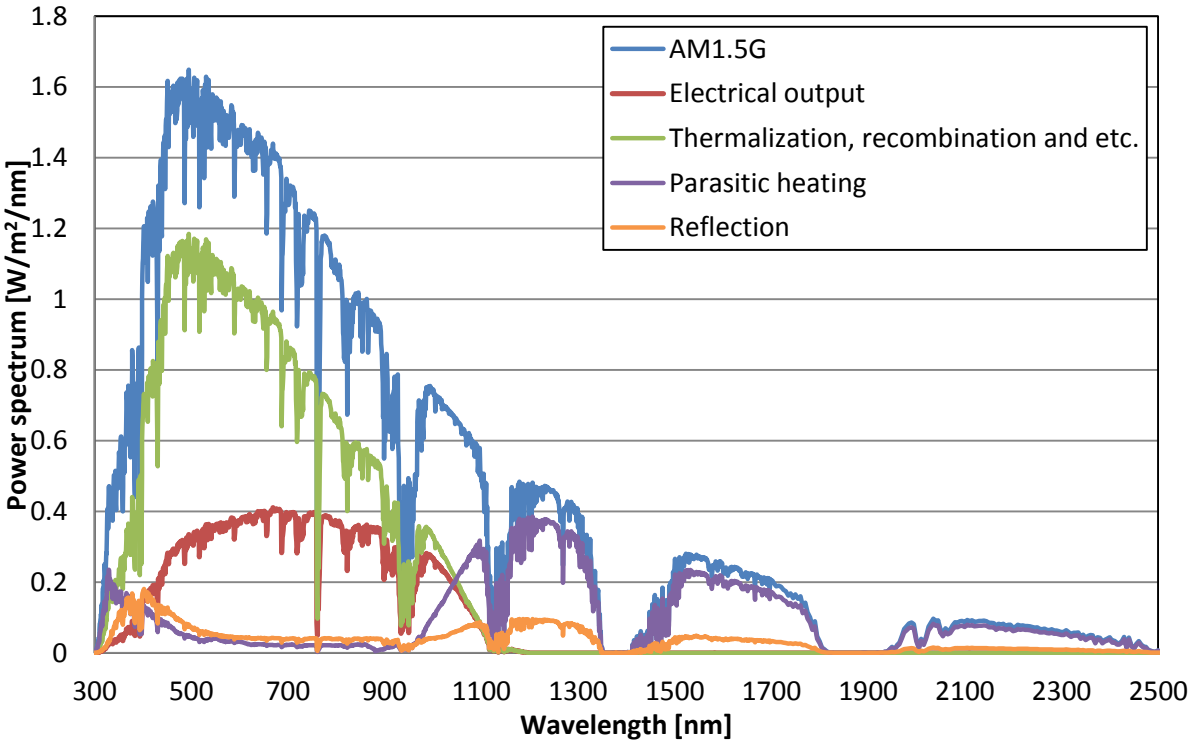

Figure 37: Spectrum of AM1.5g and electrical output, thermalization. Reflection and parasitic heating of the Al-BSF cell.

Figure 38 shows the spectrum of parasitic heating of the cells when they are illuminated from front side. As expected from the previous chapter, the Al-BSF solar cell (dark blue) has the highest parasitic heating at near IR region because of the existence of full area aluminum BSF and back contact. The unabsorbed IR light through the cell is parasitically absorbed by aluminum BSF and back contact and generates parasitic heating. The parasitic heating spectra of the bifacial cells are roughly comparable at wavelengths below 1000 nm due to the similar reflection, transmission and IQE responses. The Al-BSF cell has higher

parasitic heating compared to other cells at short wavelengths due to the low IQE response at UV region which might be due to the poorer front surface passivation. (Figure 38). The jasmine cell has the lowest parasitic heating due to the high reflective rear at near IR region (Figure 36 & 38).

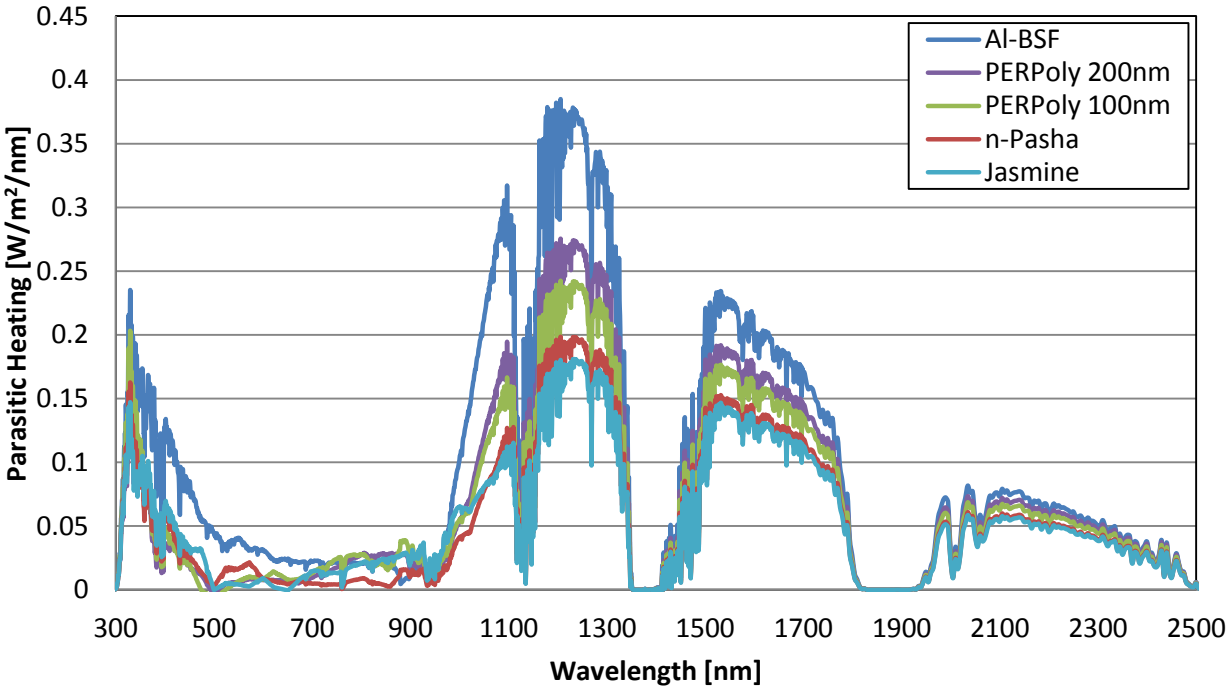

Figure 38: Spectrum of the parasitic heating of different cell types.

Table 5 shows the total heating and contribution of the parasitic heating to the total heating of the cells. Around 65%-70% of the total AM1.5g becomes source of heat for solar cells. The Al-BSF has the highest total parasitic heating and highest parasitic heating fraction (26.7%) to total heating. Total parasitic heating of the Al-BSF cell is around 86% higher than the total parasitic heating of the n-Pasha cell, so the overall total heating of the Al-BSF is around 9.5% higher than the total heating of the n-Pasha cell. The n-Pasha cell has lower total and parasitic heating than the jasmine cell because of the difference between their parasitic heating spectrums at short wavelengths (Figure 38).

Table 5: Average total heating, total parasitic heating and fraction of parasitic heating of the different cell types with a standard deviation.

	Total heating [W/m^2]	**Total parasitic heating [W/m^2]**	**Fraction of parasitic heating on total heating [%]**
Al-BSF	706.7±3.2	188.8±2.8	26.7
n-Pasha	645±3.8	101.8±1.7	15.8
PERPoly 100nm	660.7±1.4	122.3±1.6	18.5
PERPoly 200nm	666.2±2.6	126.9±2.7	19
Jasmine	643±2.8	101.7±2.6	15.8

5.1.2. Absorption Model for the PERPoly Cells

Absorption of the both PERPoly cells were modeled for band to band absorption and free carrier absorption. Figure 39 and 40 show the total absorption (band to band absorption of silicon and free carrier absorption) by using the model and measured absorption which is derived from the measured spectral reflection and transmission of the PERPoly 100nm and PERPoly 200nm cells, respectively. As it can be seen from Figure 39 and 40, modeled total absorption perfectly follows the measured total absorption level until 990 nm where the free carrier absorption starts to be more dominant. Between 990 and 1100 nm, total absorption of the both cells is underestimated (Figure 39 and 40). Also, above 1100 nm, total absorption is predicted higher than measured total absorption (Figure 39 and 40). In the model, light is assumed to be perpendicular to all layers of the semiconductor material. This might be a reason of the deviations.

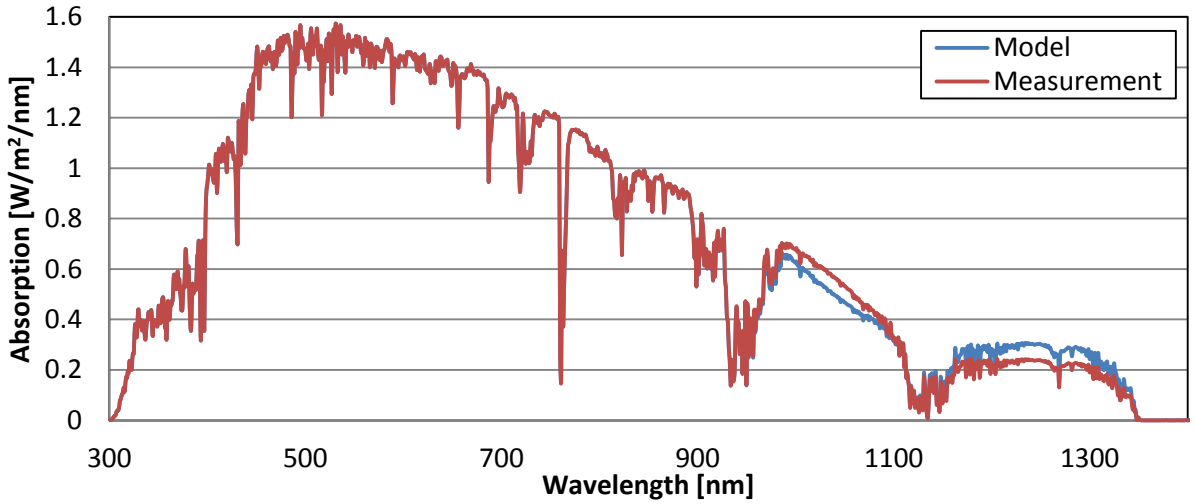

Figure 39: Modeled total absorption (band to band absorption of silicon and free carrier absorption) and measured absorption by using the measured spectral reflection and transmission for PERPoly 100nm cell.

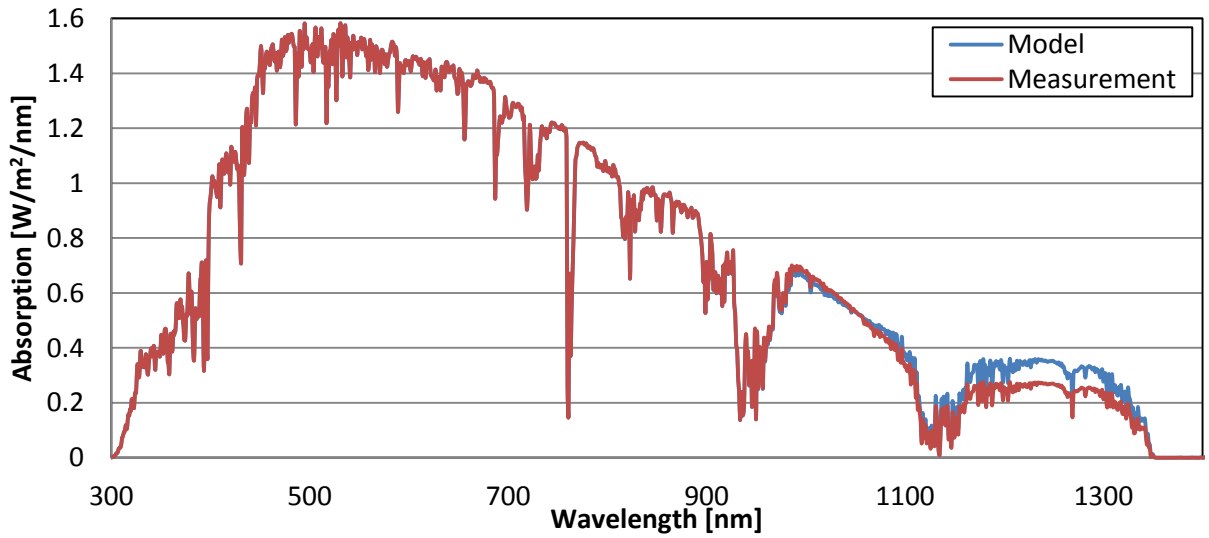

Figure 40: Modeled total absorption (band to band absorption of silicon and free carrier absorption) and measured absorption by using the measured spectral reflection and transmission for PERPoly 200nm cell.

Figure 41(a) and 41(b) show the distribution plot for the different absorption mechanisms, reflection and transmission of the PERPoly 100nm and PERPoly 200nm cells, respectively. Both cells have comparable band to band silicon absorption which is mainly by the emitter and base. As expected, free carrier absorption fraction of the PERPoly 200nm cell is higher than free carrier absorption fraction of the PERPoly 100nm cell due to the thicker polysilicon layer. Result of this PERPoly 100nm cell has higher reflection and transmission fractions than PERPoly 100nm cell.

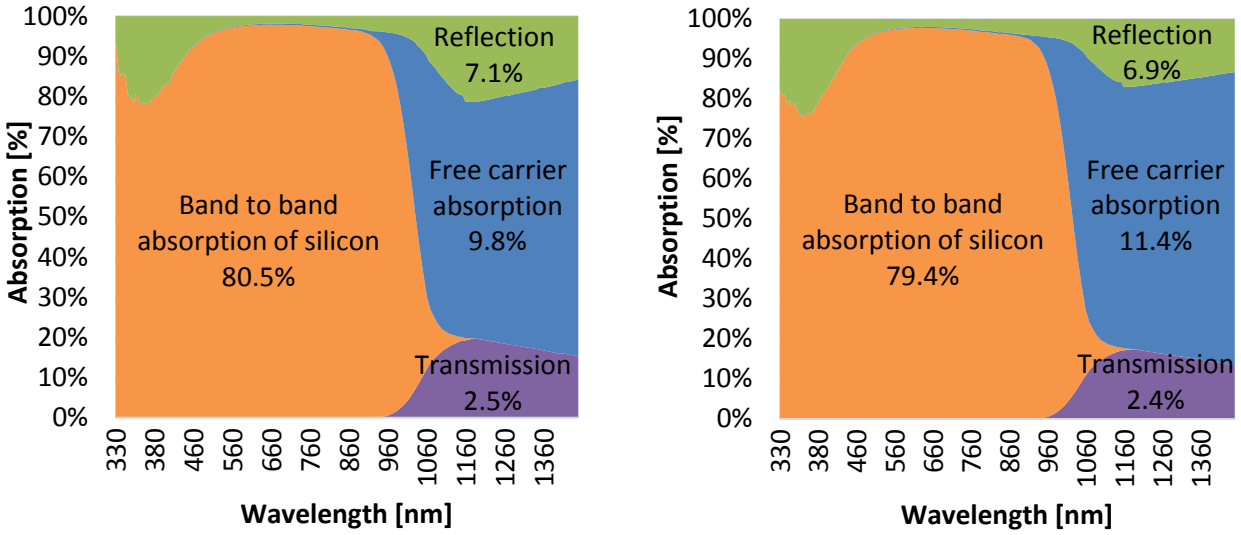

Figure 41: Distribution plot for band to band absorption, free carrier absorption, reflection and transmission of **(a)**PERPoly 100nm and **(b)**PERPoly 200nm at 330-1400nm wavelengths.

5.2. Analysis of the Single Cell Modules

The IV results of the glass-glass modules, which are built by using the cells that are mentioned in the previous chapter, are shown in Table 6. The modules with PERPoly cells have the highest V_{oc} and I_{sc} as expected from the cell IV measurements. Also, Al-BSF module has the lowest V_{oc} and I_{sc}.

Table 6: IV characteristics of glass-glass modules with different cell types.

g-g module	I_{sc} [A]	V_{oc} [V]	FF [%]	Efficiency [%]	Bifaciality factor [%]
Al-BSF	8.50	0.622	74.4	15.9	-
n-Pasha	8.83	0.658	74.8	18.2	94.1
PERPoly 100nm	8.92	0.676	74.2	18.7	89.1
PERPoly 200nm	8.86	0.675	73.7	18.4	83.3
Jasmine	8.81	0.630	71.8	16.5	69.8

The I_{sc}, fill factor (FF) and aperture efficiency values, which is the efficiency of aperture area, decreased from cell to module for all modules but bifaciality factors of the modules with bifacial cell increased. In the solar cells, light goes from air to cell. However, for the encapsulated solar cells, light goes from air to glass/EVA and from glass/EVA to cell. The optical coupling is different from air to cell than from air to glass/EVA to cell [54] [55]. The glass and EVA layers decrease the amount of light that illuminates the solar cell which

has a decreasing effect (optical loss) on I_{sc} from cell to module on both sides. Additionally, while making solar module from solar cell, tabs are soldered as busbar and cross connector. Light that is incident on the busbar, partially scatters back. This scattered light might scatter back to the solar cell at module interfaces, e.g. the boundary of EVA and glass [55]. Hence, the amount of light that the module effectively gets is higher than the amount of light that the cell gets which is an increasing effect (optical gain) on the I_{sc} from cell to module on both sides. Table 7 shows the cell to module change for I_{sc}, efficiency and bifaciality factor for the glass-glass modules. Apart from the I_{sc} of rear side of the jasmine, I_{sc} from cell to module decreases for both sides of the modules which reveals optical loss from cell to module is more significant than optical gain from cell to module. The reason for the I_{sc} increase from cell to module on rear side of the jasmine is that rear side of the jasmine cell is high reflective and not textured, so glass/EVA interface act as an anti-reflective coating and decreases the reflection of the rear side which increases the light that illuminates the cell. In addition, the solar cells are optically optimized for front side efficiency, e.g. the properties of the SiN_x coating on the front is also optimized for anti-reflection, whereas SiNx on the rear side is mostly optimized for the combined effect of rear side passivation and contact formation [56]. Therefore, the optical gain at the rear side might be higher than the front side. This can cause lower decreasing value of I_{sc} for the rear side compared to the front for n-Pasha and PERPoly modules (Table 7) which results in better bifaciality actor.

As mentioned before tabs are soldered as busbar and cross connector so they have additional resistive losses [18]. Hence, FF from cell to module decreases around 4.9% ±0.17 and 4.1% ±0.12 for front and rear of all modules, respectively. The decrease in both I_{sc} and FF lead to decrease in efficiency of the modules. In addition, since the decrease in I_{sc} and FF on the front is higher than the decrease in I_{sc} and FF on the rear, bifaciality factor increases for all bifacial modules (Table 7).

Table 7: Cell to Module change on I_{sc}, efficiency and bifaciality factor for the glass-glass module with different cell types.

	I_{sc} [%]		**Efficiency [%]**		**Bifaciality factor [%]**
	Front	**Rear**	**Front**	**Rear**	
Al-BSF	-5.1	-	-11.4	-	-
n-Pasha	-4.9	-3.3	-10.9	-8.3	4.3
PERPoly 100nm	-4.9	-3.9	-10.7	-9.0	2.3
PERPoly 200nm	-5.0	-4.2	-10.8	-9.3	2.1
Jasmine	-5.6	15.2	-12.7	9.9	20.0

Light management of the modules with white and black back sheets are different than the light management of the glass-glass modules as mentioned in chapter 2.4.1. The I_{sc} of the modules are affected by the back sheet type which is either reflective or absorbing. Figure 42 shows the I_{sc} and P_{mpp} of glass-glass modules with different cell types.

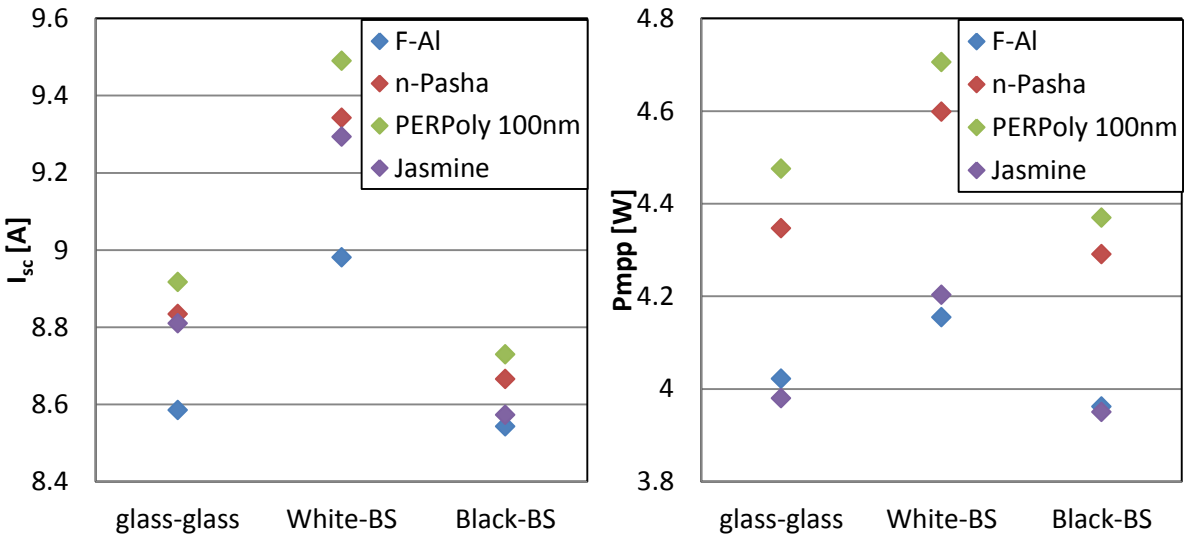

Figure 42: I_{sc} and P_{mpp} of different module types with different cell types (n-Pasha).

Since I_{sc} is directly related with the incident illumination on the cell, Figure 42 shows the outcome of the different light management mechanisms of the different module types, especially for modules with bifacial cells. The transmitted light through the cell can hit the back sheet and depending on the type of the back sheet it is either reflected or absorbed. For modules with white back sheet, significant amount of reflected light from the back sheet increases the I_{sc} (Figure 42). There are three types of optical gains from glass-glass module to white back sheet module. The first optical gain mechanism is unabsorbed light through the bifacial solar cell can be reflected back into the active area of the rear of the cell. The second and third mechanisms are the incident light on the non-solar cell area of the module (edge of the module) can be scattered to active area of the rear side of the cell [57] or can be reflected back to glass/air interface and reflect back into the front surface of the cell [57]. For modules with bifacial cells, all mechanisms are valid but for modules with monofacial cell, only gain from front glass which scattered from non-solar cell area of the module mechanism is valid. Black back sheet is non-transparent and has around 95% absorption rate at all wavelengths as mentioned in chapter 2.4.1. Figure 42 shows that modules with black back sheet have lower I_{sc} than glass-glass module. For the glass-glass modules, incident light on the glass/air interface of the rear side of the module might reflect back into the rear side of the cell or front glass of the module. This mechanism results in an optical gain for the glass-glass modules. The reason behind the lower I_{sc} of black back sheet modules than glass-glass modules might be lesser reflection from black back sheet (~5%) than glass/air interface. In addition, since the module type does not have a significant impact on the V_{oc} and FF of the modules, change in the I_{sc} directly affects the P_{mpp} of the modules (Figure 42).

Figure 43 shows the IQE of the glass-glass modules. Since all modules are glass-glass, same amount of the parasitic absorption by glass and encapsulant material is expected for all glass-glass modules from cell to module. The jasmine cell has higher IQE response than Al-BSF cell at UV region and similar IQE response as n-Pasha at IR region as mentioned in chapter 5.1. However, jasmine module has similar IQE response as Al-BSF module at UV region and lower IQE response than n-Pasha module at IR region. This indicates that jasmine module has higher cell to module (CTM) losses than other modules at UV and IR regions.

These unexpected decreases at both UV and IR regions might be due to the manufacturing damage on only jasmine modules, since other modules does not have this loss and all jasmine modules have same loss. Hence, manufacturing jasmine modules should be more investigated to understand the reason behind the decreases. Due to the decrease in IQE response of jasmine module, n-Pasha has the highest IQE red response (Figure 43).

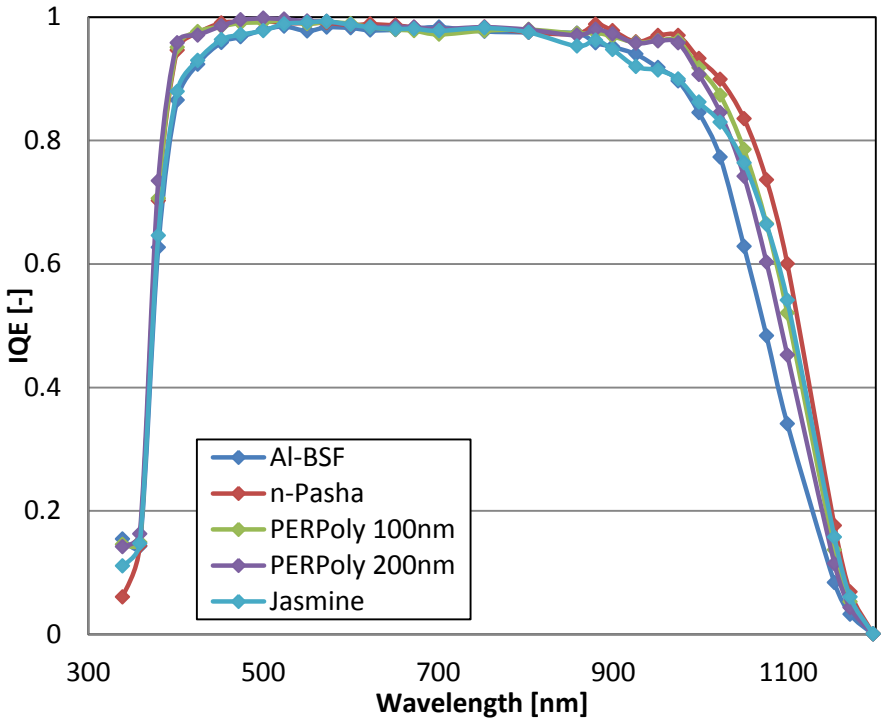

Figure 43: IQE of glass-glass modules with different cell types.

The reflection and transmission rates of the modules are changed from cell to module due to parasitic absorption of the module materials. The absorption of the module materials is elaborately explained in chapter 5.2.1 below. Figure 44 shows the reflection and 1-transmission rates of glass-glass modules. Still jasmine module has the highest reflection at near IR region. The n-Pasha and Al-BSF modules have similar reflection behaviors but since Al-BSF module has no transmission, higher absorption is measured from Al-BSF module (~81.2%) compared to other modules at near IR region. At around 1150 nm, similar absorption rates are expected from n-Pasha (~55.9%), PERPoly 100nm (~55.1%) and jasmine (~55.3%) modules and higher absorption is expected from PERPoly 200nm (~63.65%) module.

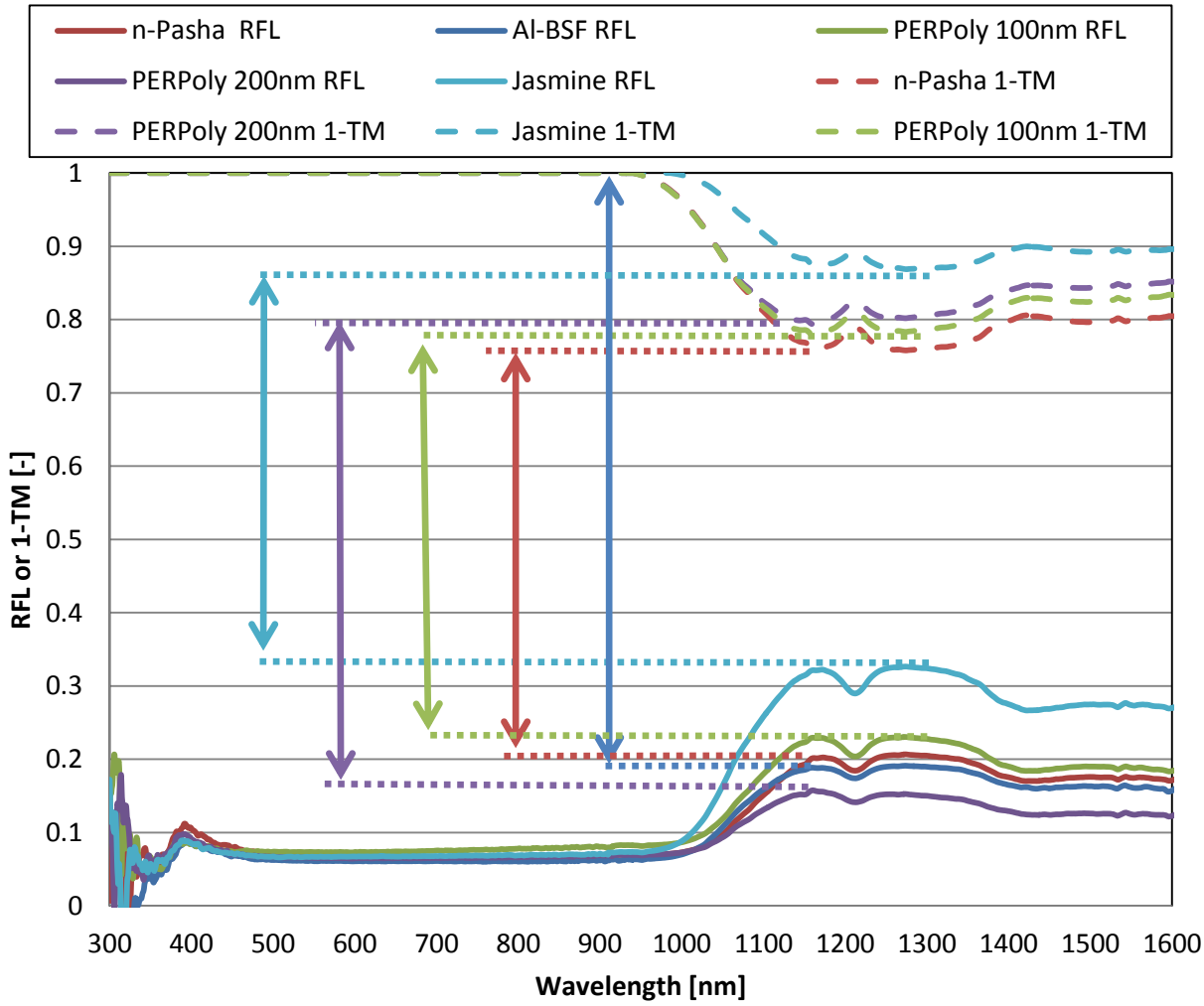

Figure 44: Reflection and 1-Transmission of the glass-glass modules with different cell types.

Different module types have different light management properties, which results in creating different spectral reflection and transmission values. Figure 45 shows the spectral reflection and 1-transmission of the three module types with bifacial cell (n-Pasha). Since monofacial cell (Al-BSF) cannot transmit light, module type has no effect on the reflection of the active area of the module. The module with white back sheet has the highest reflection and the glass-glass module has slightly higher reflection than the module with black back sheet (Figure 45). Since the glass-glass module has highest transmission rate by far, it has also the lowest absorption rate (~55.9%) at IR region. The module with white back sheet (~68.6%) has lower absorption rate than the module with black back sheet (~81.3%) because of the high reflection rate at near IR region. As a result, highest absorption is expected from black back sheet modules due to the high absorbing rate of the black back sheet which results in highest heat input. Also, lowest absorption is expected from glass-glass modules due to the high transmission rate of the glass + EVA which results in lowest heat input.

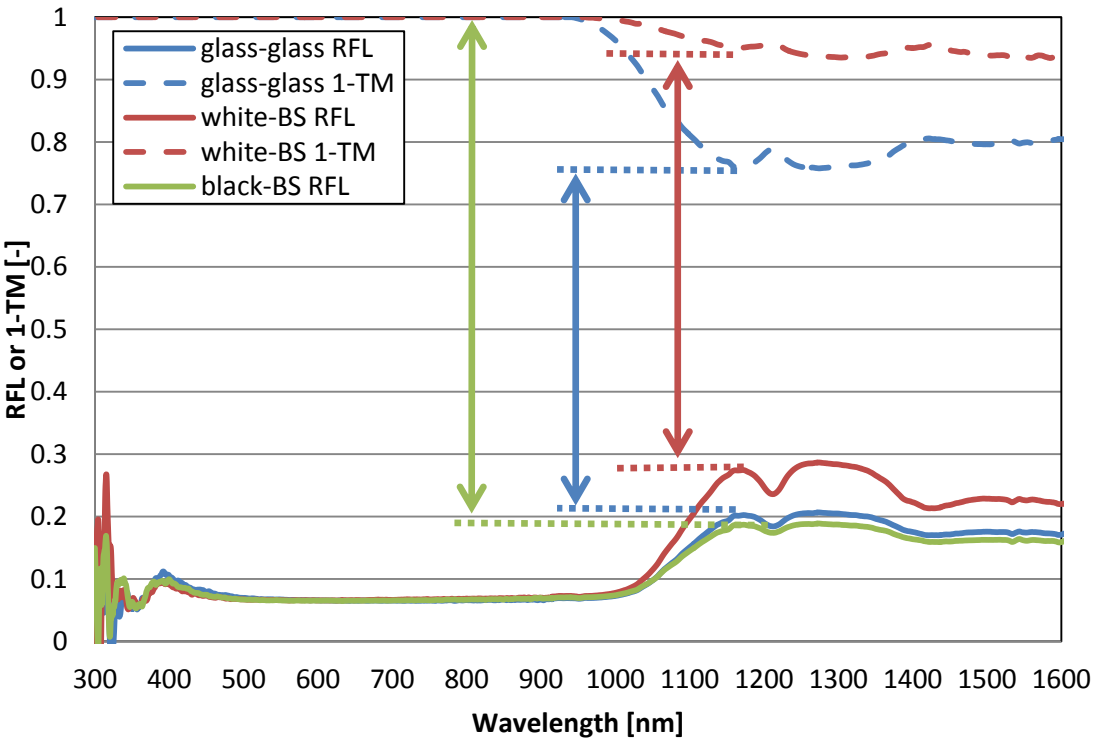

Figure 45: Reflection and 1-Transmission of the different modules types with bifacial cell.

5.2.1. Module Material Absorption

Power losses occur from cell to module due to optical, resistive and mismatch components. To evaluate the optical losses/gains, IQE, spectral reflection and spectral transmission of the different modules are compared. Optical losses occur from cell to module due to additional reflectance and parasitic absorption of various layers (glass, EVA and back sheet) [58] [59] [60]. The optical loss mechanisms of the modules are shown in Figure 46. Besides the optical losses, optical gains from cell to module occur because of the incremental increase in the refractive index per layer (reduced reflection) [61] [62] and total reflection at the glass-air interface which reflects the light back into the active area of the cell (reduced reflection) [57].

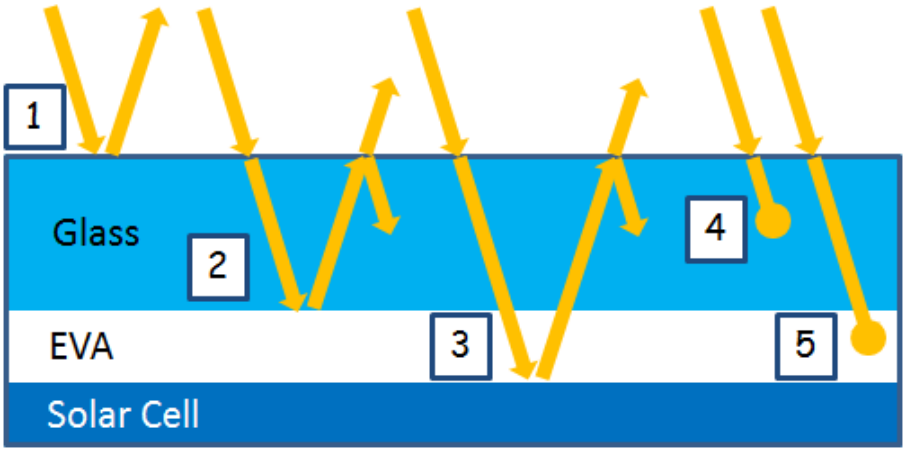

Figure 46: Various optical losses of a solar module (active area) (transmission for bifacial modules is not included). (1=reflection of air/glass interface, 2 = reflection of glass/EVA interface, 3 = reflection of EVA/Cell interface, 4 = absorption of glass, 5 = absorption of EVA.)

Figure 47 shows the absorption rate of the glass/EVA/glass stack. At short wavelengths, both glass and EVA have high absorption coefficient [58]. Especially, the EVA blocks most of the UV light which is below 400 nm [58] [63]. In addition, at around 1200 nm, there is sudden drop in the reflection and transmission of the modules (Figure 44 & 45). The reason for this drop is the EVA absorption peaks between 1100 nm and 1300 nm which is possibly because of the absorptions of C-H due to vibrational overtones [58] (Figure 47).

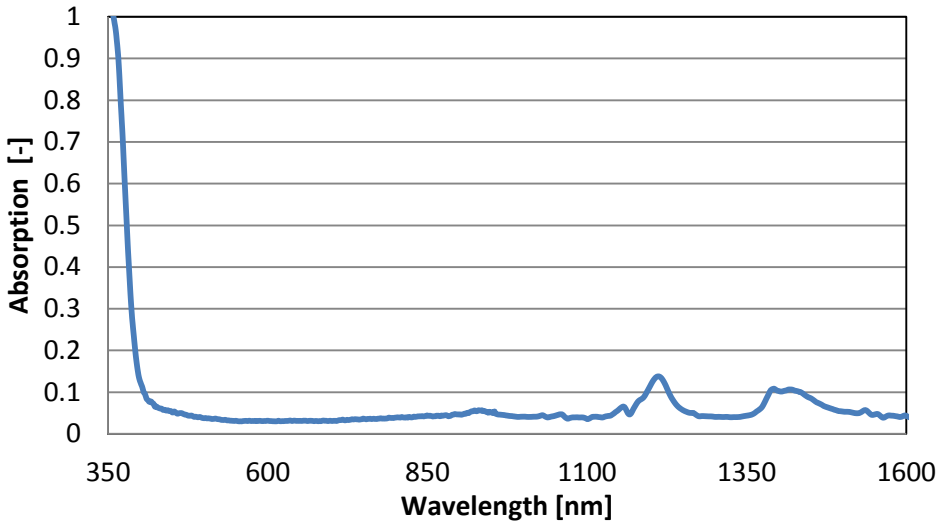

Figure 47: Absorption rate of the glass/EVA/glass stack.

The effect of the parasitic absorption by module materials can be seen in Figure 48(a) and 48(b) which shows the IQE response, spectral reflection and spectral transmission measurements, respectively. The CTM decrease of the IQE and the reflection at UV region take place due to the high absorption coefficients of the glass and EVA at UV region (Figure 48(a) & 48(b)) [63]. In addition, at IR region, there is decrease in the reflection and transmission from cell to module due to the parasitic absorption of the module materials. At around 1200 nm, there is drop in the reflection and transmission due to peaks in the absorption of the EVA at 1100-1300 nm as explained in the previous paragraph (Figure 48(b)).

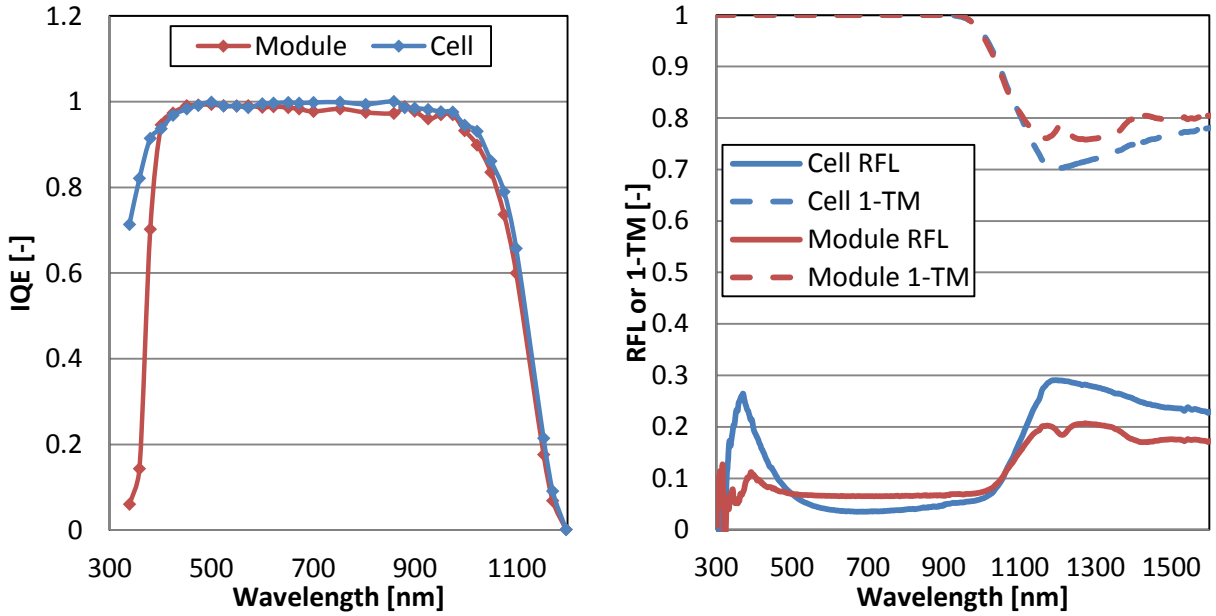

Figure 48:(a) CTM IQE of glass-glass module with bifacial cell and **(b)** CTM reflection and 1-transmission of glass-glass module with bifacial cell

The effect of CTM changes on the IQE response, reflection and transmission as seen on Figure 48(a) and 48(b) directly leads to increase in parasitic heating from cell to module at UV and IR region. Figure 49 shows the CTM parasitic heating of glass-glass, white back sheet and black back sheet modules. At UV region, modules have higher parasitic absorption than the cell due to the absorption of glass and EVA. Since all module types have the same front side materials, they have similar CTM parasitic heating increase at UV region. At IR region, parasitic heating increases from cell to module due to the module materials at the rear (glass + EVA, white and black back sheet). Above 1000 nm, since black back sheet has the highest absorption rate compared to other rear encapsulant materials (white back sheet and glass + EVA), black back sheet module has the highest parasitic heating increase from cell to module compared to other module types.

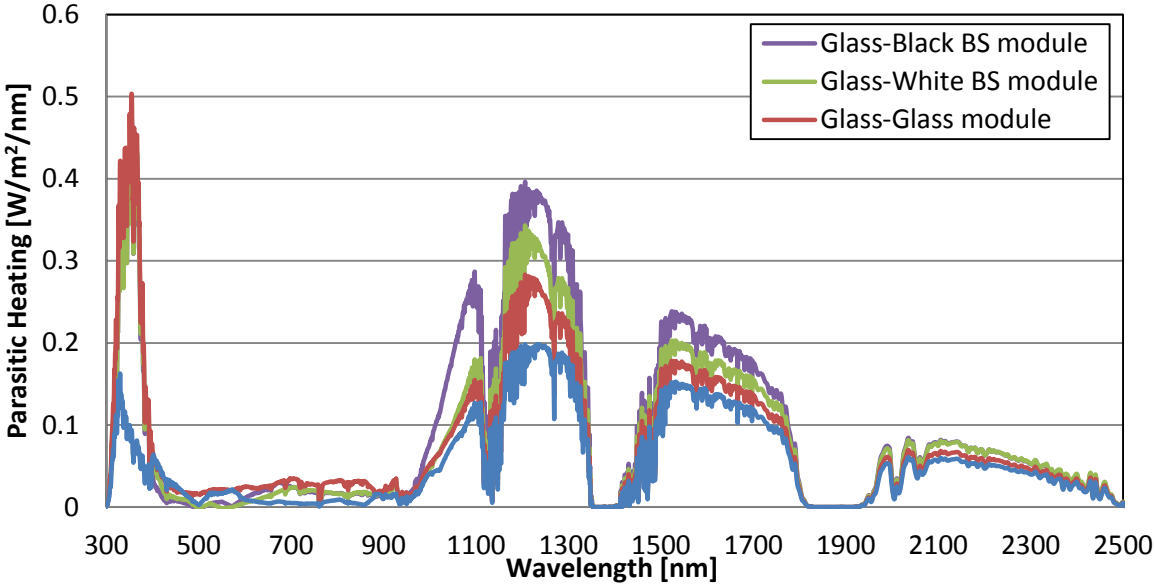

Figure 49: Spectrum of the parasitic heating of bifacial cell and different module types with bifacial cell.

5.2.2. Total and Parasitic Heat Inputs

Spectral heating of the modules is calculated with spectral reflection and transmission of the active area of the modules by using the method that explained in chapter 5.1. Figure 50 shows the spectrum of the parasitic heating of glass-glass modules. At short wavelengths the Al-BSF and jasmine modules both have higher parasitic heating due to lower IQE response than other modules. Main difference between the parasitic heating values of all the glass-glass modules are visible at near IR region. Parasitic heating spectrum of the modules are comparable with parasitic heating spectrum of the cells. The Al-BSF module has highest parasitic heating due to the absorption of the full area aluminum back contact. The only exception is that from the cell derivations, jasmine cell has the lowest parasitic heating at above 1100 nm but from glass-glass module calculations, both n-Pasha and jasmine modules have the lowest parasitic heating response at above 1100 nm.

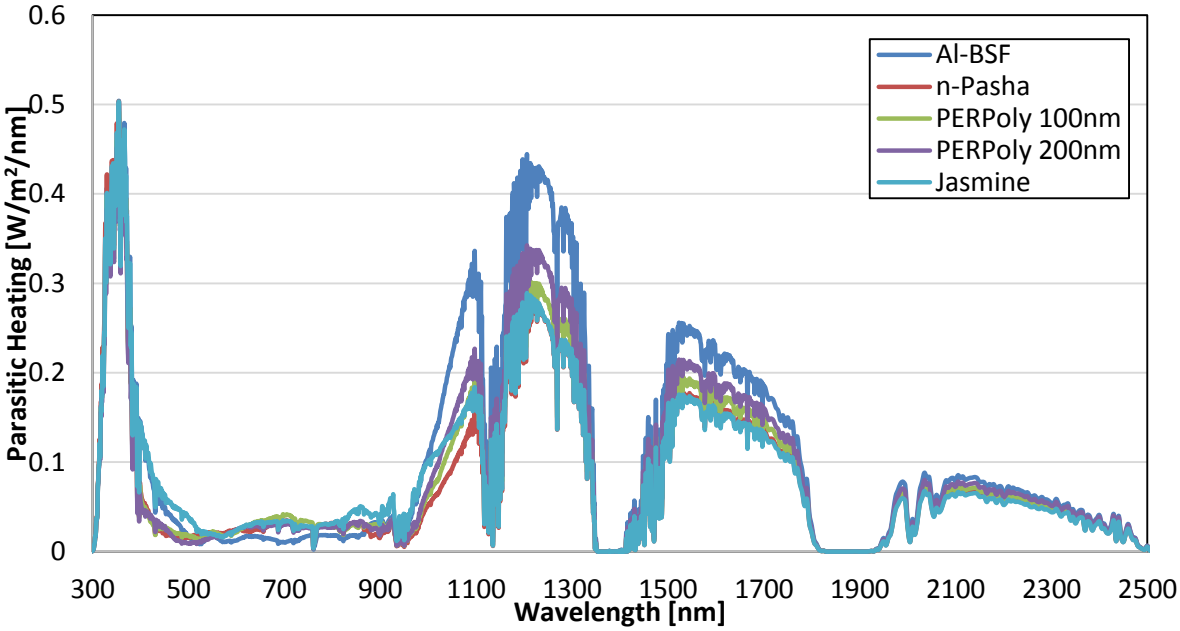

Figure 50: Parasitic heating spectrum of glass-glass modules with different cell technologies.

Figure 51 and 52 shows the spectral parasitic heating of different module types with monofacial (Al-BSF) and bifacial (n-Pasha) cells, respectively. The module type does not have any effect on the parasitic heating of the module with monofacial cell since light cannot be transmitted by the monofacial solar cell (either reflected or absorbed by aluminum back contact). On the other hand, light can pass through the bifacial cell so it can be either absorbed or reflected by the back sheet. Hence, back sheet affects the heating of the module depending on the absorption level of the back sheet. Since black back sheet has higher absorption rates than the white back sheet, parasitic heating of module with black back sheet is higher than parasitic heating of module with white back sheet at IR region (Figure 52).

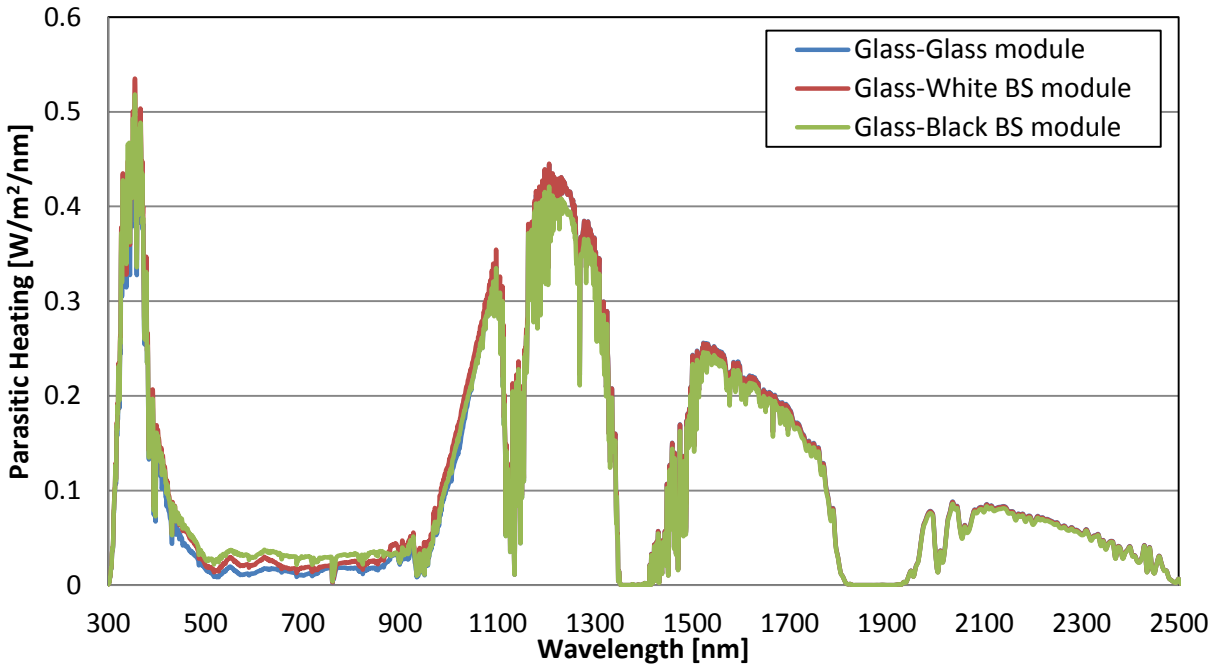

Figure 51: Parasitic heating spectrum of different module types with monofacial cell.

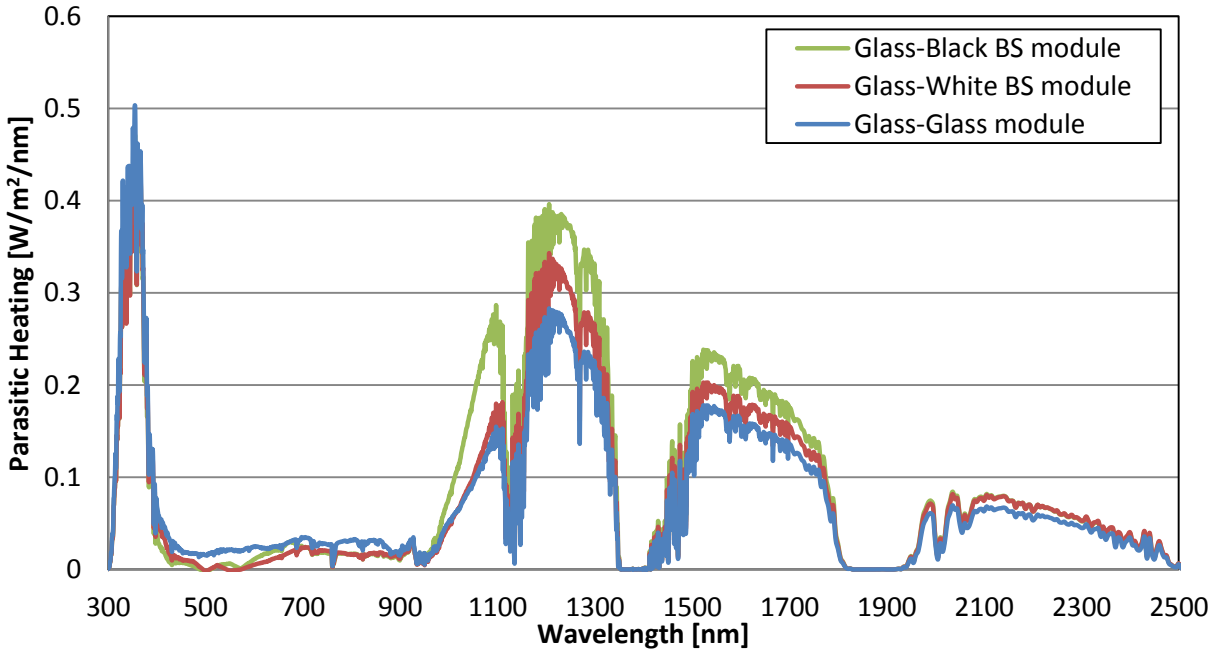

Figure 52: Parasitic heating spectrum of different module types with bifacial cell.

Figure 53 and 54 show the spectrum of the parasitic heating of the modules with white and black back sheet, respectively. Since Al-BSF cell cannot transmit light, module type does not have an effect on the parasitic heating of the module, as discussed in previous paragraph. However, module type has an effect on modules with bifacial cells. Regardless of the type of the back sheet, modules with any type of back sheet have higher parasitic heating than glass-glass modules. Hence, parasitic heating values of the white and black back sheet modules with bifacial cells approach the parasitic heating of Al-BSF module at near IR (Figure 53 and 54). Depending on the absorption of the back sheet, the difference in the parasitic heating

values of the modules change. For the white back sheet modules, Al-BSF module has the highest parasitic heating but the differences between Al-BSF module and other modules are smaller than the differences between Al-BSF glass-glass module and other glass-glass modules (Figure 50 and 54). For the black sheet which has high absorption rate, parasitic heating of the PERPoly 100nm module is close to the parasitic heating of Al-BSF module and n-Pasha has slightly lower parasitic heating response than them at near IR.

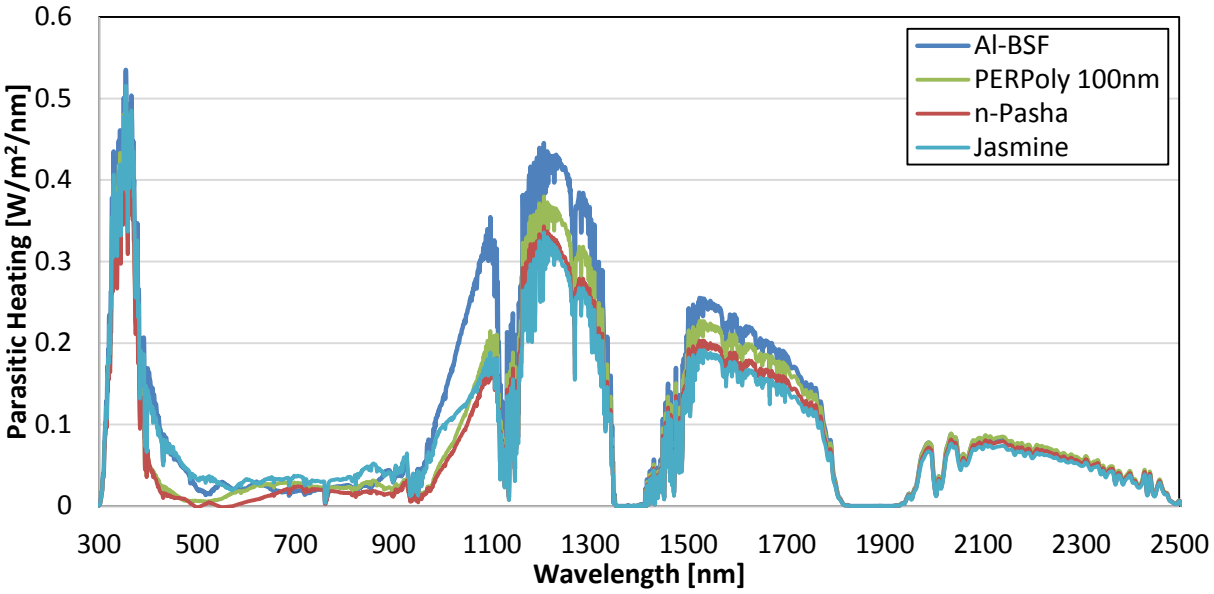

Figure 53: Parasitic heating spectrum of white back sheet module with different cell technologies.

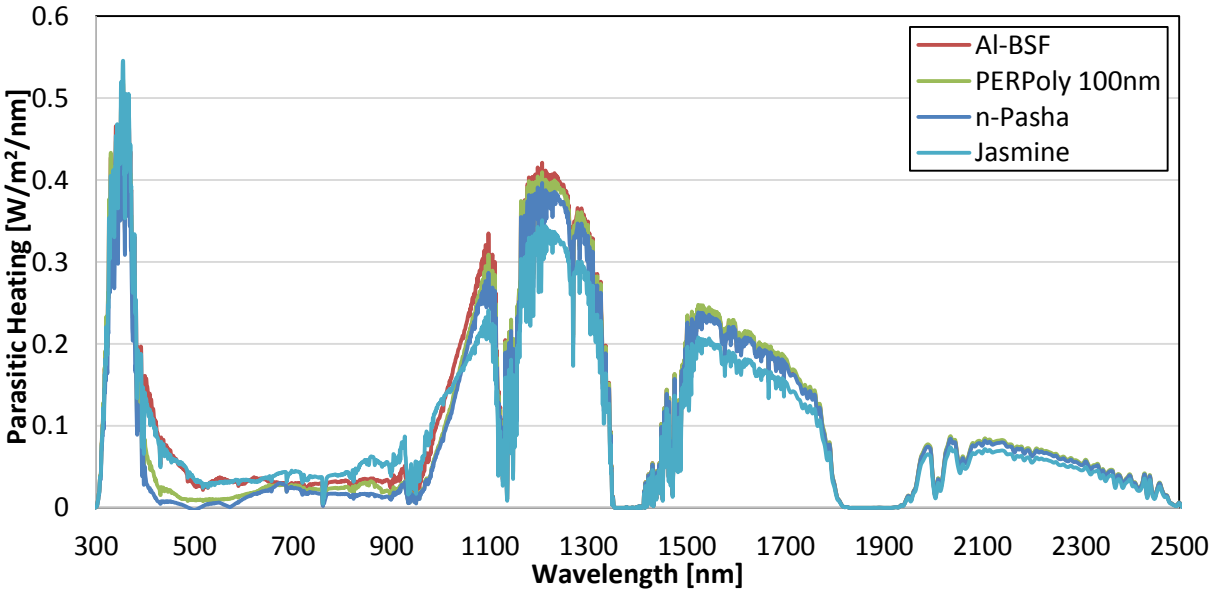

Figure 54: Parasitic heating spectrum of black back sheet module with different cell technologies.

In Figure 55, total parasitic heating values of different module and cell types under one sun illumination from front side can be seen. The Al-BSF module has the highest parasitic heating and n-Pasha module has the lowest parasitic heating in all module types. The glass-glass modules with bifacial cell has lower parasitic heating than the white back sheet modules with bifacial cell. Also, the white back sheet modules with bifacial cell has lower

parasitic heating than the black back sheet module with bifacial cell. The Al-BSF modules have similar parasitic heating values for all the module types but there are differences mainly due to variations in IQE response between 500 nm and 900 nm which is also visible in spectrum of parasitic heating (Figure 51). From the parasitic heating calculations of the cell measurements, parasitic heating is expected to be the lowest for jasmine modules. However, it has similar parasitic heating value as PERPoly 100nm for all module types. This unexpected change might be due to an error in manufacturing process of the jasmine modules, as mentioned before.

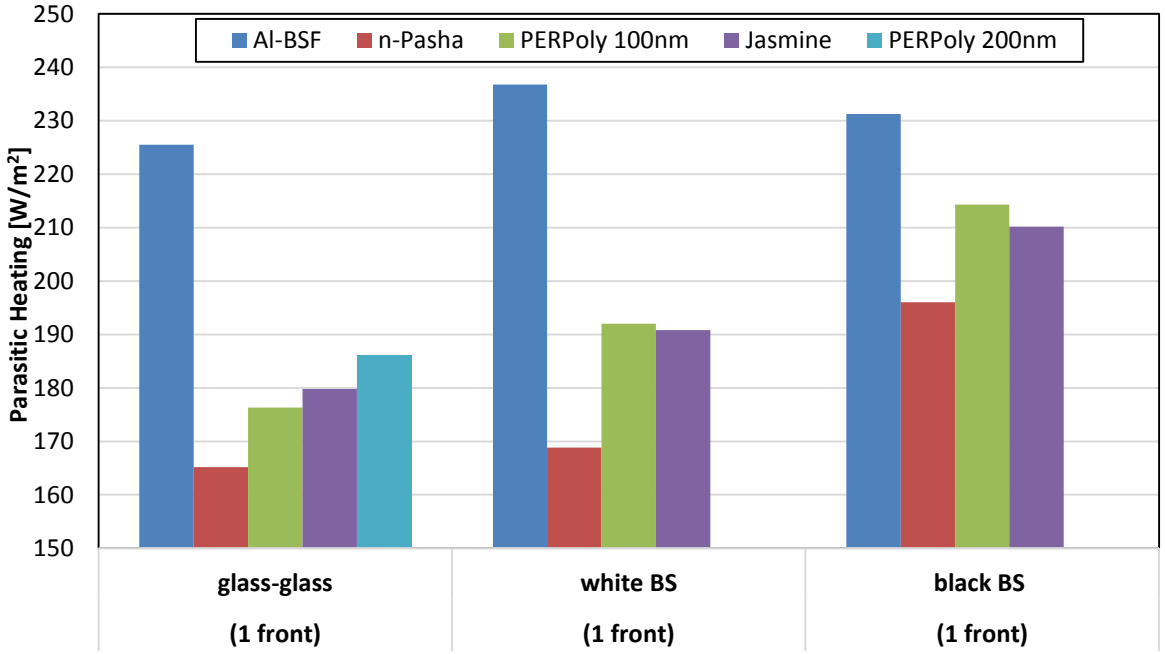

Figure 55: Total parasitic heating of different module types with different cell technologies.

When modules are placed free-standing, the illumination from back side of the modules becomes an important parameter on the heating of the module. Parasitic heating of all module types with (0.3 sun) and without rear contribution can be seen in Figure 56. Due to the full aluminum back side of the glass-glass Al-BSF module, rear illumination results in steep increase in parasitic heating of Al-BSF glass-glass module. In addition, different rear side technologies of the cells cause increase in difference between parasitic heating values of glass-glass modules with increasing rear contribution. However, for jasmine module the increase is very little because of the high reflective back side. Hence, when there is 0.3 sun rear contribution it has lower parasitic heating value than PERPoly 100nm (Figure 56). Since rear side of monofacial modules parasitically absorbs some amount of the incident light, parasitic heating also increases for monofacial modules with increasing rear contribution. The colors of the rear sides of both white and black back sheets are white and incident light on the rear of the back sheet is either reflected, transmitted (only for white back sheet) or absorbed. Hence, if there is rear contribution, parasitic heating of the black back sheet module increases due to the parasitic absorption by back sheet (Figure 56). For white back sheet modules, heating mechanism from rear is more complicated, since small portion of the incident light passes through the white back sheet. Transmitted light causes thermalization and parasitic heating (e.g. FCA and recombination) for modules with bifacial cells and only parasitic

heating (absorption by aluminum contact) for modules with monofacial cell. Hence, parasitic heating of the white back sheet module increases due to absorption by the back sheet, thermalization and parasitic absorption by the cell with increasing rear contribution.

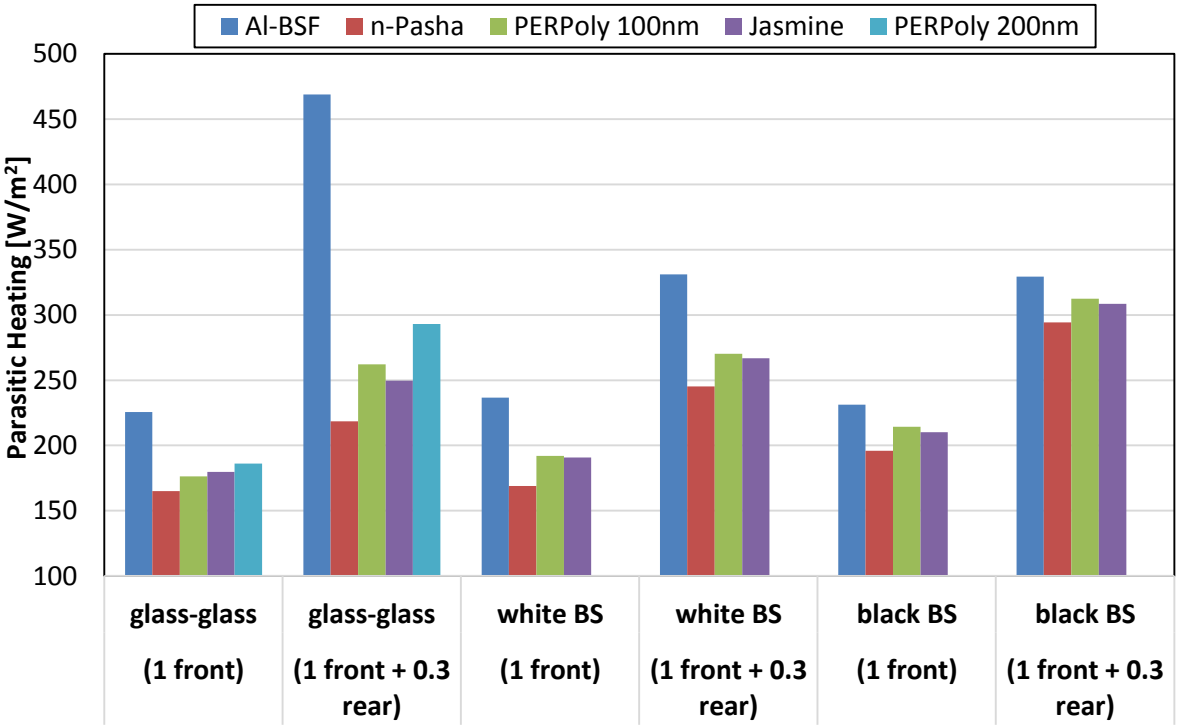

Figure 56: Total parasitic heating of different module types with different cell technologies with (0.3 sun at rear) and without (no sun at rear) rear contribution.

Other parameters that lead to increase in the total heat of a solar module are thermalization, entropy and resistive losses. However, since all the modules use c-Si as absorber, similar thermalization, entropy and resistive losses are expected. Therefore, the difference between total heating of the modules is mainly due to the parasitic heating. Figure 57 shows the total heating of the modules without and with (0.3 sun) rear contribution. Rear contribution increases the total heating of all module types; the amount depends on the module type. The total heat differences between the black back sheet modules with different cell types are minor and it is not affected by the rear contribution since black back sheet does not transmit light. The differences between the heating of the white back sheet modules with different cell types are also not affected significantly by the rear contribution since white back sheet only transmits little amount of light. On the other hand, total heating of the glass-glass modules highly depends on the rear contribution and especially total heat of the Al-BSF module increase steeply with rear contribution. Figure 57 tells the heat input under specified conditions for different module types with different cell technologies. By looking the total heating results of cell (Chapter 5.1) and module, the highest temperature is expected from Al-BSF modules and lower temperature is expected from n-Pasha and PERPoly 100nm modules for all module types. Additionally, when there is illumination from front side only, highest temperature is excepted from black back sheet modules as compared to other module types for modules with bifacial cell.

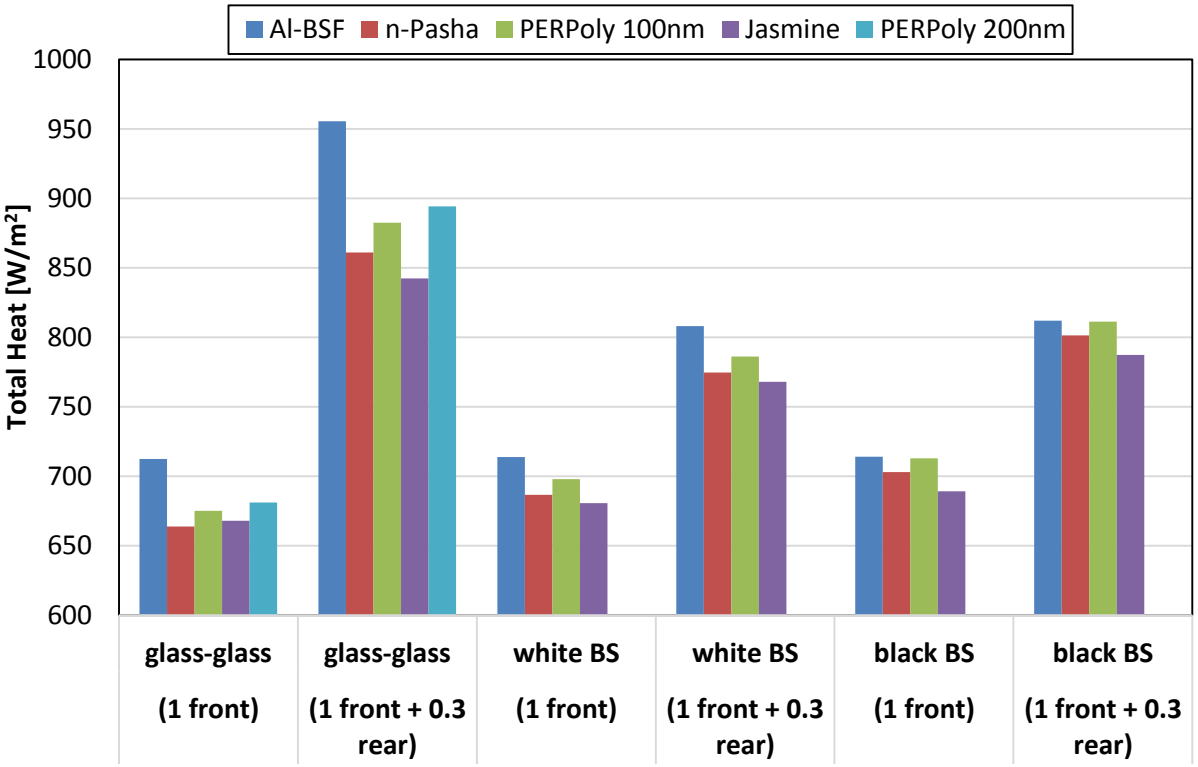

Figure 57: Total heating of different module types with different cell technologies with (0.3 sun at rear) and without (no sun at rear) rear contribution.

5.3. Outdoor Measurement Analysis

Weather conditions i.e. wind speed, ambient temperature, front irradiance and rear irradiance (only for free-standing module) have an impact on the module temperature. Irradiance is the main mechanism of heat input on the solar module which strongly affects the temperature of the module. Wind speed strongly affects the forced convection heat transfer (heat output). Figure 58(a) shows standardized Pareto chart for module temperature (glass-glass module with PERPoly 100nm cell) relative to ambient temperature. To determine the main effects (both linear and quadratic) a fitting procedure was applied using statistical data analysis software Statgraphics Centurion®. The standardized Pareto chart shows the significant effects on the relative module temperature. The p-value is statistical value that shows the statically significant relation between dependent and independent variables with specified confidence. In statistics, confidence limit is mostly 95%. Hence, p-value of the independent variable should be less than 0.05 in order to say that there is significant relation between dependent and independent values with 95% confidence. In this case, front irradiance, wind speed and square of front irradiance which have p-value close to zero, have significant relation with relative module temperature with 95% confidence. Front irradiance is dominant and has an increasing effect on the module temperature (Figure 58(a)). Also, wind speed causes higher forced convection which increases the heat transfer from the module. Hence, temperature of the module decreases with increasing wind speed (Figure 58(a)). Figure 58(b) shows the main effects plot of front irradiance and wind speed on the relative module temperature. Both curves only show the effect of only one independent variable on the relative module temperature. Relative module temperature has decremental increase with increasing front irradiance. The square of the front irradiance has significantly negative effect

on the relative temperature. Wind speed has linear and decreasing impact on the relative module temperature. Since the rear irradiance is around 11% of the front irradiance, rear irradiance does not have a significant effect (P value > 0.05) on the module temperature. In order to see the effect of rear irradiance which is expected to cause more difference between the module temperatures, ground should be painted white (high albedo factor).

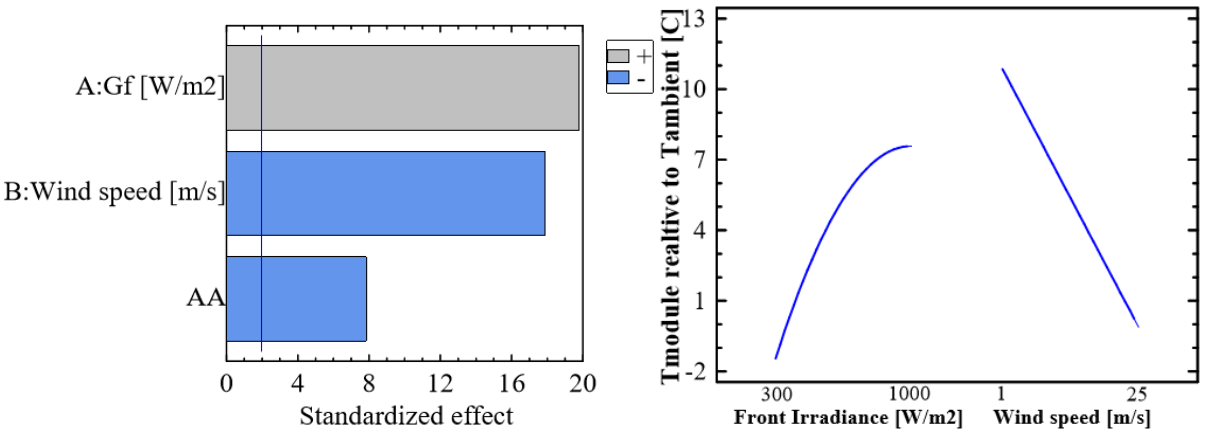

Figure 58: (a) Pareto chart and **(b)** main effect plot for front irradiance and wind speed.

Figure 59 shows the module temperature relative to ambient temperature as a function of front irradiance at low (wind speed=1 m/s) and high (wind speed=25 m/s) wind speeds. At low wind speed, forced convection has small impact on the cooling by convection. Therefore, more heat is kept inside the module and relative module temperature reaches around 13 K at 1000 W/m^2 front irradiance. On the other hand, at high wind speed, forced convection is significant and module temperature relative to ambient temperature barely reaches 3 K at 1000 W/m^2 front irradiance. The curve decreases at high irradiance because of fitting the data which is not realistic. This is out of scope of the project and more research should be done. Also, the temperature difference between low and high wind speed plots (the distance between the blue curves) increases with increasing front irradiance because when there is more heat input, effect of the forced convection by wind is more significant.

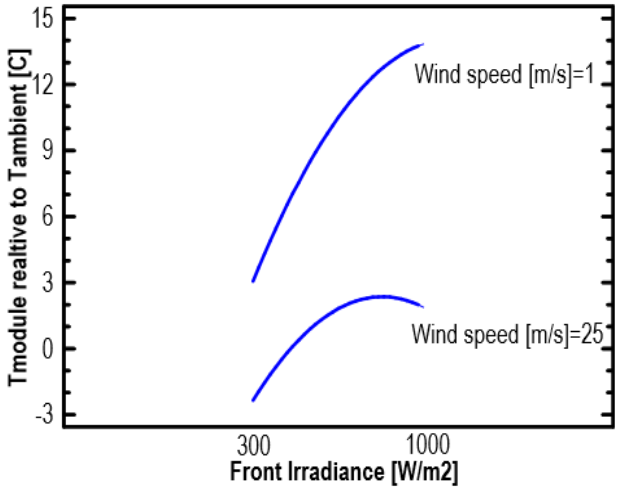

Figure 59: Module temperature relative to ambient temperature as a function of front irradiance at low (1 m/s) and high (25 m/s) wind speeds.

In the rest of this chapter, temperature of the modules which are calculated by using V_{oc} as explained in chapter 2.3, are compared. The ideality factor $n_{ide.}$ which is used to calculate the temperature from V_{oc}, varies as a function of the voltage. At low voltages (low irradiance), it increases to 2 and is not valid [35]. Therefore, calculated ideality factor from ECN developed program assumed to be constant between 700 and 1200 W/m^2 and only temperatures at this range is compared in this chapter. Rest of this chapter, mean of temperatures with two times of standard deviation (~%95 of the data), which are calculated by statistical data analysis software Statgraphics Centurion®, are given at 1000 W/m^2 front irradiance condition in order to see effect of cell and module type on the temperature statistically. More statistical research is out of scope of this work so mean values of the temperatures with two times of standard deviation are given.

5.3.1. Effect of Module Type on Modules with Monofacial and Bifacial Cells

Figure 60 shows the module temperature relative to ambient temperature for different module types with Al-BSF cell. From indoor heat input measurements, effect of module type on the temperature of the module with Al-BSF cell is expected to be insignificant when there is no rear irradiance (Figure 51). The back sheet which is the main difference between those module types has limited area (inactive area of the module/edge of the module) in order to make an impact on the temperature. However, even this small effect of the back sheet on the inactive area can be seen on the relative temperature of the module (Figure 60). The black back sheet module has 13.1±6.6 K higher temperature than ambient temperature while glass-glass and white back sheet modules have 12.5±5.0 K and 12.6±5.9 K higher temperature than ambient temperature at 1000 W/m^2. The reason for the differences in temperature between the different module types is the heating of back sheet at the inactive area of the module.

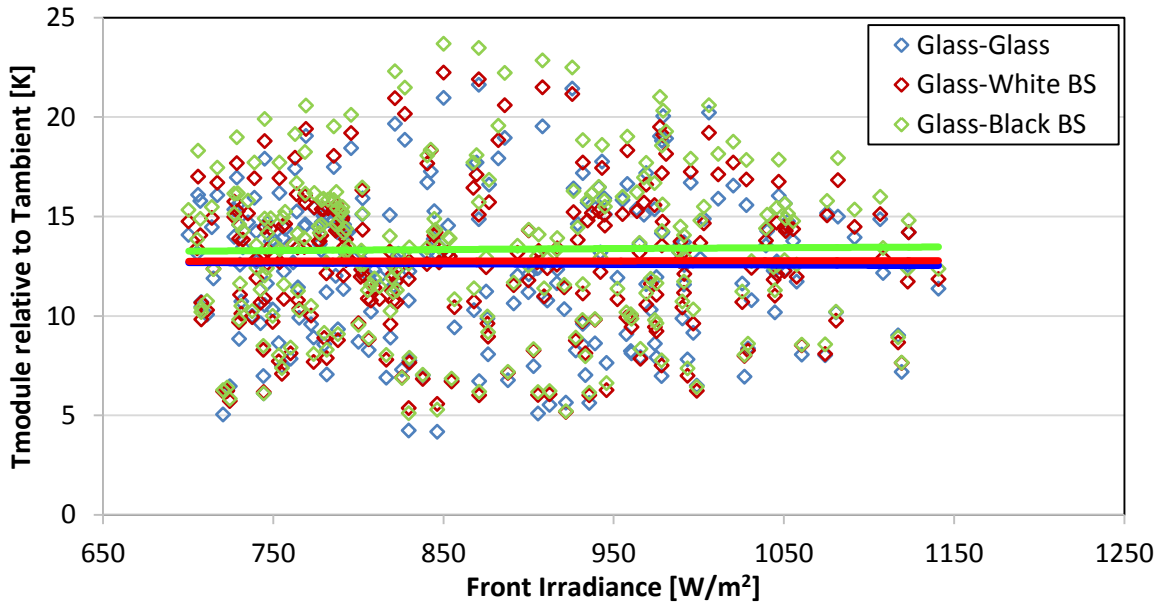

Figure 60: Module temperature relative to ambient temperature as a function of front irradiance for different module types with Al-BSF cell.

Module type has a significant effect on the modules with bifacial cell because unabsorbed IR light through the cell can be either absorbed by back sheet or pass through the

glass. Figure 61 shows the relative temperature of different module types with PERPoly 100nm cell. Modules with white and black back sheet have 12.1±6.3 K and 12.5±6.7 K higher temperature than ambient temperature at 1000 W/m^2. Since black back sheet (~95%) has higher absorption ratio compared to white back sheet (~20%), module with black back sheet has slightly higher temperature than module with white back sheet. Glass-glass module has lower temperature than monofacial modules which correlates with indoor measurements when the fraction of rear irradiance is low. Temperature of the monofacial modules relative to bifacial module can be seen in Figure 62. In the Netherlands, at low irradiances, fraction of the diffused light is high which results in high rear irradiance fraction for bifacial modules and at high irradiances, fraction of diffused light is low which results in low rear irradiance fraction for bifacial modules. Since at low irradiances fraction of the rear irradiance is high, temperature of the glass-glass module is close to monofacial modules due to thermalization and parasitic heating by active part of the module (Figure 62). The temperature difference between bifacial and monofacial modules increases with increasing irradiance because fraction of rear irradiance decreases with increasing front irradiance. From indoor heat input calculations, higher temperature is expected for glass-glass modules compared to monofacial modules when there is rear irradiance (Figure 57). One of reason of the unexpected temperature difference can be higher emissivity of glass compared to back sheet which results in higher radiative heat transfer for glass-glass module compared to monofacial modules. Also, heat transfer within the module level might be better for bifacial module compared to monofacial module. The white back sheet and black back sheet modules have 2.9±2.5 K and 3.4±3.0 K higher temperature than glass-glass module at 1000 W/m^2 (Figure 62).

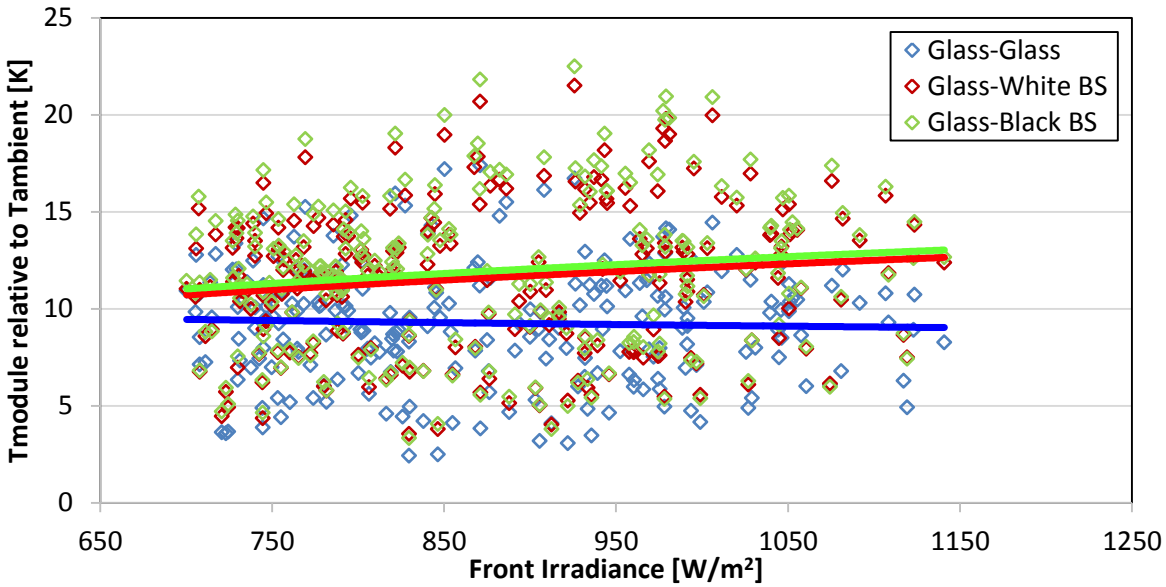

Figure 61: Module temperatures relative to ambient temperature as a function of front irradiance for different module types with PERPoly 100nm cell.

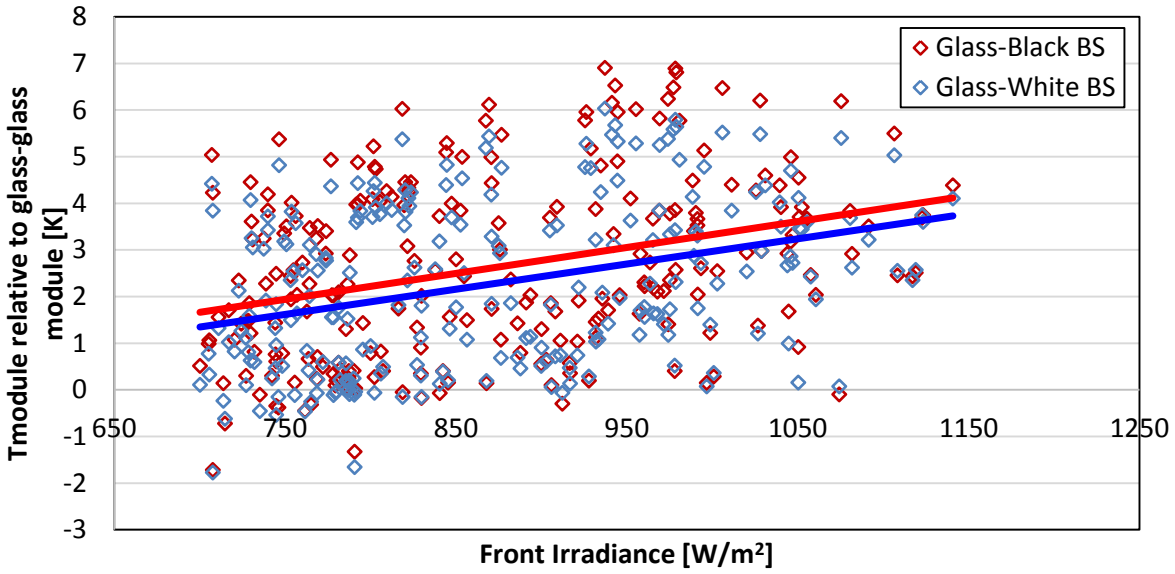

Figure 62: Temperature of monofacial modules relative to temperature of bifacial module as a function of front irradiance.

5.3.2. Effect of Cell Technology on Temperature of Glass-Glass Modules

Figure 63 shows the temperature of glass-glass modules with different cell technologies (Al-BSF, PERPoly100nm, PERPoly 200nm and Jasmine) relative to ambient temperature. In order to minimize the effect of place (i.e. wind speed) of the modules on the rack (i.e. wind speed), only modules which are close to each other are picked and described for the rest of this chapter. These modules are placed in the top row and third row of the rack (LA1, LA2, LA3 and LC2) (Figure 32). Depending on the wind speed and technology of the cell, modules have 5-20 K higher temperature than ambient temperature at 1000 W/m^2. In addition, Al-BSF module has the highest average temperature because of the existence of full aluminum contact which absorbs non-absorbed IR light through the cell. PERPoly 100nm module has the lowest module temperature between the modules as expected from indoor heat input measurements. The Al-BSF, jasmine, PERPoly 200nm and PERPoly 100nm modules have 12.6±5 K, 11.3±6.5 K, 10±6.5 K and 8.9±4.7 K higher temperature respectively than ambient temperature.

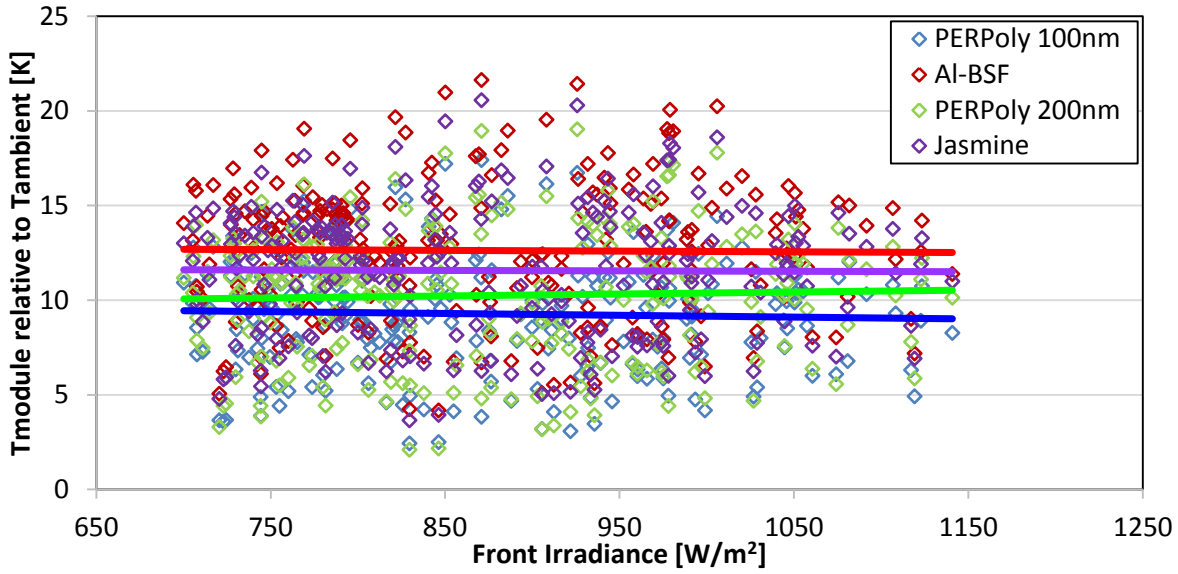

Figure 63: Temperature of glass-glass modules relative to ambient temperature as a function of front irradiance for different cell technologies.

In order to see the difference between the modules, Figure 64 shows the module temperature relative to PERPoly 100nm module which has the lowest temperature. Temperature of the Al-BSF module is 3.4±1.7 K higher than the temperature of the PERPoly 100nm module at 1000 W/m^2 because of the full aluminum back contact. If the ground had higher albedo factor, leading to higher rear irradiance fraction, this temperature difference would be higher because of the absorption of full aluminum contact. PERPoly 200nm module has slightly higher (1.3±2.0 K) temperature at 1000 W/m^2 compared to PERPoly 100nm due to higher free carrier absorption. The jasmine module has 2.4±1.5 K higher temperature than PERPoly 100nm module which is not expected from indoor measurements (Figure 57). As mentioned in previous chapter, in order to understand it, more research should be done on making modules by using jasmine cells.

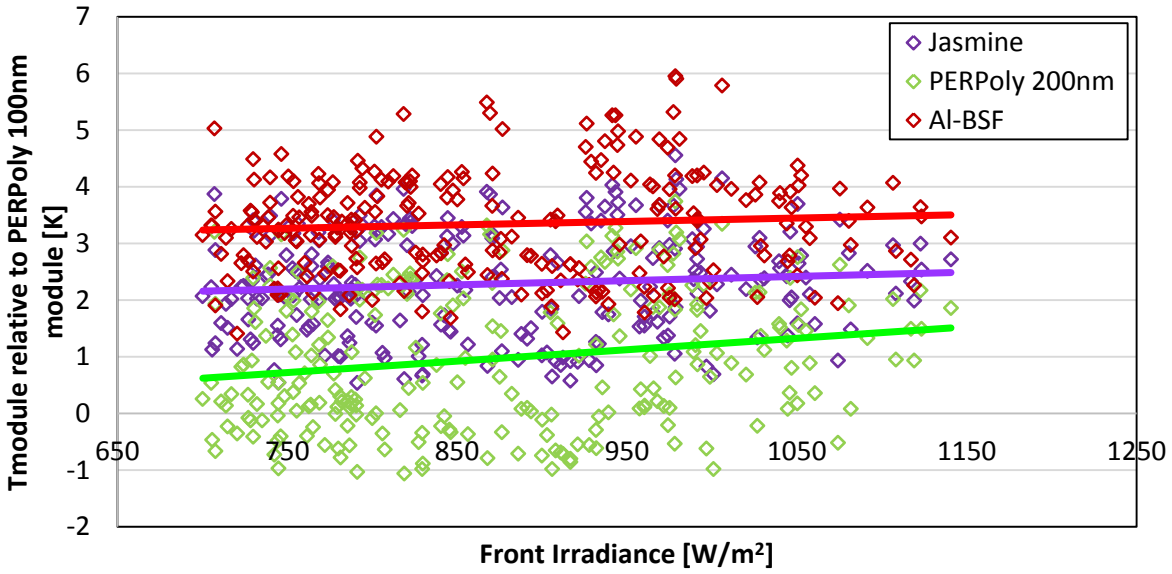

Figure 64: Temperature of glass-glass modules with different cell technologies relative to temperature of PERPoly 100nm module as a function of front irradiance.

5.3.3. Effect of Cell Technology on White back sheet & Black back sheet Modules

Figure 65 shows the module temperature relative to ambient temperature for white back sheet modules with different cell technologies (Al-BSF, PERPoly100nm, n-Pasha and Jasmine). The modules are placed close to each other on the rack (LC3, RB1, RB2 and RB3) (Figure 32). Due to the varying wind speed, relative temperatures of the modules are scattered between 5-25 K. Al-BSF module has the highest temperature which is 14.5±6.8 K higher than ambient temperature at 1000 W/m^2, as expected from heat input calculations. PERPoly 100nm and n-Pasha modules have similar relative temperatures which are 12.1±6.3 K and 12.4±6.5 K higher temperature than ambient temperature at 1000 W/m^2, respectively. The jasmine white back sheet module has 13.2±6.8 K higher temperature than ambient temperature at 1000 W/m^2.

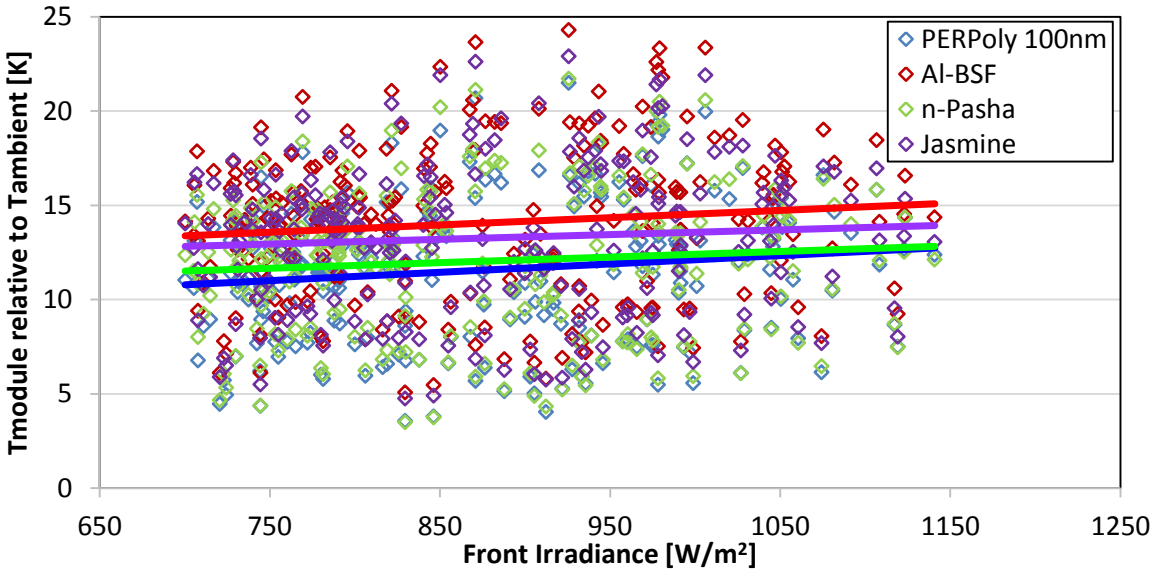

Figure 65: Temperature of white back sheet modules relative to ambient temperature as a function of front irradiance for different cell technologies.

Temperature of the modules relative to PERPoly 100nm module can be seen in Figure 66. Temperature of the Al-BSF is 2.4±0.8 K higher than temperature of PERPoly 100nm at 1000 W/m^2 due to the full area back contact. From indoor measurements, lower temperature is expected for n-Pasha module compared to PERPoly 100nm module due to free carrier absorption by polysilicon layer of PERPoly 100nm. From outdoor measurements they have comparable temperature but n-Pasha has 0.3±0.6 K higher temperature than PERPoly 100nm module at 1000 W/m^2 which might be due to the different angular dependencies of the modules. The jasmine module has 1.5±1 K higher temperature than PERPoly 100nm module at 1000 W/m^2.

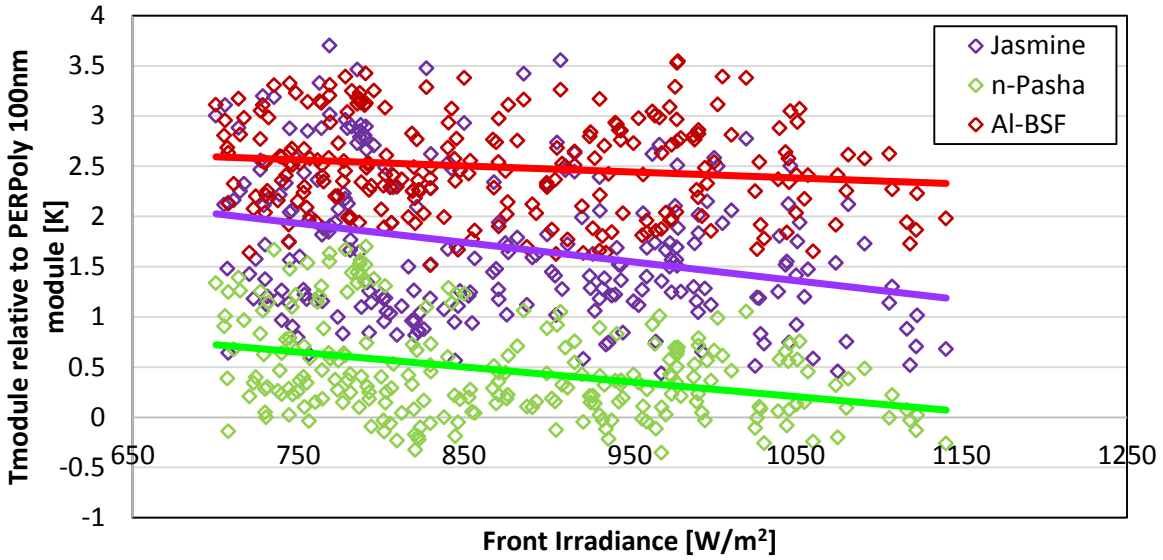

Figure 66: Temperature of white back sheet modules with different cell technologies relative to temperature of PERPoly 100nm module as a function of front irradiance.

Figure 67 shows the temperature of black back sheet modules (Al-BSF, PERPoly100nm, n-Pasha and Jasmine) relative to ambient temperature which are placed at LD1, LD2, LD3 and RD1 (Figure 32). Except jasmine module other modules have comparable relative temperatures as expected from indoor heat input measurements (Figure 57). The main reason for similar temperature is high absorption ratio of the black back sheet. Al-BSF has already high temperature which does not depend on the module type. However, as discussed in chapter 5.3.2, temperature of monofacial modules with bifacial cell is higher than temperature of bifacial module with bifacial cell. Hence, relative temperatures of modules with bifacial cell (except for jasmine module) approach the temperature of module with monofacial cell (Figure 67). Al-BSF, n-Pasha and PERPoly 100nm modules have 13.1±6.6 K, 14.2±6.5 K and 12.8±6.2 K higher temperature than ambient temperature at 1000 W/m^2. Temperature of the modules relative to PERPoly 100nm module can be seen in Figure 68. Due to the high absorption rate of black back sheet, temperature difference between different cell technologies are small. Al-BSF and n-Pasha modules have 0.6±1.2 K and 1.3±0.9 K higher temperature than PERPoly 100nm module at 1000 W/m^2. Jasmine module has higher temperature than the other modules which is 2.6±0.8 K higher than temperature of PERPoly 100nm module at 1000 W/m^2.

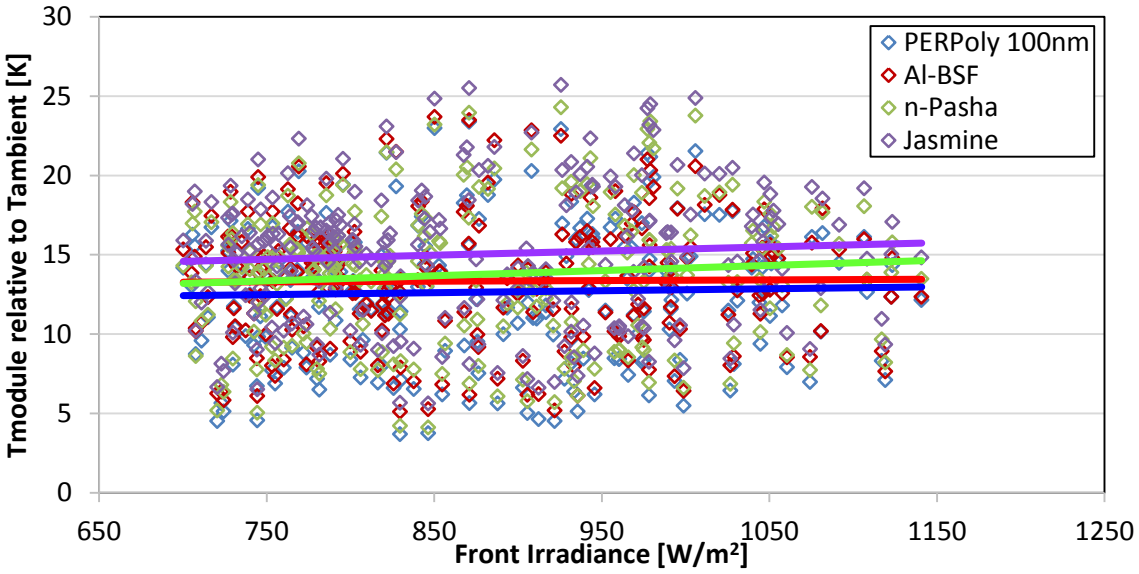

Figure 67: Temperature of black back sheet modules relative to ambient temperature as a function of front irradiance for different cell technologies.

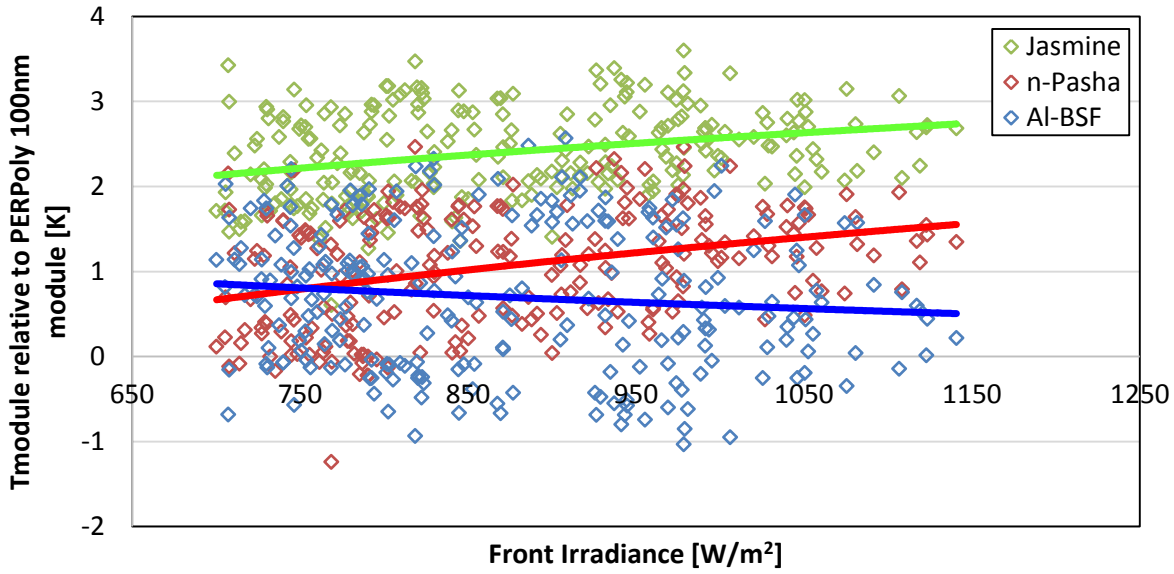

Figure 68: Temperature of black back sheet modules with different cell technologies relative to temperature of PERPoly 100nm module as a function of front irradiance.

5.3.4. Comparison between Al-BSF Module with White back sheet and PERPoly 100nm Glass-Glass Module

Existing solar farms mostly have monofacial modules with Al-BSF cells. Also, those modules have white back sheet in order to increase the electrical yield by optical coupling. Higher energy yield for bifacial modules with bifacial cell compared to monofacial modules with Al-BSF cell is proven. This indicates that bifacial modules can be a good alternative for monofacial modules in order to increase electrical yield. Another advantage of the bifacial modules over monofacial modules is lower operating temperature. Figure 69 shows that white back sheet module with Al-BSF cell has 3.6±1.5 K higher temperature than glass-glass module with PERPoly 100nm module at 1000 W/m^2. If we consider a solar farm which has 100 MW power capacity with 280 W modules, the temperature difference will increase the

power output 1.5±0.6% at 1000 W/m^2 in addition to the bifacial gain This means that PERPoly 100nm module has 1.5±0.6 MW power gain compared to Al-BSF module due to temperature effect.

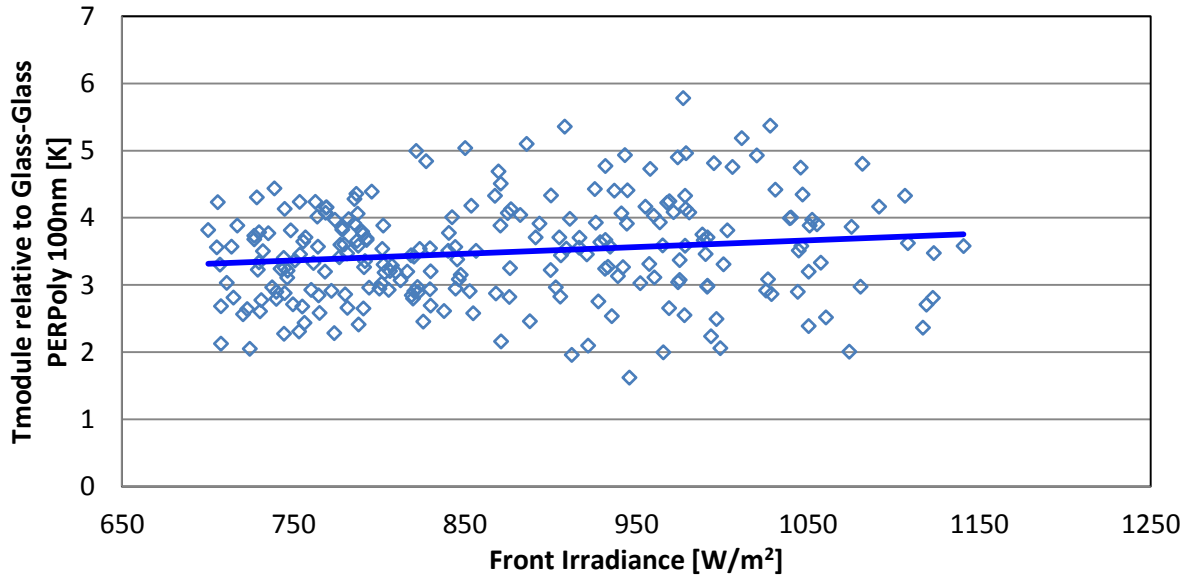

Figure 69: Temperature of Al-BSF white back sheet module relative to PERPoly 100nm glass-glass module.

5.4. Temperature Model Validation

The model that was explained in chapter 3 was used to predict temperature of the modules by using weather data (ambient temperature, wind speed, front and rear irradiance) and module characteristics (e.g. reflection, transmission, front and rear efficiency of the module). In order to verify the model two days are selected which are high irradiance and low irradiance days. Irradiance of those days can be seen in Figure 70. Predicted module temperature by the fluid dynamic model is compared with observed module temperature by the temperature sensors which are placed at the back of the modules. In this chapter, only different module types with bifacial cell (n-Pasha) are verified.

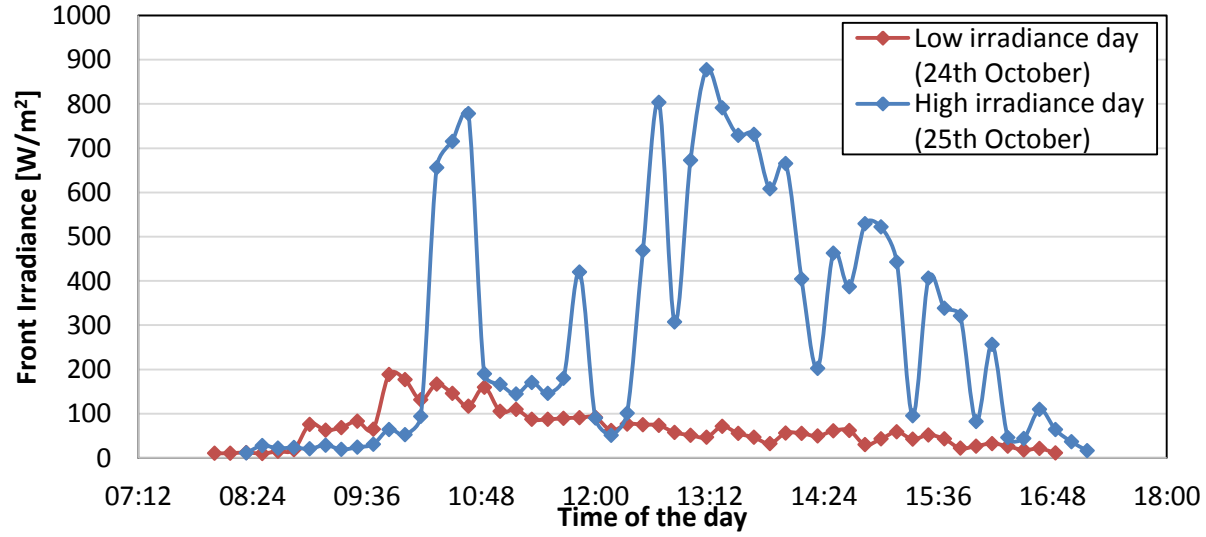

Figure 70: Front irradiance of 24th (Low irradiance day) and 25th (High irradiance day) of October.

5.4.1. Glass-Glass Module

Figure 71 and 72 show ambient temperature, wind speed (right y-axis), observed temperature, predicted temperature and temperature difference between observed and predicted temperature for high and low irradiance days, respectively. Both observed and predicted temperatures follow the irradiance during the day (Figure 70 and 71). Since irradiance fluctuates for high irradiance day, both observed and predicted temperatures also fluctuate. There are some over- or under-predictions, mostly results of the irradiance fluctuations which are results of the partly cloudy sky. In real life, those irradiances might be only for some seconds but the model predicts the temperature by using that irradiance for the full time step of 10 minutes which might be the reason for larger differences between observed and predicted temperature. Additionally, wind direction also, might have an effect on the difference between predicted and observed temperature which affects heat transfer by convection. Also, when the irradiance does not fluctuate (e.g. between 11:00 and 11:40), predicted temperature is 1-2 ˚C lower than observed temperature. On low irradiance days with maximum irradiance around 190 W/m^2, predictions are lower than observed temperature (around 1-2 ˚C) (Figure 72). Irradiance does not vary much during the day so difference between observed and predicted module temperature does not fluctuate. Additionally, predicted temperature is below the ambient temperature in some cases (Figure 71 and 72). Further research is needed to improve the temperature model.

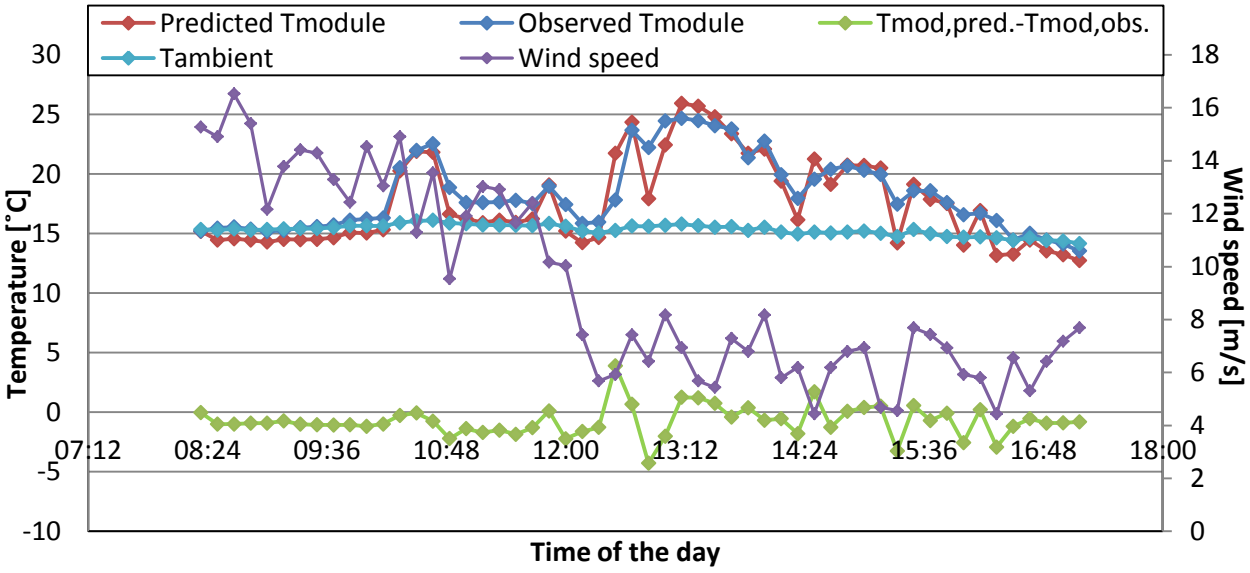

Figure 71: Predicted and observed module temperature of glass-glass module with ambient temperature and wind speed for 25th of October (High irradiance day).

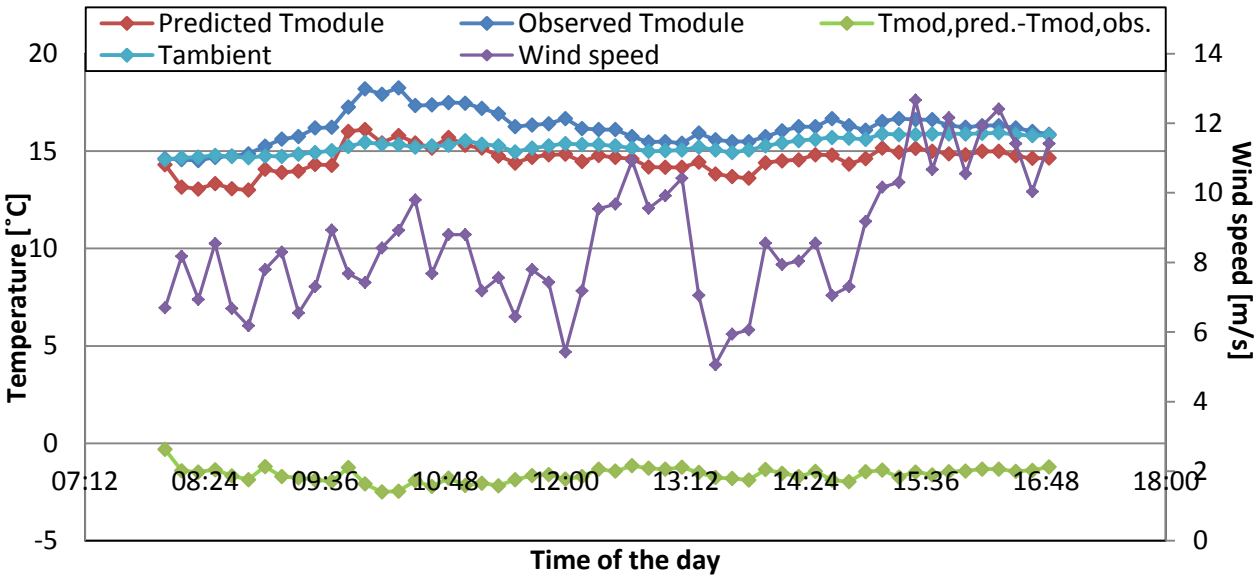

Figure 72: Predicted and observed module temperature of glass-glass module with ambient temperature and wind speed for 24th of October (Low irradiance day).

5.4.2. White back sheet and Black back sheet Modules

Figure 73 and 74 show the predicted and observed temperature of white back sheet module on high and low irradiance days, respectively. Again, predicted module temperature follows the observed temperature. Since temperature of white back sheet module is only around 1 ˚C higher than glass-glass module, the model also predicts temperature of white back sheet module successfully. However, as discussed before, when irradiance fluctuates, the difference between observed and predicted temperature increases. Additionally, the model still predicts 1-2 ˚C lower than the observed module temperature at low irradiances (Figure 74). One of the possible reasons for under predicting the module temperature might be assuming the wind speed same at the top and the back surface of the module. Possibly, in real life wind speed at the back surface of the module is lower than wind speed at the top surface of the module which means that the model overestimates the heat transfer by forced convection from rear side. Therefore, the model predicts the temperature lower than actual temperature. In some cases, module temperature is close to ambient temperature. In these cases predicted temperature is also lower than ambient temperature, since predicted temperature is mostly 1-2 ˚C lower than observed temperature. Further research is needed as stated before.

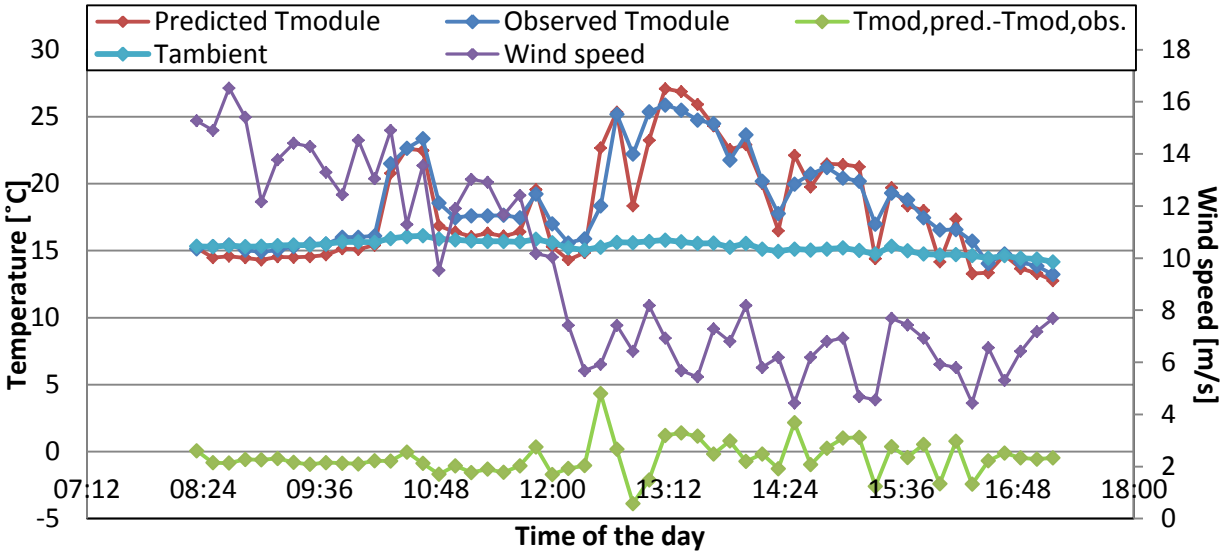

Figure 73: Predicted and observed module temperature of white back sheet module with ambient temperature and wind speed for 25th of October (High irradiance day).

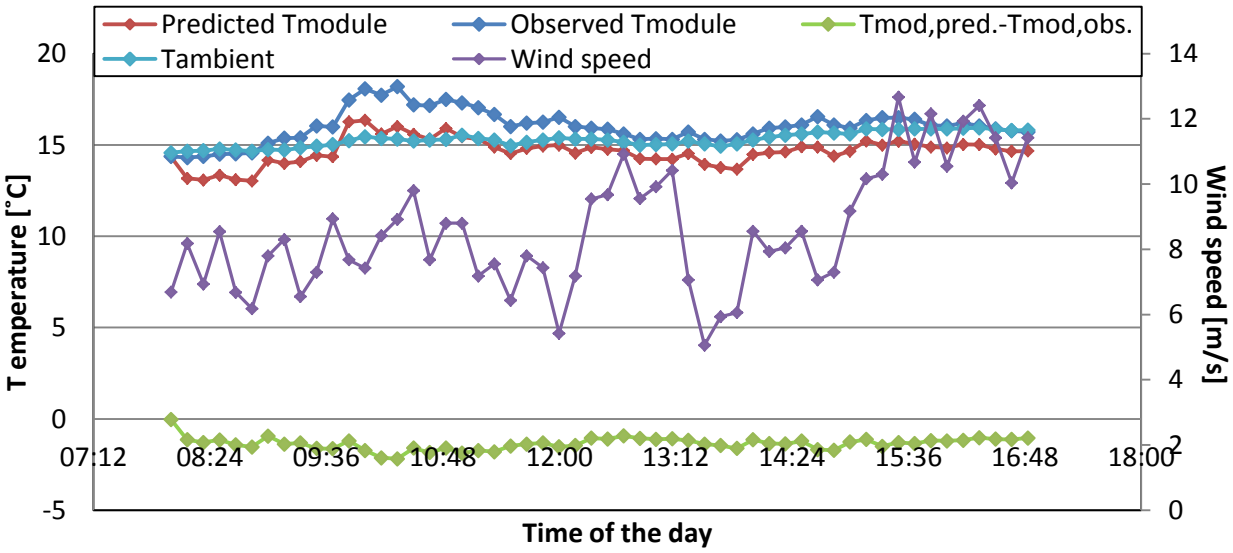

Figure 74: Predicted and observed module temperature of white back sheet module with ambient temperature and wind speed for 24th of October (Low irradiance day).

Figure 75 and 76 show the predicted and observed temperatures of black back sheet module at high and low irradiance days, respectively. Predicted module temperature is mostly close to the observed module temperature. However, when irradiance fluctuates, the difference between observed and predicted temperatures increases (Figure 75). At low irradiances, predicted temperature is lower than observed temperature also for the black back sheet module because of the explained reason in the previous paragraph (Figure 76).

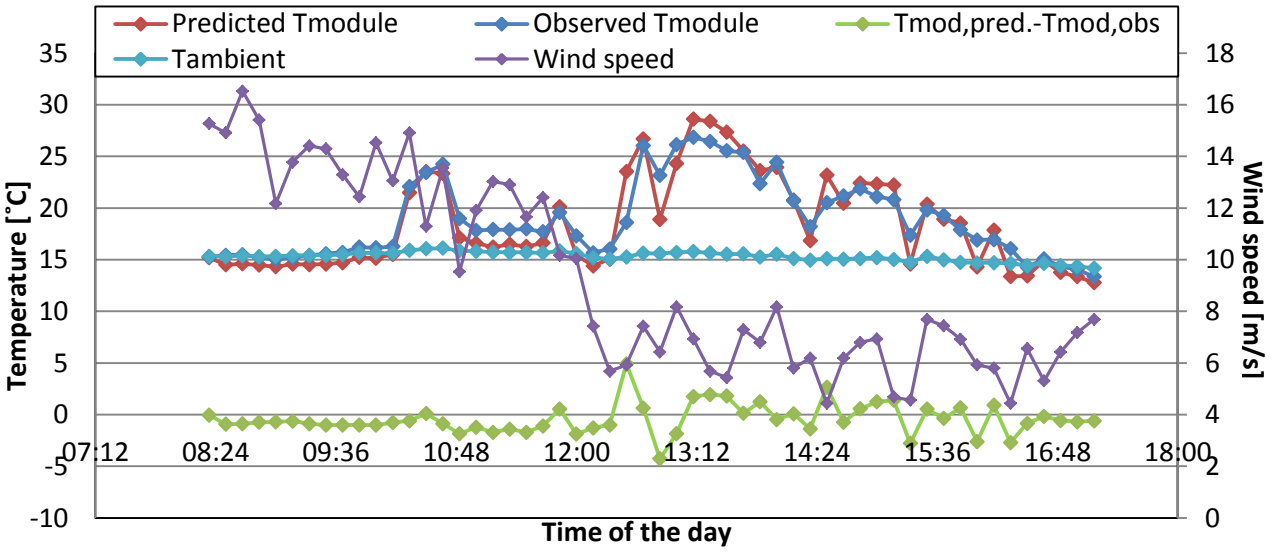

Figure 75: Predicted and observed module temperature of black back sheet module with ambient temperature and wind speed for 25th of October (High irradiance day).

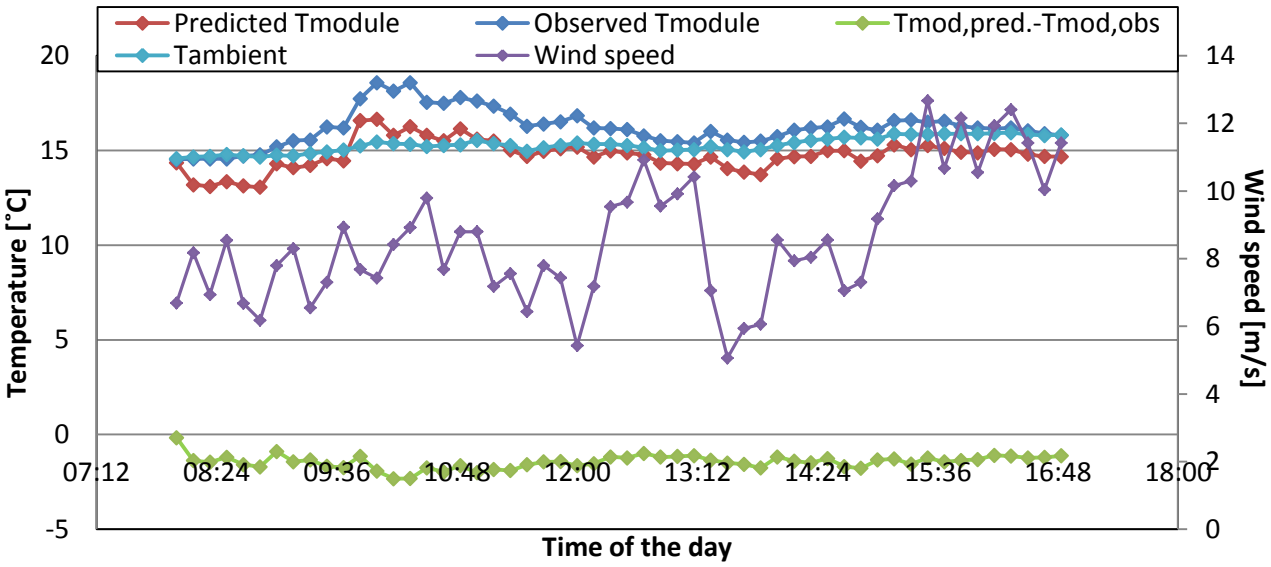

Figure 76: Predicted and observed module temperature of black back sheet module with ambient temperature and wind speed for 24th of October (Low irradiance day).

6. Conclusion

Spectral reflection, spectral transmission, spectral response and IV indoor measurements were done for different cell and module technologies in order to derive the parasitic which includes free carrier absorption, recombination, absorption of metal parts of the solar cell and absorption of module materials (only for modules) and total heat input of the cells and modules. To see the effect of the heat input on the operating temperature of the modules, all modules were placed on the roof-top of a building and the temperatures of the modules were derived from the V_{oc}. From the heat input of cell calculations, highest parasitic heat input is expected for Al-BSF cell compared to bifacial cells. In addition, the module with Al-BSF cell has higher total and parasitic heat input compared to modules with bifacial cell due to the parasitic absorption of full area aluminum back contact. For glass-glass modules, total and parasitic heat input difference between Al-BSF and bifacial modules increase with rear irradiance since aluminum rear contact of the Al-BSF either absorbs 80% of the incoming light.

From cell to module, especially, parasitic absorption increases because of the absorption of module materials (glass, EVA and back sheet). Due to the absorption of glass and EVA, parasitic heat input increases from cell to module at 300-400 nm wavelength range of the light for all module types. Since light passes through the bifacial cells, the module type (different rear encapsulation material) affects the parasitic heating of the module. Black back sheet module has the highest parasitic heat input due to the black back sheet which has around 95% absorbing rate. The glass-glass modules have the lowest parasitic heat input because of the glass and EVA as rear encapsulation materials which have high transmission rates. On the other hand, the module type does not affect the total and parasitic heat input of the modules with Al-BSF cell because incident light cannot pass through the Al-BSF cell.

Glass-glass modules with Al-BSF cell have highest operational temperature compared to glass-glass modules with bifacial cell at between 700 and 1200 W/m^2 front irradiance due to the full area aluminum back contact of the Al-BSF cell. Temperature of the glass-glass module with Al-BSF cell is 3.4±1.7 K higher than the temperature of the PERPoly 100nm module at 1000 W/m^2 when the rear irradiance is around 11% of the front irradiance. Rear irradiance has strong effect on the parasitic heat input of the Al-BSF module due to the high absorption rate of aluminum back contact which is around 80% above 500 nm wavelength for aluminum/EVA+glass interface. Therefore, higher temperature difference is expected when the rear irradiance fraction is higher. For white back sheet modules with different cell technologies, still Al-BSF module has the highest temperature compared to modules with bifacial cells. The Al-BSF white back sheet module has 2.4±0.8 K higher operational temperature than PERPoly 100nm white back sheet module at 1000 W/m^2. For the black back sheet modules, the temperature difference for the same type of cells that are mentioned above is lower which is 0.6±1.2 K at 1000 W/m^2. Due to the high absorbing rate of the black back sheet, temperature difference is low as expected from indoor heat input calculations.

Bifacial modules have higher energy yield compared to monofacial modules due to the gain from the rear irradiance. Another advantage of bifacial modules with bifacial cells compared to monofacial modules with monofacial cells is lower operational temperature even bifacial module has higher heat input than monofacial module from indoor measurement

calculations. The main reasons for the absence of heating of bifacial module might be 6% higher emissivity of glass compared to back sheet [1] [2]. Therefore, radiative heat transfer of glass-glass module is higher than radiative heat transfer of white back sheet module. Also, heat transfer within the module level might be better for bifacial module compared to monofacial module. The white back sheet module with Al-BSF cell has 3.6±1.5 K higher temperature than glass-glass module with PERPoly 100nm at 1000 W/m^2 when the fraction of rear irradiance is around 11% of the front irradiance. The temperature difference results in 1.5±0.6% power gain for PERPoly 100nm module relative to Al-BSF module, which corresponds to 1.5±0.6 MW relative power gain for 100 MW power capacity solar farm. At higher rear irradiance conditions, the glass-glass module with PERPoly 100nm might have similar temperature with Al-BSF white back sheet module but still glass-glass module has energy gain due to irradiance on the rear.

The temperature model mostly predicts 1-2 ˚C lower module temperature than observed module temperature which might be due to predicting forced convection heat transfer from rear side higher than actual forced convection from rear side. This is the result of assuming wind speed equal at both sides of the module. However, due to the module and other components of the rack, wind speed behind the module might be lower than wind speed at the front side of the module. By assuming wind speed higher than actual wind speed behind the module, forced convection heat transfer is predicted higher than actual forced convection heat transfer at the rear side of the module. Hence, this might cause the module temperature to be lower than actual module temperature.

7. Recommendation

From indoor heat input calculations, slightly lower module temperature is expected for jasmine cells compared to other bifacial cells. However, from heat input calculations of the modules and outdoor module temperature measurements, jasmine modules have higher temperature than modules with bifacial cell for glass-glass and white back sheet module types. This needs to be investigated for better understanding about making modules by using the jasmine cell. Also, from both cell and module heat input calculations, lower temperature is expected from n-Pasha modules compared to PERPoly 100nm modules due to a lower heat input of n-Pasha modules compared to PERPoly 100nm modules. However, operational temperature of PERPoly 100nm modules are slightly lower than operational temperature of n-Pasha modules. In order to understand it better, effect of heat input on both should be investigated. This might be due to structural differences between the cells.

Outdoor measurements are held with low albedo ground (black concrete). Rear irradiance is around 11% of the front irradiance. In order to increase the effect of rear irradiance on the module temperature, the floor of the rooftop should be painted white (high albedo factor) which will affect the temperature differences between different modules.

The heat input of various modules is known from indoor calculations but conductive heat transfer from solar cell to module surroundings was not investigated in this work. While comparing temperatures of two different module technologies, heating aspects (e.g. heat capacity and conductivity) of the module materials might have had an influence on the temperature difference between those modules. Hence, for better understanding of heat transfer from cell to surrounding of the module and effect of the module type on temperature of the module, heat capacity and conductivity of the module materials can be investigated and conductive heat transfer model can be developed.

8. Acknowledgement

I would like to thank my supervisors Arthur Weeber, Bas van Aken and Machteld Lamers who gave me the opportunity to do my thesis work on this wonderful project. I gained invaluable amount of knowledge from the three of your regarding solar cells, modules and also mainly about conducting scientific research. I am grateful to have worked with such nice, kind and fun people. I am also grateful to Mark Jansen and Koen de Groot who worked a lot in order to make the outdoor measurements possible and taught me a lot related to module and measurement parts of this work. I would also like to thank all my ECN colleagues for the providing a wonderful working atmosphere and for being helpful even for small things. I am thankful to the thesis committee Réne van Swaaij, Erik van der Kolk and Rudi Santbergen for having agreed to read and grade my work.

I would also like to thank Piet, Margo and Rosa who were always helpful and kind to me during my stay in Petten.

During my time at ECN, which was more than a year, I have met lots of interns and it is tough to mention all of them here. I am very happy to have met all of you and I enjoyed spending time with you all, especially playing table tennis. Mike, thanks for your help, good times and being a great company. We started this journey together and if you need any help about some measurement setups, I can help you anytime. I am thankful to Hande who helped me about a lot of things during her work at ECN and she even continued to help me from Turkey. Sundeep and Rithwick, my two Indian brothers, I am glad to know you guys and thank you both for your support during this work. We had a great time during our two years and I know we will have good times in the future as well. I am also extremely thankful to my friends Alara and Baran who helped me and kept me motivated during this journey, even during the time you were not aware. Especially Alara, I really appreciate and thankful for all of your help and support during my work. I am delighted to have both of you.

The rest is for my parents.

Benim sevgili ailem, siz olmasaydınız bu başardıklarımı asla başaramazdım. Beni özleseniz dahi hep motive edip destek oldunuz ve hiç yanımdan ayrılmadınız. Canım çekmesin diye bazen ne yediğinizi bile söylemek istemediğiniz oldu. Sadece bu çalışmamda değil bütün hayatım boyunca bana destek olduğunuz ve şuan oldugum kişi olmamı sağladığınız için size çok teşekkür ederim. Böyle bir aileye sahip olduğum için gerçekten ne kadar şanslı olduğumu anlatamam. Kardeşime ve bana her zaman en iyiyi sunmak için elinizden geleni ve hatta fazlasını yaptığınızı asla unutamam. Bazen içiniz ne kadar farklı hissetse de bize destek olmaktan asla geri durmadınız. Hakkınızı asla ödeyemeyiz. Kardeşim evin hala şimarik çocuğu olduğun için sana ayrı teşekkür ederim.

9. Bibliography

[1] G. Notton, C. Cristofari, M. Mattei en P. Poggi, „Modelling of a double-glass photovoltaic module using finite differences," *Applied Thermal Engineering,* nr. 25, pp. 2854-2877, 2005.

[2] M. D. Bazilian, H. Kamalanathan en D. Prasad, „Thermographic analyses of building integrated photovoltaic systems," *Renewable Energy,* nr. 26, pp. 449-461, 2002.

[3] IRENA, „REthinking Energy 2017: Accelarating the global energy transformation," International Renewable Energy Agency, Abu Dhabi, 2017.

[4] F. Kersten, R. Doll, A. Kux, D. Huljic, M. Görig, C. Breyer, J. Müller en P. Waver, „PV learning curves: Past and future drivers of cost reduction," in *26th European Photovoltaic Solar Energy Conference*, Hamburg, 2011.

[5] Deloitte, „US solar power growth through 2040: Exponential or inconsequential?," 2015.

[6] ITRPC en VDMA, „International technology roadmap for photovoltaic: 2016 results," 2017.

[7] C. Breyer, F. Kersten, A. Gerlach, J. Goldschmidt, G. Stryi-Hipp, D. Montoro en M. Riede, „Research and development investments in PV - A limiting factor for a fast PV diffusion?," in *PVSEC*, Valencia.

[8] Fraunhofer Institute for Solar EnergySystems en PSE AG, „Photovoltaics report," Freiburg, 2017.

[9] J. Zhao, A. Wang, P. Altermatt en M. Green, „High efficieny PERT cells on n-type silicon substrates," in *29th IEEE Photovoltaic Specialists Conference*, 2002.

[10] M. Stodolny, M. Lenes, Y. Wu, G. Janssen, I. Romijn en J. G. L. Luchies, „n-type polysilicon passivating contacts," in *European PV Solar Energy Conference*, Munich, 2016.

[11] M. Lammert en R. Schwartz, „The integrated back contact solar cell: A silicon solar cell for use in concentrated sunlight," *IEEE Transactions on Electron Devices,* vol. 24, nr. 4, pp. 337-342, 1977.

[12] G. Nemet, „Beyond the learning curve: factors influencing cost reductions," *Energy Policy,* vol. 34, pp. 3218-3232, 2006.

[13] L. Yang, Q. Ye, A. Ebong, W. Somg, G. Zhang, J. Wang en Y. Ma, „High efficiency screen printed bifacial solar cells on monocrystalline CZ silicon," *Progress in Photovoltaics: Research and Applications,* pp. 275-279, 2010.

[14] A. Hübner, A. Aberle en R. Hezel, „Temperature behaviour of monofacial and bifacial silicon solar cells," in *Photovoltaic Specialists Conference*, 1997.

[15] D. K. Schroder, R. N. Thomas en J. C. Swartz, „Free carrier absorption in silicon," *IEEE Journal of*

solid-state circuits, vol. 13, pp. 180-187, 1978.

[16] T. Tiedje, E. D. C. G. Yablonovitch en B. G. Brooks, „Limiting efficiency of silicon solar cells," *IEEE Transactions on electron devices,* vol. 31, pp. 711-716, 1984.

[17] E. Bende, I. Cesar, M. Lamers, P. Manshanden, J. Anker, Y. Zhang en E. Granneman, „Jasmine (茉莉): A low-cost alternative to the PERC solar cell".

[18] A. Smets, K. Jager, O. Isabella, R. van Swaaij en M. Zeman, Solar Energy: The physics and engineering of photovoltaic conversion technologies and systems, Cambridge: UIT Cambridge, 2016.

[19] M. Ruben Vogt, „Development of Physical Models for the Simulation of Optical Properties of Solar Cell Modules," 2015.

[20] M. A. Green, „Self-consistent optical parameters of intrinsic silicon at 300K including temperature coefficients," *Solar energy materials & solar cells,* pp. 1305-1310, 2008.

[21] E. Yablonovitch en G. D. Cody, „Intensity Enhancement in Textured Optical Sheets for Solar Cells," *IEEE Transactions on Electron Devices,* vol. 29, pp. 300-305, 1982.

[22] D. A. Clugston en P. A. Basore, „Modelling free-carrier absorption in solar cells," *Progress in photovoltaics: Research and applications,* vol. 5, pp. 229-236, 1997.

[23] S. C. Baker-Finch, K. R. McIntosh, D. Yan, K. C. Fong en T. C. Kho, „Near-infrared free carrier absorption in heavily doped silicon," *Journal of applied physics,* p. 116, 2014.

[24] O. B. Chan, „Defects in silicon solar cell materials," 1993.

[25] M. A. Green, Silicon Solar Cells Advanced Principles & Practice, Centre for Photovoltaic Devices and Systems, University of New South Wales, 1995.

[26] M. Rüdiger, J. Greulich, A. Richter en M. Hermle, „Parametrization of free carrier absorption in highly doped silicon for solar cells," *IEEE Transactions on Electron Devices,* vol. 60, pp. 2156-2164, 2013.

[27] J. Isenberg en W. Warta, „Free carrier absorption in heavily doped silicon layers," *Applied Physics Letters,* vol. 84, pp. 2265-2267, 2004.

[28] R. A. Falk, „Near IR absorption in heavily doped silicon - An empirical approach," in *International symposium for testing and failure analysis*, 2000.

[29] F. Feldman, M. Nicolai, R. Müller, C. Reichel en M. Hermle, „Optical and electrical characterization of poly-Si/SiOx contacts and their implications on solar cell design," *Energy Procedia,* vol. 124, pp. 31-37, 2017.

[30] R. Santbergen, „Optical Absorption Factor of Solar Cells for PVT systems," Eindhoven University Press, Eindhoven, 2008.

[31] L. Tous, „Nickel/Copper Plated Contacts as an Alternative to Silver Screen Printing for Front Side Metallization of Industrial High Efficiency Silicon Solar Cells," Leuven, 2014.

[32] *Private conversation. M.W.P.E. Lamers.,* 20 April 2017.

[33] M. R. Vogt, H. Holst, M. Winter, R. Brendel en P. P. Altermatt, „Numerical modelling of c-Si PV modules by coupling the semiconductor with the thermal conduction, convection and radiation equations," in *5th International Conference on Silicon Photovoltaics, SiliconPV* , Konstanz, 2015.

[34] M. Green, „Solar Cells," New South Wales, The University of New South Wales, 1998, pp. 91-92.

[35] C. Honsberg en S. Bowden, „PVeducation," 28 3 2013. [Online]. Available: http://www.pveducation.org/pvcdrom/characterisation/measurement-of-ideality-factor. [Geopend 15 10 2017].

[36] I. Romijn, B. van Aken, J. Anker, A. Burgers, A. Gutjahr, B. Heurtault, M. Koppes, E. Kossen, M. Lamers, D. Saynova en C. Tool, „Industrial implementation of efficieny improvements in n-type solar cells and modules," in *27th European Photovoltaic Solar Energy Conference*, Frankfurt, 2012.

[37] I. Romijn, J. Anker, A. Burgers, A. Gutjahr, B. Heurtault, M. Koppes, E. Kossen, M. Lamers, D. Saynova en C. Tool, „Industrial n-type solar cells with >20% cell efficiency," in *China PV Technology International Conference*, Shanghai, 2013.

[38] K. Sugibuchi, N. Ishikawa en S. Obara, „Bifacial-PV Power Output Gain in the Field Test Using ""EarthON"" High Bifaciality Solar Cells," in *28th European Photovoltaic Solar Energy Conference*, Paris, 2013.

[39] A. Blakers, A. Wang, A. Milne, J. Zhao en M. Green, „22.8% efficient silicon solar cell," *Applied Physics Letters,* vol. 55, nr. 13, 1989.

[40] M. Green, „The Passivated Emitter and Rear Cell (PERC): From conception to mass production," *Solar Energy Materials & Solar Cells,* vol. 143, pp. 190-197, 2015.

[41] S. Nold, N. Voigt, L. Friedrich, D. Weber, I. Hädrich, M. Mittag, H. Wirth, B. Thaidigsman, I. Brucker, M. Hofmann, J. Rentsch en R. Preu, „Cost modelling of silicon solar cell production innovation along the PV value chain," in *EUPVSEC*, 2012.

[42] C. Honsberg en S. Bowden, „PV education," [Online]. Available: http://www.pveducation.org/pvcdrom/modules/heat-loss-in-pv-modules. [Geopend 20 August 2017].

[43] M. K. Fuentes, „A Simpified Thermal Model fo Flat Plate Photovoltaic Arrays," Sandia National

Laboratories, 1987.

[44] „The Engineering toolbox," [Online]. Available: https://www.engineeringtoolbox.com/dry-air-properties-d_973.html. [Geopend 10 October 2017].

[45] „Engineerin toolbox," [Online]. Available: http://www.engineeringtoolbox.com/air-properties-d_156.html. [Geopend August 2017].

[46] H. Van den Aker en R. F. Mudde, Transport Phenomena, The Art of Balancing, Delft: Delft Academic Press/VSSD, 2014.

[47] J. A. Duffie en W. A. Beckman, Solar Engineering of Thermal Processes, Ner Jersey: John Wiley & Sons.

[48] S. Armstrong en W. Hurley, „A thermal model for photovoltaic panels under varying atmospheric conditions," *Applied Thermal Engineering,* vol. 30, pp. 1488-1495, 2010.

[49] W. Swinbank, „Long wave radiation from clear skies," 1963.

[50] P. Hoang, V. Bourdin, Q. Liu, G. Caruso en V. Archambault, „Coupling optical and thermal models to accurately predict PV panel electricity production," *Solar Energy Materials & Solar Cells,* vol. 125, pp. 325-338, 2014.

[51] *Private conversation. K.M. de Groot.,* 1 August 2017.

[52] *Private conversation. M. Jansen and K.M. de Groot.,* 20 July 2017.

[53] *Private Conversation. G.J.M. Janssen.,* 1 November 2017.

[54] I. Haedrich, S. Surve en A. Thomson, „Cell to Module (CTM) ratios for varying industrial cell types," in *Asia - Pacific Solar Research Conference*, 2015.

[55] I. Haedrich, U. Eitner, M. Wiese en H. Wirth, „Unified methodology for determining CTM ratios: Systematic prediction of module power," *Solar Energy Materials and Solar Cells,* vol. 131, pp. 14-23, 2014.

[56] I. Romijn, B. van Aken, J. Anker, A. Burgers, A. Gutjha, B. Heurtault, M. Koppes, E. Kossen, M. Lamers, D. Saynova, C. Tool, F. Lang, G. Li, H. Wang, Z. Hu, P. Venema en A. Vlooswijk, „Industrial implementation of efficiency improvements in n-type solar cells and modules," in *27th European Photovoltaic Solar Energy Conference* , Frankfurt, 2012.

[57] J. Singh, Y. Khoo, J. Chai, Z. Liu en Y. Wang, „Cell-to-module power loss/gain analysis of silicon wafer-based PV modules," *Photovoltaics International,* vol. 31, pp. 90-98, 2016.

[58] K. Mcintosh, J. Cotsell, J. Cumpston, A. Norris, N. Powell en B. Ketola, „An optical comparison of silicone and EVA encapsulants for conventional silicon PV modules: A ray-tracing study," in *34th*

IEEE Photovoltaics Specialists Conference, Philadelphia, 2009.

[59] M. Kang, K. Ryu, A. Upadhyaya en A. Rohatgi, „Optimization of SiN AR coating for Si solar cells and modules through quantitative assessment of optical and efficiency loss mechanism," *Progress in Photovoltaics,* vol. 19, nr. 8, pp. 983-990, 2011.

[60] I. Peters, Y. Khoo en T. Walsh, „Detailed current loss analysis for a PV module made with textured multicrystalline silicon wafer solar cells," *IEEE journal of photovoltaics,* vol. 4, nr. 2, pp. 585-593, 2014.

[61] S. Krauter en P. Grunom, „Optical simulation to enhance PV module encapsulation," in *21st EU PVSEC*, Dresden, 2006.

[62] C. Ballif, J. Dicker, D. Borchert en T. Hofmann, „Solar glass with industrial porous SiO2 antireflection coating: measurements of photovoltaic module properties improvement and modelling of yearly energy yield gain," *Solar energy materials and solar cells,* vol. 82, nr. 3, pp. 331-344, 2004.

[63] Y. Khoo, T. Walsh, F. Lu en A. Aberle, „Method for quantifiyng optical parasitic absorptance loss of glass and encapsulant materials of silicon wafer based photovoltaic modules," *Solar Energy Materials & Solar Cells,* vol. 102, pp. 153-158, 2012.

[64] P. Campell en M. A. Green, „Light trapping properties of pyramidally textured surfaces," *Journal of Applied Physics,* vol. 62, pp. 243-249, 1987.

[65] „Climate change 2007: The Physical Science Basic," Paris, 2007.

[66] J. Gee, W. Schubert en P. Basore, „Emitter wrap-through solar cell," in *Photovoltaic Specialists Conference*, Louisville, KY, USA, 1993.